University of Alberta

Fabrication of colloidal crystals featuring sub-20 nm pore size for protein separation

by

Ali Malekpourkoupaei

A thesis submitted to the Faculty of Graduate Studies and Research
in partial fulfillment of the requirements for the degree of

Master of Science

Mechanical Engineering

Fall 2012
Edmonton, Alberta

To my beloved wife, Roya

ABSTRACT

Clinical point-of-care (POC) diagnosis remains an open and challenging field of research worldwide in which the study of the mechanism and dynamics of protein molecule separation using electrophoresis is of considerable interest.

The quality of a protein separation is strongly dependent on the separating matrix and conditions under which the electrophoresis is performed. This research is mainly focused on development of a novel separation matrix, based upon the self-assembly of particles in a colloidal suspension, within a microfluidic chip. Several challenges were overcome in developing crystalline particle arrays that generate a porous material with pores smaller than 20 nm. The effect of pore size on separation of proteins of differing molecular weight and size was then studied, and the mechanism of separation, which appears to change in the smallest size range, was explored.

ACKNOWLEDGMENT

It is really very difficult for me to acknowledge two of the most determining persons in my academic life, professor D. Jed Harrison and professor Larry W. Kostiuk. Their personalities, brightness, supervisions and most importantly perspectives of science and engineering have made them excellent role models for the rest of my academic life. I could never imagine any better supervisors than them.

I am feeling grateful and lucky to work with one of the world's pioneers in microfluidics, Dr. D. Jed Harrison. I thank him for providing me the brilliant opportunity of attending the major 15th International Conference in Seattle on Miniaturized Systems for Chemistry and Life Science where I could gain insights into this field and its impact on various aspects of our lives. As a spiritual mentor, Jed was always there for me during the very tough times of my research when he was also pretty busy as the chairman of the department of Chemistry. This is why I could successfully get over all of that and reach to this point.

I would like to express my greatest and sincere gratitude to an exceptional professor, Dr. Larry W. Kostiuk who as a chairman of my home department generously supported me during breathtaking moments of my M.Sc. program and I would never ever forget his help. Larry broadened my view of different aspects

of science and “academic life” to a large extent. I am happy that he shared his smart and insightful thoughts and attitudes with me so that I can find answers to many of my big questions.

I appreciate DJH group members as an absolutely wonderful labmates who made my times during my research very smooth and joyful. I thank support and friendship from all of them, including Wenmin Ye, Huiying Sheng, Sabrina Peng, Narges Shabani, Dr. Abebaw Jemere, Hamid Ramezani, Yonxin Zhao, Reshma Singh, Mohammad Azim, Le Zhang and Ya Zhou. I am grateful for the help from the support staff in electronic shop, machine shop, general office of the Chemistry department and also NanoFab.

I am thankful to professor J. William Lown for his valuable advises regarding my future academic plans.

I specially acknowledge professor Michael Brett’s group for their generous support of gaseous krypton used for the porosimetry experiments. Many thanks go to Dr. Katie Krause for our valuable discussions regarding porosimetry.

My deepest gratitude goes to my parents who tried their best to support me making my future. They always supported me and never asked for anything in return.

Words fall short of expressing my deep appreciation to my beloved wife, Roya, for her love and trust. Without her understanding, this would never be possible.

TABLE OF CONTENTS

LIST OF TABLES

LIST OF FIGURES

LIST OF NOMENCLATURE

A_c	The microchannel cross-sectional area
$D_{w,a}$	Diffusion coefficient of water in air
d_h	Hydrodynamic diameter
d_L	Diameter of the small particles
d_S	Diameter of the large particles
$d_p^{av.}$	Average diameter of a particle
f	Friction coefficient
$\boldsymbol{g}$	Gravitational acceleration vector
g	Gravitational acceleration
h	Height of the liquid phase in the reservoir
J_{0e}	Rate of evaporation from a flat surface
J_e	Evaporation rate at the drying front
J_o	Overall flow
J_p	Rate of fluid flow through the grown crystal
k	Column permeability
k_B	Boltzmann constant
κ^{-1}	Thickness of the double layer
m	Total number of ions
N	Number of residues in the polypeptide chain of protein
n	Small to large particle number ratio
n_i	Density of the ith ion
p_h	Hydrostatic pressure
p_C	Capillary pressure
p_{atm}	Atmospheric pressure
p_l	Total liquid phase pressure in the curvature
p	Pressure
p_h	Hydrostatic pressure
p_C	Capillary pressure
p_o	Krypton solidification pressure at 87 K
Q	Total charge

r_p	Pore radius
r_M	Radius of curvature
r_{M0}	Constant in equation (2-9)
$\mathrm{R}_{\mathrm{hyd.}}$	Hydrodynamic radius of a protein
R	Radius
R_g	Gyration radius
t	Time
T	Temperature
t_0	Characteristic time in equation (2-19)
y_c	Length of the crystal

Greek symbols

μ^{EOF}	Electro osmotic mobility
ρ_0	Density of water vapor
ρ_f	Density of the fluid
ρ_p	Density of a particle
ρ_w	Mass concentration of water
$\rho_{w\infty}$	Mass concentration of water vapor at infinity
φ_L	Volume fraction of the large particles
φ_S	Volume fraction of the small particles
φ_c	Volume fraction of particles in the crystal
φ_d	Volume fraction of particle in the dispersion phase
ζ	Zeta potential
σ	Standard deviation of particle size
γ	Surface tension
η	Dynamic viscosity of liquid phase
ρ	Density
τ	Time constant ion equation (2-20)
ψ	Global Orientational Order Parameter

LIST OF ABBREVIATIONS

bCC	Binary Colloidal Crystal
BSA	Bovine Serum Albumin
CCD	Charge Coupled Device
CGE	Capillary Gel Electrophoresis
CSA	Colloidal Self-Assembly
DC	Direct Current
DLS	Dynamic Light Scattering
DNA	Deoxyribo Nucleic Acid
EDL	Electrical Double Layer
EOF	Electro Osmotic Flow
fcc	Face Centered Cubic
FITC	Fluorescein IsoThioCyanate
fps	Frame Per Second
GLAD	glancing Angle Deposition
hcp	Hexagonal Close Packed
IHEISA	Isothermal Heating Evaporation Induced Self-Assembly
LbL	Layer-by-Layer
mCC	Monomodal Colloidal Crystal
MS	Mass Spectrometry
NMR	Nuclear Magnetic Resonance
PDMS	Poly(DimethylSiloxane)
POC	Point-Of-Care
RDF	Radial Distribution Function
rhcp	Random Hexagonal Close Packed
rhcp	Random hexagonally close-packed
SANS	Small Angle Neutron Scattering
SDS	Sodium Dodecyl Sulfate
SEM	Scanning Electron Microscopy
TAS	Total Analysis Systems
TBAB	Tetra-n-ButylAmmonium Bromide
TBE	Tris-Borate-EDTA
vdw	Van der Waals

CHAPTER 1

INTRODUCTION

1.1 Introduction

Protein separation is an indispensable technology for quantifying and identifying species present in complex sample mixtures. It is used for the discovery of protein biomarkers for diseases, development of protein related drugs and probing molecular aspects of life processes and disease and is an ongoing research field.[1, 2] The advent of miniaturization and the concept of total analysis systems (TAS)[3] in 1990 by Manz et al. and the following pioneering developments in the laboratories of Harrison[4-7], Ramsey[8-10] , Mathies[11-13] and Whitesides[14-16], has rendered the impact of this technology on life-sciences more significant due to the short analysis times, small amounts of samples and the ability to integrate and automate processes. Separation of these biological molecules with electrokinetic microfluidic chips has found numerous applications embracing clinical and pharmaceutical,[17-21] food and agricultural[22-25] as well as proteomic analysis.[26-28] Detection and quantifying urinary albumin protein, a well-known risk factor of diabetic nephropathy and cardiovascular disease[18], diagnosis of different levels of head trauma[19] and rapid detection of proteinaceous disease biomarkers[29] are a few exciting examples of the application of protein separation in human health sciences.

In recent years there has been a growing interest[30-36] in the coupling of protein separation by electrophoresis with mass spectrometry (MS) to accurately identify and characterize proteins in biological samples, which may present a very complex nature at low concentrations, or be available in very limited amounts. In contrast to MS, which has undergone pronounced advances since its emergence, the separation of proteins as the first stage of detection is still considered a bottleneck[37, 38] in terms of challenges in separation performance and automation.

Discrimination of different proteins exclusively by their size, using electrophoresis, is at the heart of protein separation technology. Amongst "invented-to-date" separation modes for protein electrophoresis in microfluidic chips, capillary gel electrophoresis (CGE) is perhaps the most popular [30] approach in which a gel or a polymer matrix is applied as the sieving media.[39] Size fractionation of biomolecules has remained a dynamic research field due to the complex nature of analyte-matrix interactions, which is at the core of electrophoretic separations.[40] Artificial sieving media have proven to give reliable, flexible and tunable structures that can be precisely engineered at micro and nano scales.[41-49] Thanks to their ordered and well-characterized structures, they can indeed be reliably and readily employed for systematic studies of the dynamics of biomolecules under nano-scale confinement, as well as for probing different bioseparation mechanisms.

1.2 Motivations and Scope

Study of the mechanism and dynamics of protein molecules during electrophoretic separation, in order to achieve high quality separations suitable for commercial clinical and point-of-care (POC) diagnosis, is an open and challenging field of research worldwide. The quality of a protein separation is dependent on the separating matrix, the conditions under which the electrophoresis is run and the properties of the molecule being separated. This research is centered on developing the matrix.

Previously, a microfluidic colloidal self-assemble (CSA) approach was developed in the Harrison group in order to make monomodal colloidal crystals (mCC) for applications as nanoporous media. The structure had an average pore size ranging from about 140 to 25 nm, demonstrating a proof-of-concept for DNA and protein separation.[50-52] Applying the same approach later, the smallest achievable pore size was pushed to 15 nm in a systematic study of DNA dynamics in nanoscale confinement within mCCs.[53] Here we are embarking on the fabrication of nanoporous media, as separating matrices, with smaller mean pore sizes ranging from 3 to 11 nm. Smaller pore sizes should enable higher quality separation of proteins demonstrated initially by Zeng et al.[51]

The first objective of this thesis is to explore a new microfluidic approach for the fabrication of binary colloidal crystals (bCC) made from mixtures of monodisperse particles with two distinct sizes. Several studies of mCC growth with different pore sizes were also performed in order to develop a new approach for the fabrication of silica bCCs featuring a pore size of 11 nm. The bCC structures were compared to mCC structure in terms of separation performance, and lattice structure.

As the size of proteins in a sample mixture shrinks, the pore size needed to separate them will also shrink, since friction in the pores controls the separation and friction is enhanced when the pore size is close to the molecular scale. In attaining smaller pore sizes than 15 nm, the nano structure of the sieving matrix develops cracks and totally dried areas at the micro scale, which is quite detrimental to the separation. Fabrication of mCC and bCC structures that are totally free of the inherent micron sized cracks and air-invaded areas was the other major objective of this thesis.

1.3 Colloidal Self-Assembly

Self-assembly[54], spontaneous organization of components of a system without human intervention, is an essential part of nanotechnology that can be applied to fabricate ensembles of nanoporous structures with engineered pore architecture and size distribution. This method can be recruited as a bottom-up[55] approach, as shown in Figure 1-1, to assemble billions of individual molecules or nanoparticles together, as building blocks, leading to the creation of three-dimensional compartments that feature a crystalline behavior. Figure 1-2 depicts the size spectrum where this spontaneous phenomenon can occur. Accordingly, self-assembly can happen from atomic to macroscopic scales.

In colloidal self-assembly (CSA), particles are used as mesoscopic building blocks to fabricate structures. Compared to standard fabrication techniques, like optical lithography, self-assembly offers a cheap, easy, faster and flexible route.[56]

One of the most studied applications of colloidal crystals in the literature has been in photonics[57, 58]. When the sizes of particles become comparable to the wavelengths of light, they strongly interact with it, confining and controlling photons of a specific wavelength. Hence propagation of light of a given wavelength can be blocked by the organized structure of particles in a lattice.[55] An example of a colloidal crystal made in this study by using particles 30 nm in diameter is depicted in Figure 1-3. The colorful nature upon normal incidence of light is in fact proof of the crystalline nature of the structure.

In a typical CSA process, particles undergo four phases, namely suspension, migration (towards the packing area), crystallization and drying/fixation. Each individual particle experiences different kinds of interactions until it is assembled at the crystallization point. The final fabricated structure is an overall result of a complex balance of these forces, attractive or repulsive, acting on each particle. It is noteworthy that the repulsive force between the assembled particles must be strong enough to avoid local aggregations, i.e. caused by van der Waals forces, leading to amorphous structures. At the same time it must be small enough not to hinder the self-assembly process that tries to organize particles in a closed-pack style.[55, 56] The quality of the final structure, particle deposition and colloidal suspension stability are all dependent on these colloidal forces.[55, 59]

The advantages brought by these nanoparticle arrays, including narrow pore size distribution, tunable morphology, mechanical stability and capability of incorporation with microfluidics, make them an excellent candidate to be considered for a molecular-level study of sized-base bioseparation.

1.4 Nanofabrication by Colloidal Self-Assembly

Colloidal crystals have been the focus of numerous studies for about five decades in many different fields of science, including photonic technologies[60-66], cancer studies[67-72], tissue engineering[73-78] and bioseparation[50-53, 79]. This interest is due to the unique and highly flexible structural properties colloidal crystals present at the nano scale and, most importantly, the ease of the fabrication techniques invented to date, which can enable their mass production.

1.4.1.1 Fabrication of monomodal colloidal crystals

One of the methods of fabricating colloidal crystals is the use of gravity to direct particles towards the crystalline locations.[80] Miguez et al.[81, 82] proposed a sedimentation approach for the assembly of 260 nm particles which was quite slow, taking weeks to complete the lattice. Mei et al.[83] applied a centrifugation method to hasten the fabrication process for silica particles of 200, 330 and 460 nm in diameter, but the method was not reliable enough to ensure face centered cubic structures (fcc). In techniques based on sedimentation, crystallization occurs over a period of several days to weeks depending on the sedimentation rate, where particles are directed towards thermodynamically low energy locations forming layers of particles packed in a hexagonal fashion.

Joannopoulos[84] at 1998 proposed a vertical approach to nano-engineer a crystal made from silicon were the mCC of silica particles was used as a template. Followed by Jiang et al.[85], to date, there have been different versions of this method adopted by several authors.[86-89] In this method a microslide is vertically placed in a suspension solution of monodisperse particles. Evaporation of the solvent triggers the emergence of a meniscus at the solvent, particle and microslide interface where particles are deposited on the slide. Depending on the particle volume fraction, rate of solvent evaporation and the type of solvent used[90], the thickness and the quality of the crystalline layer of particles could be easily controlled. This method suffers from the effect posed by the sedimentation phenomena when used with large particles. This problem has been solved in a method called isothermal heating evaporation-induced self-assembly (IHEISA)[89] by introducing a temperature gradient to make a convective flow to keep the sedimenting particles suspended. Silica particles of 635 nm, 850 nm and 1 μm were successfully self-organized in highly ordered multilayers of crystals in an hour.

Use of an external electrical field is another approach in which charged colloidal particles are directed towards crystallization sites via their electrophoretic mobilities and are compressed together, creating a densely packed lattice.[91, 92] In a study by Wen et al.[92] it was discovered that by tuning the ratio of the magnitudes of the magnetic and the electric field they are able to make crystals having either of the body centered tetragonal or face centered cubic (fcc) orientation.

Monolayer and multilayer crystals of monodisperse silica particles have also been fabricated by the Langmuir–Blodgett method.[93-96] In this method, ionic surfactants are used to make monolayers of floating particles that are transferred to the substrate via a vertical deposition approach. It was found that the quality of the crystals could be tuned by different choices of surfactants, their concentrations and also the type of the solvent used.

Wang and Gu[97] proposed a new method that relies on a self-assembly of silica particles on the water-air interface. The surfaces of these particles were modified by physical adsorption of cationic surfactant or chemical grafting of alkyl chains with silane coupling agents. The surface modified particles were then transferred from an aqueous phase to an organic one where monolayers of silica particles could be achieved by adjusting the balance of hydrophobic/hydrophilic nature of the particles. These assemblies were capable of being transferred onto a substrate in a layer-by-layer fashion, making three dimensional lattices.

Recently several research groups have come up with new microfluidic approaches to grow colloidal crystals in a microchannel. High quality artificial opals grown in a microchannel was firstly achieved in late 1990's [98-101] where colloidal self-assembly was used to fabricate lattices that were later employed as templates for the fabrication of inverse structures, by dissolving the initial colloidal particles away. This method offers a reliable approach without use of any machinery however, it took a long time.

An alternative method employed by Lee et al.[102] was based on a centrifugal microfluidics, where the external strong body force produced by centrifugation facilitates particle assembly in a microfluidic channel in less than an hour. Furthermore, the centrifugal force accelerates flow of the solvent through the growing nanoporous lattice, accelerating the process of self-organization.

Earlier a microfluidic approach was suggested[103-105] that used nitrogen flow to push the colloidal dispersion towards the evaporation ports, where particles were held within the microfluidic cell when their sizes were larger than the size of the ports. Application of a hydrodynamic pressure, pressing the particles together, with a continuous sonication during the course of the CSA produced high quality crystals of particles within the confinement of the microfluidic chip.

A convective mechanism for the production of two-dimensional closed packed and non-closed packed colloidal structures was suggested by Kumacheva et al.[106] In this approach a flow-driven crystallization in the confined geometry of a microchannel was studied. It was found that the ratio of the width of the microchannel to the size of particles was the determining factor on the number and type of grown lattices. In another similar study by Yin and Xia[107], capillary force and physical constraint of a microfluidic channel were combined to yield a generic approach for the self-assembly of particles into helical mesostructures with well-controlled functionalities.

1.4.1.2 Fabrication of binary colloidal crystals

Mixtures of suspended particles of two different sizes with appropriate size and number ratio can form colloidal crystals with various properties that cannot be attained in their monomodal counterparts. Changing the size and number ratio of the small to large particles can be used as a tuning tool to dictate the ultimate self-organized lattice, giving great flexibility.

Depending whether small and large particles are assembled at the same time or one-after-another renders the “invented-to-date” approaches into two major categories, namely a layer-by-layer (LbL) growth strategy[108] and a one-stage approach. In a typical method of LbL the crystal is made by layers of large and small particles sequentially stacked on top of each other, leading to a three-dimensional nanostructure. In this approach, the layer of the larger particle plays a template role for the consecutive layer of smaller particles, determining their ultimate locations upon assembly. However, in a typical one-stage method, a mixture of dispersed large and small particles is applied and the self-assembly process simultaneously co-crystallizes large and small particles into a three-dimensional structure. In the latter approach the applied small and large particles must have a specific number and size ratio, as otherwise the ordered property of the lattice will be sacrificed.

Within the LbL category, controlled drying[108], stepwise spin-coating[109] and confined convective assembly[86, 110] are the recently introduced techniques. In controlled drying, first proposed by Velikov and co-workers[108], a vertical deposition method, described before, was adopted to deposit a layer of the large particles. Sequentially, using the same approach, smaller particles were deposited on the larger particles. The first layer plays a template role for the subsequent layer of smaller particles. These monolayers of particles array can be deposited until the desired thickness of the colloidal crystal is achieved. This novel technique is sluggish, giving 1-2 mm per day of growth, challenging its applicability compared to the rapid stepwise spin-coating approach of Wang and Mohwald[109].

In the spin-coating method, individual monolayers of large and small particles are deposited on a horizontal substrate by a centrifugal force in a very short time in a stepwise manner. This method was first introduced in the 1980's by Deckman and Dunsmuir[111, 112] for the rapid fabrication of monomodal colloidal crystals. To facilitate uniform coating, the substrate needs to be fairly wettable by the colloidal dispersion. In some cases, the substrate is coated with a layer of surfactant to promote wetting. This method was recently employed by Sharma et al.[113] to fabricate binary colloidal crystals of oppositely charged particles. They produced ordered bCCs with different structural stoichiometries (i.e. LS_2 and LS_6) by use of Triton X-100, a non-ionic surfactant, that, by absorbing onto the surface of the polystyrene particles, imposes steric barriers to reduce short-range electrostatic attractions, thus avoiding micron-sized aggregations and disordered bCCs.

In another version of the LbL method, Kim et al [86, 110] used two vertical substrates, dipped into the colloidal dispersion, one of which is left static and the other one is moved upward. Hence colloidal particles are transported upwards, by an evaporation-induced convective flow, to the edge where the solvent evaporates away, leaving particles deposited at the meniscus location. By changing the colloidal volume fraction and lift-up rate they could manage to deposit two- or three-dimensional lattices of high quality.

In a recent LbL method developed by Singh and co-workers[114], a circular rubber ring is placed on the substrate, then a larger sized colloidal dispersion is injected into the space surrounded by the ring. Evaporation of the solvent initiated from the center point of the ring triggers crystallization of particles and entrainment of more particles due to an evaporation induced colloidal flow towards the crystallization zone, until all of the dispersion solvent content is evaporated, leaving colloidal particles crystallized on the substrate. A second layer of smaller particles is deposited on the previous layer, which acts as a template for the next layer. This deposition procedure can be continued until the desired thickness of the bCC is achieved.

Contact printing[115], self-assembly at an interface[116], horizontal deposition[117], vertical deposition[118, 119], use of oppositely charged particles and epitaxial growth with dielectrophoretic compression[60] are all examples of the one-step category. In self-assembly at an interface, a mixture of the small and large particles is prepared with a specific number and size ratio. The bimodal mixture is then injected onto a substrate surrounded by water. The mixture is then spread on the substrate until it reaches the surrounding liquid phase, where upon the suspension experiences strong surface tension effects that cause it to disperse onto the water around the substrate. The bimodal mixture is then self-assembled on the surface of the water.

In the horizontal deposition method introduced by Wang et al.[117] a mixture of small and large particles is placed on the surface of a substrate. The dispersion phase spreads all over the surface of the substrate and stops at the edges. Evaporation starts from the edges and triggers colloidal crystallization after a certain amount of water has evaporated. This evaporation process induces flow of solvent, due to capillary action of the water bridges between the neighboring particles, bringing floating particles to the crystallization zone where they are self-organized into closed-packed structures. By tuning the number ratio of small to larger particles, bCC structures of LS_2 and LS_6 could be fabricated in a fairly short amount of time.

The vertical deposition method[118-121] applies the same method as was described before for the fabrication of mCCs except that a mixture of small and large particles is used.

Recently van Blaaderen's group[122] has shown that oppositely charged particles can be self-assembled into various bCC configurations. They used Tetra-n-butylammonium bromide (TBAB) salt to control the particle charges. At different salt ionic strengths, different crystals could be fabricated.

Vermolen et al.[60] could control the orientation of the bCC by applying an external electric-field gradient on a structured wall, also referred to as epitaxial growth, and obtained thick, oriented, pure NaCl crystal lattice structures. In this method the effect of gravity on separating the small and large particles were counterbalanced by applying an oscillating electric field of 30 V, which imposes a compression force on the dispersed particles between the two electrodes, self-organizing them onto a substrate that has the epitaxial patterns directing the crystallization.

1.5 Recent Trend in Protein Separation

Today the most common mode of separation of proteins by electrophoresis is performed using polyacrylamide or agarose gel as sieving matrix. Considering the advantages brought by the microfluidic era, incorporation of the old technology to the miniaturized systems suggests many critical applications that could profit relevant bioanalytical research. This was demonstrated for the first time by

Effenhauser and his co-workers.[123] Herr and Singh also performed a high performance separation of five proteins on a polyacrylamide gel in a microfluidic channel in less than 30 seconds, much faster than the conventional approach.[39] They studied the effect of pore size and electrical field strength upon the performance of separation. Oliver at al.[124] performed the same kind of analysis and investigated the mechanism of protein separation at different gel concentrations. Nagata et al.[125] investigated the reason for poor separation of SDS-denatured proteins during electrophoresis in a polymethylmethacrylate (PMMA) gel in a plastic microchip, then proposed an effective way for separation of three proteins in less than 20 seconds. In another study by the same research group the conditions of electrophoretic separation of proteins, ranging in molecular weights from 21.7-116 kDa, was optimized and separation was achieved in less than 10 seconds.

With the advent of colloidal self-assembly, and the use of colloids for making structures with tunable narrow pore size distribution and flexible ordered/disordered morphologies, as opposed to what is attainable by use of any kinds of gel, bioseparation started a new trend.

Zeng and Harrison[51] showed for the first time that a colloidal crystal can be fabricated in a microfluidic channel via CSA using silica particles of 160 nm diameter. The sieving matrix with an average pore size of about 25 nm, was used to separate five proteins with molecular weights ranging from 20.1 to 116 kDa within a few minutes, reliably and reproducibly. Based on the measured mobilities, a governing SDS-protein complex electromigration was diagnosed. In a recent study by Wirth's research group[38] lattices of silica particles of 330 nm was made in a microcapillary and used to investigate an electrochromatographic protein separation. The high efficiency achieved demonstrated the importance of homogeneity of the sieving media, and the potential for miniaturization and lab-on-a-chip applications. In another study by the same research group[126], the effects of the lattices of chemically modified silica particles of 900 nm, packed in a capillary, upon a field-free remobilization of three proteins were investigated.

1.6 Fundamentals of Electrophoresis

When two platinum electrodes are placed in an electrolyte and both are connected to a power supply, an external electrical field will be established. Any object that has electrical charge at the surface, like a protein molecule, moves with respect to the surrounding liquid electrolyte. This phenomenon, discovered by Reuss at 1807, is called electrophoresis.

Any charged object in an electrolyte, a solution with free ions, perturbs the distribution of ions in the surrounding solution and is equilibrated by a balance between electrostatic and Brownian forces. This re-distribution of ions forms an electrical double layer (EDL) as per Figure 1-4. The first layer is comprised of ions having opposite charge compared to the charges on the surface of the object. This immobile layer is called the Stern layer with a potential of Ψ_d. All other free ions that are distributed beyond the Stern layer form a thicker layer that is called the diffuse layer. Between the Stern layer and the outside edge of diffuse layer there is a boundary before which all ions are immobile, the shear plane. The exact location is not defined. The electrical potential at this plane is called the electrokinetic or more commonly the zeta potential, ζ.[127]

The thickness of the EDL, a property of the electrolyte solution, based on the Debye-Huckel equation can be estimated via the following equation

$$\kappa^{-1} = \sqrt{\frac{\epsilon k_b T}{2e^2 I}} \qquad 1\text{-}1$$

where ϵ is the dielectric permittivity of the electrolyte solution, k_b is the Boltzmann constant and e is the elementary charge. The ionic strength, I, is calculated by $I = \frac{1}{2}\sum_{i=1}^{m} z_i^2 n_i$ with z_i, n_i and m being valence, density of the i$^{\text{th}}$ ion and total number of ions, respectively.

When a negatively charged object immersed in an electrolyte is subjected to an external electrical field, $\vec{\boldsymbol{E}}$, both the object and its surrounding cloud of ions start to move towards the electrode that has the opposite type charge. i.e. negatively charged proteins towards anode and the surrounding cations towards cathode. Hence there would be a hydrodynamic interaction between the object and its surrounding ions. The free solution electrophoretic mobility, of the charged object is defined as[40]

$$\mu = \frac{|\vec{\boldsymbol{V}}|}{|\vec{\boldsymbol{E}}|} \tag{1-2}$$

where $\vec{\boldsymbol{V}}$ is the velocity of the migrating object[1]. Based on the thickness of the EDL two limiting cases have been considered. First, when the EDL thickness is larger than the object, i.e. $\kappa^{-1} \gg R_g$, the electric and viscous forces equilibrate each other; hence the mobility can be estimated via[40]

$$\mu = \frac{Q}{f} \tag{1-3}$$

where Q is the total charge and f is the friction coefficient calculated by

$$f = 6\pi\eta R \tag{1-4}$$

where η and R are the viscosity of solvent, and radius of the object respectively.

The second limiting case includes the Smoluchowski model, the mobility for the case when the Debye length is very thin compared to the object size, i.e. $\kappa^{-1} \ll R_g$, can be estimated by[40]

$$\mu = \frac{\epsilon\phi_0}{\eta} \approx \frac{\sigma'\kappa^{-1}}{4\pi\eta} \tag{1-5}$$

where ϕ_0 and σ' are the surface potential and charge density, respectively. In this regime the mobility is not dependent on particle size.

---

[1] Consistent with the current literature in this field the free solution electrophoretic mobility will be referred to as simply the mobility.

1.7 Electro Osmotic Flow

Flow of an electrolyte with respect to a charged stationary wall or porous media due to the application of external electrical field is called electro osmotic flow (EOF). In the case of microfluidics, the deprotonation of the silanol groups present at the surface of the PDMS, glass substrate and silica particles in the lattice, at pH > 2 of the running buffer, creates negative charge on the surface. As a result, during electrophoresis the electrical double layers that develop near these surfaces induce EOF of the electrolyte from anode to cathode. This EOF is mainly caused by the movement of hydrated cations, which are in excess compared to anions in the diffuse layer, imposing viscous drag and hence transporting the momentum onto the surrounding electrolyte solution. The mobility of EOF is estimated via

$$\mu^{EOF} = -\frac{\epsilon\zeta}{\eta} \tag{1-6}$$

where ζ is the zeta potential and η and ϵ are the viscosity and the dielectric permittivity of the solution, respectively.

In electrophoresis within a negatively charged capillary, EOF is towards the cathode, opposing movement of a negatively charged SDS coated-protein towards the anode. Hence, the elution times of the analyte will be delayed. Since EOF is dependent on the zeta potential, different lattices made from different particles, which probably having different zeta potentials, present different levels of EOF.

Hence a systematic study of proteins migrations in different pore sizes might be challenging, since the mobilities of proteins are affected by two parameters, pore size and EOF.

Another disadvantage caused by the presence of EOF during electrophoresis is a change of the liquid phase hydrostatic head in the reservoirs of the microfluidic chip due to flow of buffer into or out of the reservoirs. This effect brings unequal liquid levels into the reservoirs of the chip, which causes flow due to differences in the hydrostatic heads present in the reservoirs. This flow has a parabolic laminar nature that incurs dispersion of the analyte due to the broad range in the velocities, which is tantamount to uncontrolled separation conditions.[128] Fortunately this problem is not significant except for run times exceeding several hours.

The high surface-to-volume ratios created by the colloidal crystals in the microfluidic channel, and use of a running buffer with sufficiently high ionic strength to lower the zeta potential magnitude, suppresses EOF to a high extent. Another way of eliminating the EOF has been through surface treatments.[129]

1.8 Size-Based Protein Separation

Protein molecules have different electrical charges and unique native shapes determined by hydrogen, hydrophobic and disulfide linkages of different branches on the backbone the protein. They are denatured in the presence of heat and/or a detergent, such as sodium dodecyl sulfate (SDS). This first covers them with a uniform negative charge invoked by SDS molecules that bind to the protein backbone on a basis of ~1.4 $\frac{\text{gr SDS}}{\text{gr protein}}$; and secondly, destroys their unique native folded structure, giving flexible, more soluble structures that take random coil conformations.[130-133] Figure 1-5 schematically depicts both native and SDS-denatured states of a typical protein. As a consequence of denaturation, and electrophoresis in a buffer of concentrated more than 100 mM[40], e.g. 356 mM in this study, the double layer surrounding a negatively charged SDS-protein complex will be suppressed to a few nanometers. Therefore the electrophoretic mobilities can be estimated via the Smoluchowski model, equation 1-5.

Furthermore, the charge-to-mass ratios of different SDS-denatured protein complexes after the denaturation process will, regardless of their size, incur a constant charge-to-friction ratio and, hence, constant free solution electrophoretic mobility according to equation 1-5. When these globular objects move in the presence of an external electrical field with the same velocity, they cannot be fractionated, since they migrate with the same mobility. As a result, the medium has to be filled with a sieving matrix that imposes size-dependent steric interactions with the SDS-protein complexes, leading to separation based solely on their sizes.

There have been many studies of DNA migration in a porous media, in contrast to SDS-denatured protein molecules that have not been studied on as deeply. However, the mechanism of protein separation at the molecular level in a sieving matrix, i.e. colloidal crystal in this study, is reasonably described by the proposed migration mechanisms for the DNA separation since DNA molecules, like SDS-protein complexes, have size-independent charge-to-mass ratio values[124] and also SDS-protein complexes are flexible polymer chains[131, 133], similar to what is believed to be the case for DNA molecules.

Three different mechanisms have been proposed for the migration of DNA molecules through a confined geometry. These mechanisms are categorized according to the ratio of the radius of gyration, root-mean-squared of all the atoms in the molecule from the molecular center of mass[134], and the pore size.

The first mechanism considers the SDS-protein complexes as globular objects[131, 133] with a hydrodynamic radius smaller than the pore size of the colloidal crystal, which then migrate through the lattice without any conformational changes, c.f. Figure 1-6a. Based on this Ogston sieving model, the logarithm of the electrophoretic mobility of the SDS-protein objects are proportional to their molecular sizes. i.e. $\ln \mu \propto -M$[135, 136]. Fitting to this model identifies if it is the correct regime, and can be used to identify molecular weights with appropriate standards available.

Within the Ogston regime no molecule with a size larger than the pore size would penetrate the sieving matrix. However, experimental evidence proves the opposite.[124, 131, 133] Hence, there is another mechanism at work, the reptation of flexible thin objects formed by uncoiling the globular molecule. Accordingly, molecules can still enter the lattice moving via a snake-like motion oriented along the electrical field, c.f. Figure 1-6b. In the reputation regime the logarithm of the mobility of the SDS-protein complexes is proportional to the logarithm of the molecular weights. i.e. $\ln \mu \propto -\ln M$. Hence a log-log plot of mobilities versus molecular weights should have a negative unit slope at the limit of very small electric field strength.[137, 138]

By applying higher electrical voltages a biased reptation motion with stretching of the flexible chain occurs, shown in Figure 1-6c, rendering higher mobilities than the former case. In this regime the conformable globular complexes are turned into rode-like shapes with mobilities that do not follow the very low electrical field scenario. Lumpkin[139] discovered that mobilities will be also governed by the magnitude of the electrical field. i.e. $\mu \propto \frac{1}{M} + bE^2$ where b is a function of the mesh size of the lattice network, charge and segment length of the migrating species and E is electrical field strength.[137, 138] Figure 1-6c illustrates the concept that the existing coils along the body of the migrating chain are totally elongated due to the effect of higher field strength.

1.9 Thesis Outline

In the current chapter, a brief overview of protein separation technology and the motivation behind it is provided. Furthermore, objectives of this thesis and the literature review are discussed.

In chapter 2 an experimental approach for the study of the dynamic growth of monomodal colloidal crystals is suggested and used to probe macroscopic behavior of autonomous crystal growth phenomena of two different kinds of particle systems, polystyrene and silica. A mathematical model was adapted to better understand the underlying physics behind the microfluidic CSA approach. The model shows strong agreement with the experimental results for polystyrene, but fell well short of describing the growth behavior observed for the silica system. According to a hydrodynamic simulation of the microchip reservoir, and the particle number gradient captured from the SEM analysis, the poor agreement with the silica system was then attributed to the effect of sedimentation on the composition of the silica supply suspension. The model was modified via introducing an exponential factor on the characteristic time of the system. The exponential factor showed a decremental trend as particle sizes decreased. Inspired by the outcome of this study, binary colloidal crystals of polystyrene were made following the original approach, with specific particle number and size ratios. A periodic chip rotation strategy was proposed to counterbalance the effect of gravity during self-assembly of binary colloidal crystal of the silica system, and bimodal crystals were the grown.

Chapter 3 embarks on fabrication of bCCs and mCCs having sub-20 nm scale porous structures. According to the initial observations, emergence of micro scale cracks and air-invaded spots were inevitable as the sizes of crystal building blocks, the assembling particles, shrank to 50 or 30 nm using the original microfluidic CSA approach.[51] The formation of cracks that then incur channeling phenomena excludes the sieving effect of the matrix. The origin of these cracks was believed to be bed shrinkage and hence build-up of internal stress, due to the capillary action during CSA, given the structure itself is adhered to the surrounding microchannel boundaries. Decreasing the speed of the CSA process was a huge alleviating factor in favor of avoiding cracks. The air-invasion problem is imposed due to faster diffusion of water at the drying front compared to its bulk transfer through the nanoporous structure. In fact, as the pore size shrinks to a few nanometers, e.g. 3 nm, the viscous resistance forces against its fluid transfer gets more serious; so much so that part of the structure becomes completely dried, as enough replenishing water cannot be transferred to compensate for the loss due to evaporation. These two problems were tackled by decreasing the water evaporation rate placing the microfluidic chip in an environment with controlled humidity. The electrophoretic mobilities of proteins, including trypsin inhibitor (MW: 20.1 kDa), ovalbumin (45 kDa) and bovine serum albumin (66 kDa), measured in the fabricated mCC and bCC described above, revealed an Ogston regime to be the governing separation mechanism during chip electrophoresis. Anomalous observations in the smallest sizes made with 50 nm particles suggest the onset of a reptation separation regime.

Chapter 4 concludes the thesis by presenting the outcome of the project and a discussion over the envisaged future perspectives and plants.

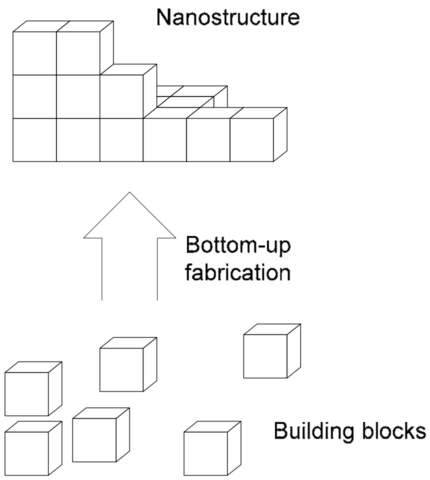

Figure 1-1 Demonstration of the bottom-up approach.

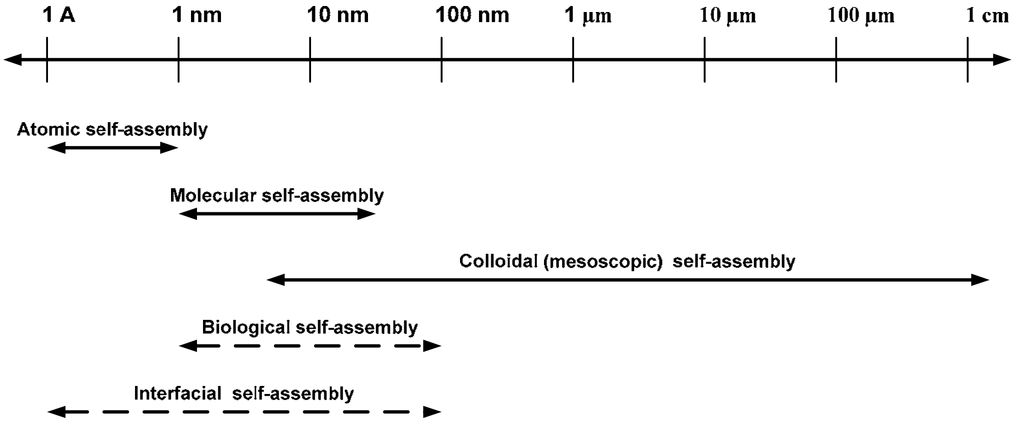

Figure 1-2 Classification of self-assemblies based on the size and nature of the building blocks as well as where it occurs.

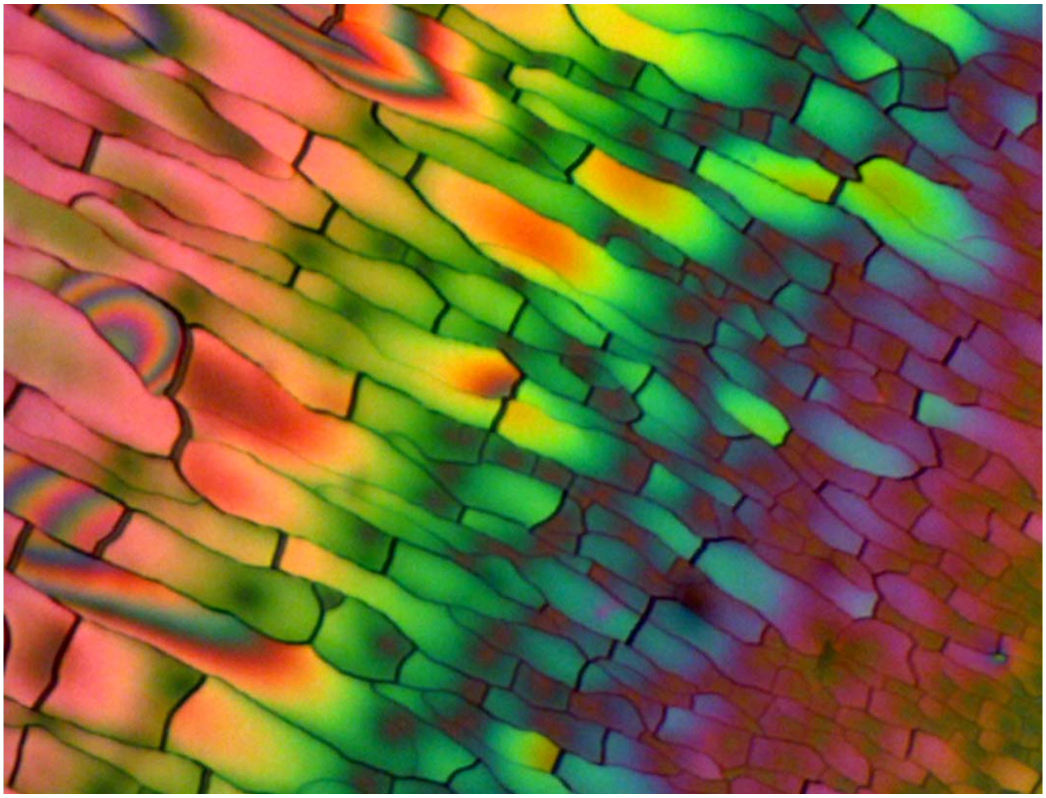

Figure 1-3 Demonstration of Bragg diffraction phenomena featured by crystal of silica nanoparticles of 30 nm fabricated via colloidal self-assembly in this study.

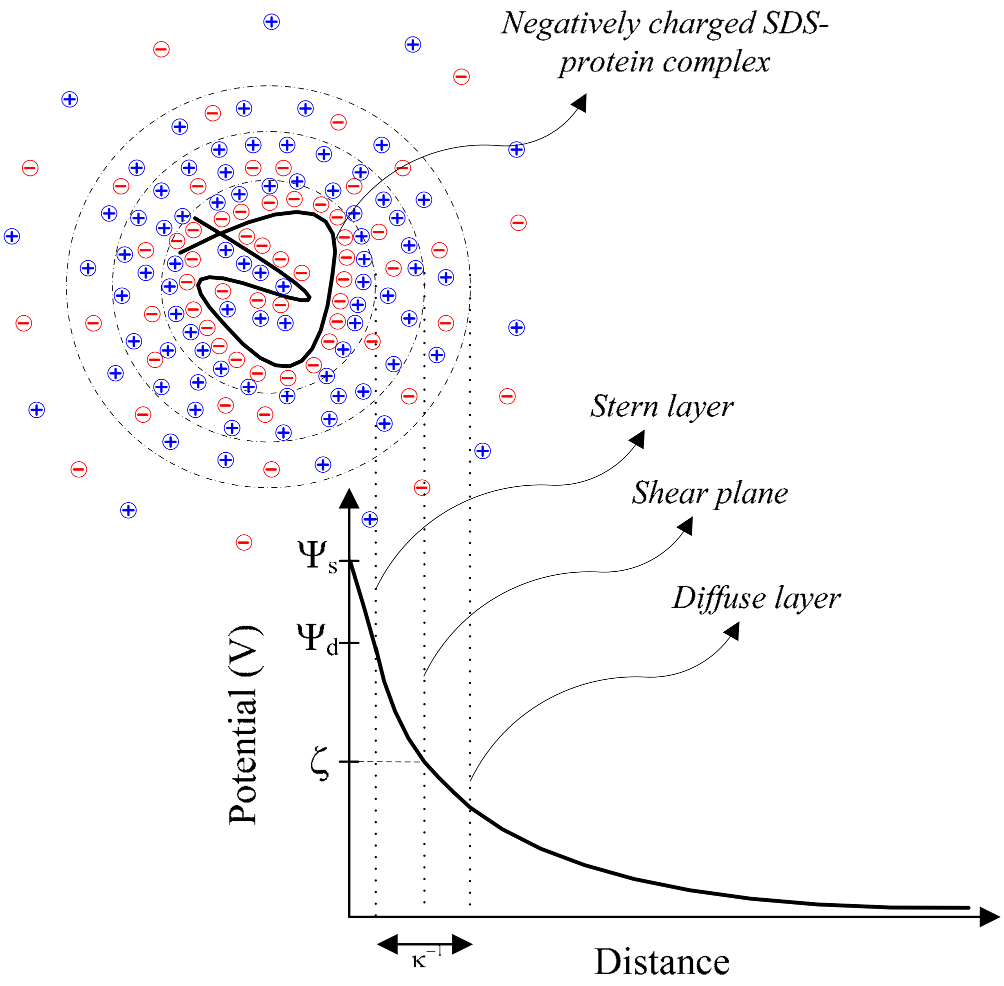

Figure 1-4 Schematic view of a negatively charged protein immersed in an electrolyte. Below indicates the profile of the electrical potential illustrating the Debye length, κ^{-1}, the zeta potential, ζ and different layers away from the surface of the complex.

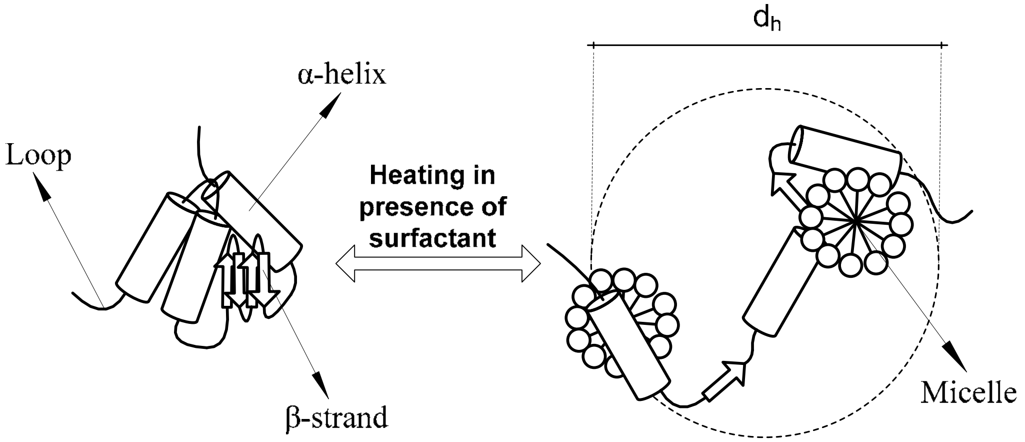

Figure 1-5 Schematic representation of the structure of a native (left) and an SDS-denatured protein (right).[140] d_h is the hydrodynamic diameter.

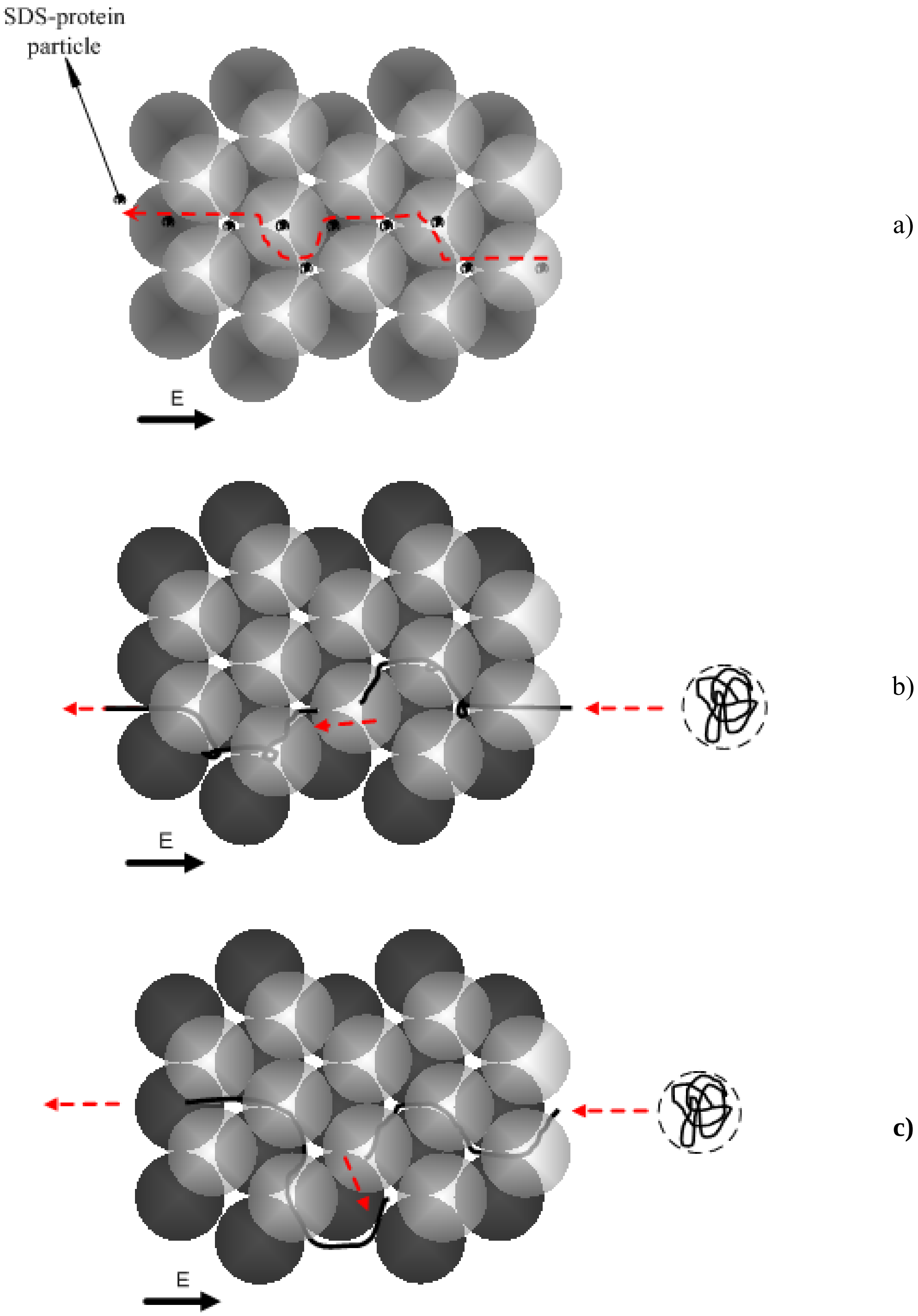

Figure 1-6 Different regime of migrations in the presence of an external electrical filed. a) Ogston regime b) Reputation without orientation c) Reputation with orientation.

1.10 References

[1] Wang, X., Wei, X., Thijssen, B., Das, J., Lipkin, S.M., Yu, H. *Nature Biotechnology* **2012**, *30*, 159–164.

[2] Henkel, A.W., Muller, K., Lewczuk, P., Muller, T., Marcus, K., Kornhuber, J., Wiltfang, J. *Journal of Neural Transmission* **2012**, *119*, 779–788.

[3] Manz, A., Graber, N., Widmer, H.M. *Sensors and Actuators: B. Chemical* **1990**, *1*, 244–248.

[4] Harrison, D.J., Fluri, K., Seiler, K., Fan, Z., Effenhauser, C.S., Manz, A. *Science* **1993**, *261*, 895–897.

[5] Liang, Z., Chiem, N., Ocvirk, G., Tang, T., Fluri, K., Harrison, D.J. *Analytical Chemistry* **1996**, *68*, 1040–1046.

[6] Fluri, K., Fitzpatrick, G., Chiem, N., Harrison, D.J. *Analytical Chemistry* **1996**, *68*, 4285–4290.

[7] Chiem, N., Harrison, D.J. *Analytical Chemistry* **1997**, *69*, 373–378.

[8] Kutter, J.P., Jacobson, S.C., Matsubara, N., Ramsey, J.M. *Analytical Chemistry* **1998**, *70*, 3291–3297.

[9] Khandurina, J., Jacobson, S.C., Waters, L.C., Foote, R.S., Ramsey, J.M. *Analytical Chemistry* **1999**, *71*, 1815–1819.

[10] Jacobson, S.C., Culbertson, C.T., Daler, J.E., Ramsey, J.M. *Analytical Chemistry* **1998**, *70*, 3476–3480.

[11] Woolley, A.T., Mathies, R.A. *Analytical Chemistry* **1995**, *67*, 3676–3680.

[12] Liu, S., Shi, Y., Ja, W.W., Mathies, R.A. *Analytical Chemistry* **1999**, *71*, 566–573.

[13] Simpson, P.C., Roach, D., Woolley, A.T., Thorsen, T., Johnston, R., Sensabaugh, G.F., Mathies, R.A. *Proceedings of the National Academy of Sciences of the United States of America* **1998**, *95*, 2256–2261.

[14] McDonald, J.C., Duffy, D.C., Anderson, J.R., Chiu, D.T., Wu, H., Schueller, O.J.A., Whitesides, G.M. *Electrophoresis* **2000**, *21*, 27–40.

[15] Sia, S.K., Whitesides, G.M. *Electrophoresis* **2003**, *24*, 3563–3576.

[16] McDonald, J.C., Whitesides, G.M. *Accounts of Chemical Research* **2002**, *35*, 491–499.

[17] Roper, M.G., Shackman, J.G., Dahlgren, G.M., Kennedy, R.T. *Analytical Chemistry* **2003**, *75*, 4711–4717.

[18] Chan, O.T.M., Herold, D.A. *Clinical Chemistry* **2006**, *52*, 2141–2146.

[19] Phillips, T.M. *Electrophoresis* **2004**, *25*, 1652–1659.

[20] Giordano, B.C., Jin, L., Couch, A.J., Ferrance, J.P., Landers, J.P. *Analytical Chemistry* **2004**, *76*, 4705–4714.

[21] Colyer, C.L., Mangru, S.D., Harrison, D.J. *Journal of Chromatography A* **1997**, *781*, 271–276.

[22] Schulze, P., Ludwig, M., Kohler, F., Belder, D. *Analytical Chemistry* **2005**, *77*, 1325–1329.

[23] Monti, G., De Napoli, L., Mainolfi, P., Barone, R., Guida, M., Marino, G., Amoresano, A. *Analytical Chemistry* **2005**, *77*, 2587–2594.

[24] Uthayakumaran, S., Batey, I.L., Wrigley, C.W. *Journal of Cereal Science* **2005**, *41*, 371–374.

[25] Uthayakumaran, S., Listiohadi, Y., Baratta, M., Batey, I.L., Wrigley, C.W. *Journal of Cereal Science* **2006**, *44*, 34–39.

[26] Kustos, I., Nyul, A., Lorand, T., Kocsis, B., Kilar, F. *Journal of Biochemical and Biophysical Methods* **2006**, *69*, 57–65.

[27] Nawarak, J., Sinchaikul, S., Wu, C.-Y., Liau, M.-Y., Phutrakul, S., Chen, S.-T. *Electrophoresis* **2003**, *24*, 2838–2854.

[28] Tabuchi, M., Kuramitsu, Y., Nakamura, K., Baba, Y. *Journal of Proteome Research* **2003**, *2*, 431–435.

[29] Herr, A.E., Hatch, A.V., Throckmorton, D.J., Tran, H.M., Brennan, J.S., Giannobile, W.V., Singh, A.K. *Proceedings of the National Academy of Sciences of the United States of America* **2007**, *104*, 5268–5273.

[30] Peng, Y., Pallandre, A., Tran, N.T., Taverna, M. *Electrophoresis* **2008**, *29*, 157–178.

[31] Musyimi, H.K., Guy, J., Narcisse, D.A., Soper, S.A., Murray, K.K. *Electrophoresis* **2005**, *26*, 4703–4710.

[32] Wang, C., Oleschuk, R., Ouchen, F., Li, J., Thibault, P., Harrison, D.J. *Rapid Communications in Mass Spectrometry* **2000**, *14*, 1377–1383.

[33] Sung, W.-C., Huang, S.-Y., Liao, P.-C., Lee, G.-B., Li, C.-W., Chen, S.-H. *Electrophoresis* **2003**, *24*, 3648–3654.

[34] Tachibana, Y., Otsuka, K., Terabe, S., Arai, A., Suzuki, K., Nakamura, S. *Journal of Chromatography A* **2003**, *1011*, 181–192.

[35] Lazar, I.M., Li, L., Yang, Y., Karger, B.L. *Electrophoresis* **2003**, *24*, 3655–3662.

[36] Xu, Y., Little, M.W., Murray, K.K. *Journal of the American Society for Mass Spectrometry* **2006**, *17*, 469–474.

[37] Bogdanov, B., Smith, R.D. *Mass Spectrometry Reviews* **2005**, *24*, 168–200.

[38] Wei, B., Malkin, D.S., Wirth, M.J. *Analytical Chemistry* **2010**, *82*, 10216–10221.

[39] Herr, A.E., Singh, A.K. *Analytical Chemistry* **2004**, *76*, 4727–4733.

[40] Sartori, A., Barbier, V., Viovy, J.-L. *Electrophoresis* **2003**, *24*, 421–440.

[41] Huang, L.R., Silberzan, P., Tegenfeldt, J.O., Cox, E.C., Sturm, J.C., Austin, R.H., Craighead, H. *Physical Review Letters* **2002**, *89*, 178301/1–178301/4.

[42] Randall, G.C., Doyle, P.S. *Macromolecules* **2006**, *39*, 7734–7745.

[43] Fu, J., Yoo, J., Han, J. *Physical Review Letters* **2006**, *97*.

[44] Huang, L.R., Tegenfeld, J.O., Kraeft, J.J., Sturm, J.C., Austin, R.H., Cox, E.C. *Nature Biotechnology* **2002**, *20*, 1048–1051.

[45] Han, J., Craighead, H.G. *Science* **2000**, *288*, 1026–1029.

[46] Fu, J., Schoch, R.B., Stevens, A.L., Tannenbaum, S.R., Han, J. *Nature Nanotechnology* **2007**, *2*, 121–128.

[47] Chou, C.-F., Bakajin, O., Turner, S.W.P., Duke, T.A.J., Chan, S.S., Cox, E.C., Craighead, H.G., Austin, R.H. *Proceedings of the National Academy of Sciences of the United States of America* **1999**, *96*, 13762–13765.

[48] Huang, L.R., Cox, E.C., Austin, R.H., Sturm, J.C. *Science* **2004**, *304*, 987–990.

[49] Han, J., Turner, S.W., Craighead, H.G. *Physical Review Letters* **1999**, *83*, 1688–1691.

[50] Zeng, Y., He, M., Harrison, D.J. *Angewandte Chemie - International Edition* **2008**, *47*, 6388–6391.

[51] Zeng, Y., Harrison, D.J. *Analytical Chemistry* **2007**, *79*, 2289–2295.

[52] Zeng, Y., Harrison, D.J. *Electrophoresis* **2006**, *27*, 3747–3752.

[53] Nazemifard, N., Bhattacharjee, S., Masliyah, J.H., Jed Harrison, D. *Angewandte Chemie - International Edition* **2010**, *49*, 3326–3329.

[54] Whitesides, G.M., Grzybowski, B. *Science* **2002**, *295*, 2418–2421.

[55] Lee, Y. S. *Self-Assembly and Nanotechnology: A Force Balance Approach*; John Wiley and Sons, Inc., New Jersey, 2008.

[56] Li, F., Josephson, D.P., Stein, A. *Angewandte Chemie - International Edition* **2011**, *50*, 360–388.

[57] Xia, Y., Gates, B., Yin, Y., Lu, Y. *Advanced Materials* **2000**, *12*, 693–713.

[58] Xia, Y., Yang, P., Sun, Y., Wu, Y., Mayers, B., Gates, B., Yin, Y., Kim, F., Yan, H. *Advanced Materials* **2003**, *15*, 353–389.

[59] Li, Q., Jonas, U., Zhao, X.S., Kappl, M. *Asia-Pacific Journal of Chemical Engineering* **2008**, *3*, 255–268.

[60] Vermolen, E.C.M., Kuijk, A., Filion, L.C., Hermes, M., Thijssen, J.H.J., Dijkstra, M., Van Blaaderen, A. *Proceedings of the National Academy of Sciences of the United States of America* **2009**, *106*, 16063–16067.

[61] Lee, W., Pruzinsky, S.A., Braun, P.V. *Advanced Materials* **2002**, *14*, 271–274.

[62] Taton, T.A., Norris, D.J. *Nature* **2002**, *416*, 685–686.

[63] Tran, P. *Journal of the Optical Society of America B: Optical Physics* **1997**, *14*, 2589–2595.

[64] Weissman, J.M., Sunkara, H.B., Tse, A.S., Asher, S.A. *Science* **1996**, *274*, 959–960.

[65] Park, S.H., Xia, Y. *Langmuir* **1999**, *15*, 266–273.

[66] Lee, K., Asher, S.A. *Journal of the American Chemical Society* **2000**, *122*, 9534–9537.

[67] da Silva, J., Lautenschlager, F., Kuo, C.-H.R., Guck, J., Sivaniah, E. *Integrative Biology* **2011**, *3*, 1202–1206.

[68] da Silva, J., Lautenschlager, F., Sivaniah, E., Guck, J.R. *Biomaterials* **2010**, *31*, 2201–2208.

[69] Zhao, Y., Zhao, X., Pei, X., Hu, J., Zhao, W., Chen, B., Gu, Z. *Analytica Chimica Acta* **2009**, *633*, 103–108.

[70] Gates, B., Lu, Y., Li, Z.Y., Xia, Y. *Applied Physics A: Materials Science and Processing* **2003**, *76*, 509–513.

[71] Irvine, D.J., Stachowiak, A., Jain, S. *Materials Science Forum* **2003**, *426-432*, 3213–3218.

[72] Kolishetti, N., Dhar, S., Valencia, P.M., Lin, L.Q., Karnik, R., Lippard, S.J., Langer, R., Farokhzad, O.C. *Proceedings of the National Academy of Sciences of the United States of America* **2010**, *107*, 17939–17944.

[73] Cai, Z., Teng, J., Yan, Q., Zhao, X.S. *Colloids and Surfaces A: Physicochemical and Engineering Aspects* **2012**, *402*, 37–44.

[74] Wang, X., Wang, Y.-Y., Gu, Z.-Z., Huang, N.-P. Fabrication of nanostructured polymeric films and their geometric effects on cell growth. 2011.

[75] Shanbhag, S., Lee, J.W., Kotov, N.A. Modeling cell-matrix interactions and nutrient transport in cell scaffolds possessing inverted colloidal crystal geometry. 2005.

[76] Liu, Y., Wang, S., Lee, J.W., Kotov, N.A. *Chemistry of Materials* **2005**, *17*, 4918–4924.

[77] Zhang, Y., Wang, S., Eghtedari, M., Motamedi, M., Kotov, N.A. *Advanced Functional Materials* **2005**, *15*, 725–731.

[78] Lee, J., Kotov, N. Inverted colloidal crystals as tissue engineering scaffolds. 2004.

[79] Nazemifard, N., Wang, L., Ye, W., Bhattacharjee, S., Masliyah, J.H., Harrison, D.J. *Lab on a Chip - Miniaturisation for Chemistry and Biology* **2012**, *12*, 146–152.

[80] Vos, W.L., Sprik, R., Van Blaaderen, A., Imhof, A., Lagendijk, A., Wegdam, G.H. *Physical Review B - Condensed Matter and Materials Physics* **1996**, *53*, 16231–16235.

[81] Mi-guez, H., Meseguer, F., Lopez, C., Blanco, A., Moya, J.S., Requena, J., Mifsud, A., Fornes, V. *Advanced Materials* **1998**, *10*, 480–483.

[82] Mayoral, R., Requena, J., Moya, J.S., Lopez, C., Cintas, A., Mi-guez, H., Meseguer, F., Vazquez, L., Holgado, M., Blanco, A. *Advanced Materials* **1997**, *9*, 257–260.

[83] Mei, D., Liu, H., Cheng, B., Li, Z., Zhang, D., Dong, P. *Physical Review B - Condensed Matter and Materials Physics* **1998**, *58*, 35–38.

[84] Joannopoulos, J.D. *Nature* **2001**, *414*, 257–258.

[85] Jiang, P., Bertone, J.F., Hwang, K.S., Colvin, V.L. *Chemistry of Materials* **1999**, *11*, 2132–2140.

[86] Kim, M.H., Im, S.H., Park, O.O. *Advanced Functional Materials* **2005**, *15*, 1329–1335.

[87] Zheng, Z., Liu, X., Luo, Y., Cheng, B., Zhang, D., Meng, Q., Wang, Y. *Applied Physics Letters* **2007**, *90*.

[88] Vlasov, Y.A., Bo, X.-Z., Sturm, J.C., Norris, D.J. *Nature* **2001**, *414*, 289–293.

[89] Wong, S., Kitaev, V., Ozin, G.A. *Journal of the American Chemical Society* **2003**, *125*, 15589–15598.

[90] Li, H.-L., Marlow, F. *Chemistry of Materials* **2006**, *18*, 1803–1810.

[91] Trau, M., Saville, D.A., Aksay, I.A. *Langmuir* **1997**, *13*, 6375–6381.

[92] Wen, W., Wang, N., Ma, H., Lin, Z., Tam, W.Y., Chan, C.T., Sheng, P. *Physical Review Letters* **1999**, *82*, 4248–4251.

[93] Pieranski, P. *Physical Review Letters* **1980**, *45*, 569–572.

[94] Collier, C.P., Saykally, R.J., Shiang, J.J., Henrichs, S.E., Heath, J.R. *Science* **1997**, *277*, 1978–1981.

[95] Kurth, D.G., Lehmann, P., Lesser, C. *Chemical Communications* **2000**, 949–950.

[96] Szekeres, M., Kamalin, O., Schoonheydt, R.A., Wostyn, K., Clays, K., Persoons, A., DÃ©kÃ¡ny, I. *Journal of Materials Chemistry* **2002**, *12*, 3268–3274.

[97] Wang, W., Gu, B. *Journal of Physical Chemistry B* **2005**, *109*, 22175–22180.

[98] Yang, P., Deng, T., Zhao, D., Feng, P., Pine, D., Chmelka, B.F., Whitesides, G.M., Stucky, G.D. *Science* **1998**, *282*, 2244–2246.

[99] Yang, P., Rizvi, A.H., Messer, B., Chmelka, B.F., Whitesides, G.M., Stucky, G.D. *Advanced Materials* **2001**, *13*, 427–431.

[100] Kim, E., Xia, Y., Whitesides, G.M. *Nature* **1995**, *376*, 581–584.

[101] Kim, E., Xia, Y., Whitesides, G.M. *Journal of the American Chemical Society* **1996**, *118*, 5722–5731.

[102] Lee, S.-K., Yi, G.-R., Yang, S.-M. *Lab on a Chip - Miniaturisation for Chemistry and Biology* **2006**, *6*, 1171–1177.

[103] Gates, B., Xia, Y. *Applied Physics Letters* **2001**, *78*, 3178–3180.

[104] Park, S.H., Qin, D., Xia, Y. *Advanced Materials* **1998**, *10*, 1028–1032.

[105] Mayers, B.T., Gates, B., Xia, Y. *Advanced Materials* **2000**, *12*, 1629–1632.

[106] Kumacheva, E., Garstecki, P., Wu, H., Whitesides, G.M. *Physical Review Letters* **2003**, *91*, 1283011–1283014.

[107] Yin, Y., Xia, Y. *Journal of the American Chemical Society* **2003**, *125*, 2048–2049.

[108] Velikov, K.P., Christova, C.G., Dullens, R.P.A., Van Blaaderen, A. *Science* **2002**, *296*, 106–109.

[109] Wang, D., Mohwald, H. *Advanced Materials* **2004**, *16*, 244–247.

[110] Kim, M.H., Im, S.H., Park, O.O. *Advanced Materials* **2005**, *17*, 2501–2505.

[111] Deckman, H.W., Dunsmuir, J.H. *Applied Physics Letters* **1982**, *41*, 377–379.

[112] Deckman, H.W., Dunsmuir, J.H. *Journal of Vacuum Science and Technology B: Microelectronics and Nanometer Structures* **1983**, *1*, 1109–1112.

[113] Sharma, V., Yan, Q., Wong, C.C., Carter, W.C., Chiang, Y.-M. *Journal of Colloid and Interface Science* **2009**, *333*, 230–236.

[114] Singh, G., Pillai, S., Arpanaei, A., Kingshott, P. *Advanced Functional Materials* **2011**, *21*, 2556–2563.

[115] Burkert, K., Neumann, T., Wang, J., Jonas, U., Knoll, W., Ottleben, H. *Langmuir* **2007**, *23*, 3478–3484.

[116] Yu, J., Yan, Q., Shen, D. *ACS Applied Materials and Interfaces* **2010**, *2*, 1922–1926.

[117] Wang, L., Wan, Y., Li, Y., Cai, Z., Li, H.-L., Zhao, X.S., Li, Q. *Langmuir* **2009**, *25*, 6753–6759.

[118] Wang, J., Li, Q., Knoll, W., Jonas, U. *Journal of the American Chemical Society* **2006**, *128*, 15606–15607.

[119] Kitaev, V., Ozin, G.A. *Advanced Materials* **2003**, *15*, 75–78.

[120] Zhou, Z., Yan, Q., Li, Q., Zhao, X.S. *Langmuir* **2007**, *23*, 1473–1477.

[121] Wang, J., Ahl, S., Li, Q., Kreiter, M., Neumann, T., Burkert, K., Knoll, W., Jonas, U. *Journal of Materials Chemistry* **2008**, *18*, 981–988.

[122] Leunissen, M.E., Christova, C.G., Hynninen, A.-P., Royall, C.P., Campbell, A.I., Imhof, A., Dijkstra, M., Van Roij, R., Van Blaaderen, A. *Nature* **2005**, *437*, 235–240.

[123] Effenhauser, C.S., Paulus, A., Manz, A., Widmer, H.M. *Analytical Chemistry* **1994**, *66*, 2949–2953.

[124] Oliver, G., Simpson, C., Kerby, M.B., Tripathi, A., Chauhan, A. *Electrophoresis* **2008**, *29*, 1152–1163.

[125] Nagata, H., Tabuchi, M., Hirano, K., Baba, Y. *Electrophoresis* **2005**, *26*, 2247–2253.

[126] Hua, Y., Koshel, B.M., Wirth, M.J. *Analytical Chemistry* **2010**, *82*, 8910–8915.

[127] Masliyah, J. H.; Bhattacharjee, S. *Electrokinetic and Colloid Transport Phenomena*; JohnWiley & Sons, Inc.: Hoboken, New Jersey, 2006.

[128] Landers, J. P. *Handbook of Capillary and Microchip Electrophoresis and Associated Microtechniques*; Taylor and Francis Group, 2008.

[129] Doherty, E.A.S., Meagher, R.J., Albarghouthi, M.N., Barron, A.E. *Electrophoresis* **2003**, *24*, 34–54.

[130] Shapiro, A.L., Vinuela, E., V. Maizel Jr., J. *Biochemical and Biophysical Research Communications* **1967**, *28*, 815–820.

[131] Guo, X.H., Zhao, N.M., Chen, S.H., Teixeira, J. *Biopolymers* **1990**, *29*, 335–346.

[132] Guo, X.-H., Chen, S.-H. *Physical Review Letters* **1990**, *64*, 2579–2582.

[133] Chen, S.-H., Teixeira, J. *Physical Review Letters* **1986**, *57*, 2583–2586.

[134] Wilkins, D.K., Grimshaw, S.B., Receveur, V., Dobson, C.M., Jones, J.A., Smith, L.J. *Biochemistry* **1999**, *38*, 16424–16431.

[135] Ogston, A.G., Preston, B.N., Wells, J.D. *Proceedings of the Royal Society A* **1973**, *333*, 1973.

[136] Ogston, A.G. *Transactions of the Faraday Society* **1958**, *54*, 1754–1757.

[137] Grossman, P.D., Menchen, S., Hershey, D. *Genetic Analysis Techniques and Applications* **1992**, *9*, 9–16.

[138] Guttman, A. *Electrophoresis* **1995**, *16*, 611–616.

[139] Lumpkin, O.J., Dejardin, P., Zimm, B.H. *Biopolymers* **1985**, *24*, 1573–1593.

[140] Otzen, D.E., Sehgal, P., Westh, P. *Journal of Colloid and Interface Science* **2009**, *329*, 273–283.

CHAPTER 2

FABRICATION OF BINARY COLLOIDAL CRYSTALS ON A MICROFLUIDIC CHIP

2.1 Introduction

Binary colloidal crystals (bCC) of submicrometer particles can be fabricated via a spontaneous process called self-assembly.[1-4] These nanoporous structures offer different structural stoichiometries (i.e. LS_x, where L and S stand for large and small, respectively, and x=1[5-7],2[3, 5, 8, 9],3[10],4[5],5[5],6[9, 11, 12],8[5],13[3, 8, 13] based on relative number ratio and size ratio of particles present in the initial colloidal dispersion.[10, 14, 15]) The bCC fabrication methods can be categorized into two major approaches, a layer-by-layer (LbL) growth strategy[10] and a one-stage approach. In a typical LbL method, such as controlled drying[10], stepwise spin-coating[14] and confined convective assembly[15], the crystal is made by layering large and small particles sequentially on top of each other, leading to a 3D nanostructure. However, in a typical one-stage method, such as contact printing[16], self-assembly at an interface[12], horizontal deposition[11], or vertical lifting[17-19], a mixture of dispersed large and small particles is applied, and the self-assembly process simultaneously packs large and small particles into a 3D structure.

Microfluidic approaches to these novel structures include the use of centrifugal forces as per Lee et al.[20], electrocapillary forces in Shiu et al.[21], Zhang et al.[22] and Velev et al.[23] works, continuous sonication in Gates et al.[24], chemically induced factors in Park et al.[25], confinement induced factors in Kumacheva et al.[26] and epitaxial technique in Hoogenboom et al.[27] work. In all of the abovementioned methods, monomodal crystals, made from only one particle size, are fabricated in a microfluidic chip.

Recently the microfluidic colloidal self-assembly (CSA) approach has been used to fabricate monomodal colloidal crystals (mCC) of silica particles for systematic study of dynamics the of DNA and protein separation under electrophoretic conditions[28-32], with the goal of achieving efficient on-chip bioseparation[33-35]. To the best of our knowledge, no microfluidic approach has been employed to fabricate bCCs on a microfluidic chip. Here we investigate the feasibility of making crack-free bCCs of polystyrene and silica particles in a microfluidic channel (100 mm × 20 mm × 14 mm) for the purpose of rapid creation of dense, nanoporous media featuring spatially long range order. The structural stoichiometries attained in this study ranged from LS_2 to LS_6 depending on the particle number ratio.

Nanoporous structures with the above mentioned stoichiometries could not be made using silica particles. To understand this problem, a mathematical model to describe crystal growth during CSA is adapted from Dufresne et al.[36], who studied growth of lattices and emerging cracks in crystals made from silica nanoparticles. According to our optical microscopy observations, this model reproduced crystal growth of polystyrene system, but fell well short of predicting crystal growth of silica particles with qualitatively the same sizes.

Based on the modified Dufresne model[36], analysis of particle-particle interactions and a finite element hydrodynamic simulation of the flow, we ascribe the model deficiency to a hydrodynamically amplified effect of gravity on particle number density in suspension. Based on our findings, particle concentration increases near the microchannel inlet zone, where they are dragged by hydrodynamic viscous forces toward the moving particle compaction front. The Dufresne et al.[36] model was then modified by an exponential term on the dimensionless time parameter, τ, that excellently captured the colloidal crystal growth of the silica system.

The effect of hydrodynamically intensified sedimentation phenomenon was then counterbalanced with stirring generated by periodic chip rotation at specified time intervals, depending on particle sizes. LS_2 bimodal crystals could be made with silica, however a higher number ratio than 2.5 was required in suspension in contrast to their polystyrene counterparts. Furthermore, no evidence of LS_6 structures was observed at a number ratio of 4, as opposed to the polystyrene system.

2.2 Experiment

2.2.1 Materials and Methods

Aqueous suspensions of monodisperse polystyrene particles (750 nm in diameter, 10% v/v, 356 nm in diameter, 10% v/v, 140 nm in diameter 10% v/v and 60nm in diameter, 1.25% v/v) were purchased from Polysciences (Warrington, PA). Colloidal solutions of silica particles (900 nm in diameter, 5% v/v, 540 nm in diameter, 5% v/v, 690 nm in diameter, 5% v/v, 310 nm in diameter, 5% v/v and 150 nm in diameter, 5% v/v) were obtained from Bangs Laboratories (Fishers, IN) and their stock concentrations were taken to be accurate. All colloidal dispersions were used as-received for dilution to the desired concentrations.

Binary colloidal dispersions were made by mixing aliquots of individual monodisperse colloidal solutions with specific volume fractions of particles to get the desired small to large particle number ratios, according to the following relation

$$n = \left(\frac{\varphi_S}{\varphi_L}\right)\left(\frac{d_L}{d_S}\right)^3 \tag{2-1}$$

where n is number ratio, φ and d are, respectively, volume fraction and diameter of particles. Subscripts S and L stand for small and large. Each colloidal dispersion was sonicated in an ultrasound bath (Branson 1200, Triad Scientific, NJ, USA) at room temperature for 30 minutes before use. To prepare bimodal dispersions, each individual colloidal suspension was sonicated separately before and after mixing.

Pre-cleaned glass microscope slides (25 mm × 75 mm × 1 mm) were purchased from Fisherbrand, Canada, and treated with piranha solution, containing concentrated sulfuric acid (98%, Caledon Laboratories Ltd., Canada) and hydrogen peroxide (30%, Fisher Scientific, U.S.A.) (H_2SO_4:H_2O_2 = 3:1 v/v), overnight to oxidize their surface making them more hydrophilic. (WARNING! *The above piranha solution reacts violently with organic materials and generates gas so should not be stored sealed. Handle with caution*).

2.2.2 Microfluidic Chip Fabrication

The microfluidic devices were fabricated by a replica-molding process[37] using poly(dimethylsiloxane), PDMS, (Sylgard 184, Dow Corning, Midland, MI), as is schematically shown in Figure 2-1. The PDMS is prepared via vigorously mixing base elastomer and cross linker at a ratio of 10:1 and degassing for about an hour at room temperature. The liquid prepolymer was then cast against a master (designed in our group[38] with the microfluidic features on its surface, then subsequently cured at 60 ^{o}C overnight. The PDMS chip was then peeled off the master and placed in a clean petri dish. A typical microfluidic chip area was about 1.5 cm × 2.5 cm consisting a micro-channel (20 µm high and 120 µm wide) and a reservoir that was punched through at one end. The PDMS microfluidic chip was then cut at the cross area and rinsed with copious amount of ethanol, to remove organic contaminants, and then with deionized water (Millipore Mili-$\mathrm{Q}_{\mathrm{plus}}^{\mathrm{UV}}$: 18.2 MΩ.cm). Chips were then dried in an ultrapure nitrogen (Praxair, Inc., Canada) flow. A glass microscope slide, treated as described in the previous section, was rinsed with copious amount of deionized water and dried in ultrapure nitrogen flow. The PDMS chip was then placed on this substrate where it binds reversibly to the hydrophilic surface of the glass via van der Waals forces[39]. Lowering the total surface energy, this flexible PDMS chip forms a conformal seal to the reservoirs and micro-channels with the surface of the substrate as shown schematically in Figure 2-2a.

2.2.3 Experimental Setup

A schematic of the micrograph setup is depicted in Figure 2-3. Two 10× microscope lens (Olympus, Japan) were used as eyepiece and objective to focus the incident light into a digital camera (SONY DSC-W330, 14.1MegaPixels) with a 4× zooming capability. Images of the growing colloidal crystal were taken at different time instances and imported into ImgaeJ software[40] for measuring the crystal length, y_c, which are plotted versus time for further analysis.

2.2.4 Crystal and Particles Characterization

2.2.4.1 Scanning electron microscopy

The microscopic quality of the colloidal crystals was investigated using scanning electron microscopy (SEM, JEOL JSM-6010LA and LEO 1430) in secondary electron mode. Before taking SEM images, the PDMS molds were peeled off the glass substrate very carefully, to avoid disturbance to the structures. To shield the silanol and oxygen atoms on the backbone of PDMS molecules at the mold surface from the silica, a 100Å thick layer of gold was sputtered selectively on the microchannel walls of PDMS mold before crystal growth. A plastic tape mask was used to avoid coating the remaining PDMS surface. After successful PDMS mold removal, the crystal on the glass substrate was coated with a thin layer of gold (3-4 nm) via a sputtering system (Branson 1200, Triad Scientific, NJ, USA) before SEM analysis. Images were acquired using an electron accelerating voltage of 10-20 kV.

2.2.4.2 Dynamic light scattering

The particle size and polydispersity of the particles was examined by dynamic light scattering (DLS) measurements, using a Brookhaven BI-200SM Multi-angle instrument.

2.3 Mathematical Model

The mathematical correlation described by Dufresne et al.[36] is derived here. The model was subjected to validation and analysis of crystal growth patterns in our system. As this model will later be subjected to further modifications, the details of the derivation are introduced here.

As water evaporates at the drying edge and hence induces a macroscopic flow of liquid phase, migrating particles will consolidate at the compaction front. If they form ideal closed-packed structures, their spatially averaged volume fraction will be 74%[41]. Beyond the compaction front the particle volume fraction reduces to its initial volume fraction in the dispersion phase. The crystalline region advances smoothly as the flowing fluid brings particles at a specific flux, dependent on the local particle volume fraction[42], and delivers them at the compaction front. The carrying fluid itself flows through the already grown nanoporous lattice, which has a length of y_C . The fluid reaches the drying edge, where it evaporates at a specific rate based on the water concentration gradient and mass transfer coefficient at the local atmospheric conditions. The goal of this model is to estimate the rate the crystal length grows, i.e. $y_C(t)$.

The driving force behind the flow from the reservoir to the compaction front and from there to the evaporation front originates from the high negative pressure exerted by the nano-menisci formed by the fluid between the assembled particles at the drying edge. The other potential driving force would be the hydrostatic head posed by the column of the liquid phase in the reservoir. This head can be estimated by the following equation

$$p_h = \rho g h + p_{atm} \cong p_{atm} \tag{2-2}$$

where ρ is the density of the colloidal dispersion, assumed to be equal to water, 1 g/cm^3, due to the low volume fraction of particles, g is gravitational acceleration, 9.8 m/s^2 and h is height, estimated as 1 mm taking into account the diameter of reservoir, ~3 mm, and volume of colloidal dispersion injected, ~7 µL. The static pressure of the liquid phase can be ignored compared to the atmospheric pressure as the hydrostatic head of the dispersion phase is very small.

For a monodisperse particle system, the radius of curvature of the meniscus, r_M , which is assumed to be a spherical-cap formed between the triangular pattern of assembled particles at the drying front[43], is estimated as 15% of the radius of the particles.[36] The liquid pressure inside can be estimated by[36, 44]

$$p_l = p_C + p_{atm} = -\ {}^{2\gamma}/_{r_M} + p_{atm} \tag{2-3}$$

where γ is the air/water surface tension, 0.07 N/m[45] and p_C is the capillary pressure. The smaller the particles the larger the negative pressure experienced by the flow at the vicinity of the meniscus; i.e. ~370 atm for 50 nm spherical particles. Therefore, a pressure gradient,∇p , will be established from the evaporation front to the compact front, which is y_C long as shown in Figure 2-4, driving the liquid phase through the nanoporous media with a rate calculated by Darcy's law[46]

$$J_p = \frac{k}{\eta} \nabla p \tag{2-4}$$

where J_p is rate of fluid flow through the grown crystal, η is the dynamic viscosity of liquid phase and k is column permeability and can be estimated by the Carmen-Kozeny equation[46]

$$k = \frac{(1-\varphi_c)^3}{45{\varphi_c}^2} r_p^2 \tag{2-5}$$

where φ_c and r_p are the particle volume fraction at the compaction front and the radius of particles, respectively. Different values of φ_c have been reported, ranging from 0.52[43] for a simple packed configuration to 0.74 for ideal face centered cubic (fcc)[11, 47] and hexagonally closed packing (hcp)[48] lattice structures. Values of 0.64 correspond to random hexagonal close packed (rhcp) packing[49, 50]. The actual value is determined by the pace of the self-assembly process; whether or not particles have enough time to transit from disordered to ordered states[51].

Using equations (2-2) and (2-3) the pressure gradient along the grown colloidal crystal length is determined via

$$\nabla p = \frac{p_h - p_l}{y_c} = \frac{2\gamma}{y_c r_M} \tag{2-6}$$

when zero pressure drop is assumed along the non-compacted region of the channel. Substituting this into equation (2-4) yields

$$J_P = \frac{2k\gamma}{\eta y_c r_M} \tag{2-7}$$

According to equation (2-7), particles will be delivered to the compaction front at a fluid flow governed by a balance between viscous resistance and capillary forces[36]. The longer the lattice the more viscous resistance the fluid experiences in migration through the bed and hence the slower the crystal growth due to slower particle delivery flux to the compaction front.

At the evaporation front, water molecules saturate the surrounding air by an interchange process between the surface and the adjacent air. Since air at infinity is not saturated, a concentration gradient is established that induces diffusion from the drying front to a distance where the concentration is considered as ambient, $\rho_{w\infty}$. This evaporating flux can be calculated by Fick's law of diffusion[52]

$$J_{0e} \approx -\frac{D_{w,a}\nabla\rho_w}{\rho_0} \tag{2-8}$$

where J_{0e} is the rate of evaporation, ρ_w is the mass concentration of water molecules, $D_{w,a} = 2.256 \times 10^{-5}\, {}^{m}/_{s}$ is the diffusion coefficient of water molecules in air molecules at ambient temperature, 20 °C and ρ_0 is density of water vapor at ambient temperature[52].

Equation (2-8) gives a rate of evaporation, in $\frac{m^3}{m^2 s}$ unit, of water from a flat surface which is not the case at the evaporation front due to presence of the nano-menisci, which hinder the evaporation rate according to Kelvin's law[36]

$$J_e = J_{0e} e^{-\frac{r_{M0}}{r_M}} \tag{2-9}$$

where r_{M0} is approximately 0.5 nm for water at room temperature[36] and J_e is the evaporation rate at the drying front.

The overall colloidal sell-assembly process and hence the lattice growth is governed by two transport processes; namely evaporation at the drying front and transport of liquid phase through the nanoporous media due to capillary action. Depending on pore size, liquid viscosity, crystal length and ambient conditions either one of these processes can be the dominant factor determining the overall mass leaving the system. To put this into mathematics, the contributions can be expressed as in-series resistances[36, 45]

$$\frac{1}{J_o} = \frac{1}{J_e} + \frac{1}{J_p} \tag{2-10}$$

with J_o being the overall mass leaving the microfluidic chip. Replacing J_e and J_p by their values from equations (2-7) and (2-9), respectively, gives

$$\frac{1}{J_o} = \frac{1}{J_{0e} e^{-\frac{r_{M0}}{r_M}}} + \frac{\eta y_c r_M}{2k\gamma} = \frac{2k\gamma + \eta y_c r_M J_{0e} e^{-\frac{r_{M0}}{r_M}}}{2k\gamma J_{0e} e^{-\frac{r_{M0}}{r_M}}} \tag{2-11}$$

With further arrangements we obtain

$$\frac{1}{J_o} = \frac{\frac{2k\gamma}{\eta r_M J_{0e}} + y_c e^{-\frac{r_{M0}}{r_M}}}{\frac{2k\gamma}{\eta r_M J_{0e}} J_{0e} e^{-\frac{r_{M0}}{r_M}}} \tag{2-12}$$

Taking equation (2-7) into account, the $\frac{2k\gamma}{\eta r_M J_{0e}}$ term in the above equation has length dimension and is called the characteristic length, y_0, of the compaction region[36, 45]

$$y_0 = \left(\frac{J_p}{J_{0e}}\right) y_c \tag{2-13}$$

Accordingly, with the assumption of no air invasion into the crystal, small values of the $\frac{y_0}{y_c}$ ratio indicate slow migration of flow through the nanoporous medium, which result in a lower evaporation rate at the drying front. Large values of $\frac{y_0}{y_c}$, however, happen when the evaporation rate is the limiting step, as determined by ambient humidity and temperature. Further arrangement of equation (2-12) yields a final expression of the total fluid loss from the microfluidic channel as

$$J_o = \left(\frac{y_0 e^{-\frac{r_{M0}}{r_M}}}{y_0 + y_c e^{-\frac{r_{M0}}{r_M}}} \right) J_{0e} \approx \left(\frac{y_0}{y_0 + y_c} \right) J_{0e} \tag{2-14}$$

Since $\frac{r_{M0}}{r_M} \ll 1$ to < 1 for virtually all the pore sizes studied here, the exponential factor was ignored for the rest of this analysis.

The total fluid loss from the microchannel, J_o, results in loading a specific amount of dispersion from the reservoir into the microchannel to compensate for the loss of the liquid phase. As a consequence, a segment of the compensating dispersion moves a distance $\Delta \mathrm{y_f}$ towards the compaction front from its original location before the evaporative loss. At the same time, the compaction front grows a distance $\Delta \mathrm{y_c}$, directed towards the said fluid segment, due to particle supply brought by the dispersion segment, as depicted in Figure 2-4.

Since these two boundaries, compaction front and dispersion segment, move towards each other, the total displacement from the dispersion segment point of view is $\Delta \mathrm{y_f} + \Delta \mathrm{y_c}$ which is equal to a total dispersion volume of $(\Delta \mathrm{y_f} + \Delta \mathrm{y_c})\mathrm{A_c}$, where $\mathrm{A_c}$ is the microchannel cross-sectional area. The amount of particle content in this fluid segment is $(\Delta \mathrm{y_f} + \Delta \mathrm{y_c})\mathrm{A_c}\varphi_\mathrm{d}$ where φ_d is the particle volume fraction in the dispersion. These particles have been delivered to the compaction area and cause it to grow a distance Δy_c.

Particle mass balance reads

$$(\Delta y_f + \Delta y_c)A_c\varphi_d = \Delta y_c A_c \varphi_c \tag{2-15}$$

Further simplification and arrangement yields a relative dispersion volume to crystal volume of

$$\frac{\Delta y_c}{\Delta y_f} = \frac{\varphi_d}{\varphi_c - \varphi_d} \tag{2-16}$$

Hence, measuring Δy_c and Δy_f by optical microscopy per unit time, and knowing the volume fraction of particles in the sample dispersion the value of φ_c can be determined.

Taking into account the contribution of the overall mass leaving the system to the flow advancement from reservoir to the microchannel, Figure 2-4, we can write

$$J_o = \frac{dy_f}{dt} \tag{2-17}$$

Replacing the J_o and y_f values by equations (2-14) and (2-16), respectively, and arrangement we obtain

$$\int_0^{y_c} \left(\frac{\varphi_c - \varphi_d}{\varphi_d}\right)\left(\frac{1}{J_{0e}} + \frac{y_f}{y_0 J_{0e}}\right)(dy_c) = \int_0^t dt \tag{2-18}$$

Further mathematical manipulation and simplification yields

$$\frac{y_c}{y_0} = \sqrt{1 + 2\left(\frac{\varphi_d}{\varphi_c - \varphi_d}\right)\frac{J_{0e}}{y_0}t} - 1 \tag{2-19}$$

In the above equation, the $\left(\frac{\varphi_c-\varphi_d}{\varphi_d}\right)\frac{y_0}{J_{0e}}$ term has dimensions of time. Hence the above equation can be simplified as

$$\frac{y_c}{y_0} = \sqrt{1+2\tau} - 1 \tag{2-20}$$

Where $\tau = \frac{t}{t_0}$ is time constant and t_0 is characteristic time. During initial stages of the colloidal self-assembly, when $\tau \ll 1$, this equation can be estimated by its Taylor expansion,

$$\frac{y_c}{y_0} \cong \tau - \frac{1}{2}\tau^2 + \frac{1}{2}\tau^3 - \frac{5}{8}\tau^4 + \cdots \tag{2-21}$$

where the terms after the first term can be ignored so that the lattice growth demonstrates a linear growth rate with respect to time at early times

$$\frac{y_c}{y_0} \cong \tau \tag{2-22}$$

However, as time elapses and the bed grows, $\tau \gg 1$, the above expression can no longer be applied, and the growth rate will be proportional to the square root of time, $\sim\sqrt{t}$, as is evident from the original equation. Overall, t_0, is in fact the duration of the evaporation-limited regime.

2.4 Results and Discussion

Microfluidic colloidal crystal growth was initiated via injection of 7 μL of the colloidal dispersion in the reservoir and the microfluidic channel, schematically shown in Figure 2-2b. Particles were packed by evaporation induced self-assembly in the microfluidic channel. The advance of the compaction front was observed via the inherent difference between the indices of refraction of the regions with high volume fraction of packed particles compared to the dispersion regimes which have lower particle volume fraction, as depicted in Figure 2-6. Measured values of the diameters of some of the particles used in this study are plotted in Figure 2-7.

2.4.1.1 System of polystyrene particles

On-chip growth of colloidal crystals of polystyrene particles of different diameters was investigated by the experimental approach described in section 2.2.3. Particles used in this study include 750, 356, 140 and 60 nm in nominal diameter, according to the manufacturer. Particle concentrations were diluted with deionized water (Millipore Mili-$\mathrm{Q}_{\mathrm{plus}}^{\mathrm{UV}}$: 18.2 MΩ.cm) to 1.25% v/v from their original concentrations. The movement of the compaction front as observed by optical microscopy was recorded and plotted.

Figure 2-8 exhibits SEM images of monomodal colloidal crystals of three different sizes. In most cases the lattices were destroyed upon PDMS mold removal, due to the stickiness of particles to PDMS surface. Two different mechanisms are believed to cause this problem[53]. The first mechanism is physisorption, with hydrogen bonding and van der Waals attractions, between the silanol groups on the particle surfaces and the oxygen atoms on the backbone of the PDMS molecule. The second mechanism is a chemisorption process that involves formation of a chemical bond between residual silanol groups on the backbone of the PDMS molecule and the silanol groups on the surfaces of silica particles. The use of Au coating on the PDMS channels eliminated this problem.

The long range hexagonal ordering of the polystyrene particles is evident from the top-down SEM images in Figure 2-8. Defects such as point vacancies, mislocations and misaligned lines can be seen, which are quite common in mCC.[49, 54-56]

During lattice fabrication, growth of both face centered cubic (fcc) and hexagonally close-packed (hcp) morphologies are possible due to the very small difference in their free energies, which is calculated to be less than $10^{-3} k_B T$ per particle[54], where $k_B T$ is thermal energy. In fact, the fcc-like structure has a lower free energy, and hence is more stable, than the hcp alternative[48]. Furthermore, structures with fcc stacking take a very long time to grow (about 10^3 slower[49] representing one disadvantage related to their application. In fact, random close-packed (rhcp) stacking is a consequence of rapidly grown colloidal crystals developing a mixture of hcp and fcc stacking that produces rhcp-planes[57, 58]. Rhcp-planes are even more stable due to higher entropy gained by different colloidal assembly configurations suggested by this pattern of stacking.

Top-down SEM analysis does not provide enough information about the stacking pattern of the bulk crystal, therefore, the origin of defects in lattices studied here remains unknown. However, one of the reasons for the emergence of line-defects is believed[54, 55] to be the presence of stacking faults, inherent in rhcp stacking. Figure 2-9a-c depict hcp and fcc stacking in a layer-by-layer fashion and the contribution of the presence of both hcp and fcc to the emergence of line-defects in an mCC.

The advancement of the compaction front, as observed by optical microscopy, is plotted in Figure 2-10a for different polystyrene particle sizes. No evidence of crack formation or air invasion into the lattice was observed during the course of crystal growth. Growth rates were analyzed according to predictions of section 2.3, as discussed below.

The first impression of the results in Figure 2-10 suggests that lattice growth of polystyrene follows a near-linear trend during initial stages of self-assembly, but as the length of the nanoporous media increases with time, a decreasing trend in the rate of growth is observed. According to Figure 2-10, the onset of the importance of viscous effects (flow through the porous media), hindering crystal growth, is deferred as particle sizes increase, which is in agreement with theoretical considerations of the model; c.f. equation (2-20).

A curve-fit of the results to a power law, $y_c \sim t^a$, shows a decrease in the exponential power from 0.76 for an average pore size of 116 nm to 0.66 for an average pore size of 9.6 nm. For pore sizes comparable to water molecule radii (i.e. ~0.3 nm) the only transport mechanism would be diffusion, which would show an exponential power value of 0.5[36, 44, 59]. Since our experiments gives a large exponent it appears that fluid transport through these nanoporous lattices is governed essentially by the bulk motion of fluid and not diffusion.

Dufresne et al.[36] study of flow and fracture in nanoporous media shows larger exponential growth values of 0.87[36] for 52 ± 6 nm diameter particles compared to the lower value of 0.66 for 62 nm particles in this study. This is probably due to the presence of micron size cracks, which are evident from the bright-field images in their target crystals. In fact, cracks in the structure of a lattice allow for channeling phenomenon, which render the colloidal column less resistant to fluid flow and facilitate a higher crystal growth rate compared to the crack-free structures in this study.

As is evident in Figure 2-10a, the length of mCC grown after the same amount of time tends to decrease as particle size shrinks. Crystal of different particle radii grow with different trajectories, that can, however, be described by a global trend via scaling these data with fitted values of y_0 and t_0 from equation (2-20). Figure 2-10b is a plot of scaled experimental data and the excellent correlation made by equation (2-20), shows this mathematical model is a reliable tool for further studies of colloidal crystal growth.

2.4.1.2 System of silica particles

The analysis of crystal growth performed for the polystyrene system was repeated for dispersions of silica particles. Both monodiperse and bidisperse modes were subjected to these growth studies. Particle volume concentrations were the same as the polystyrene systems, 1.25% v/v. For the bimodal studies, monodisperse colloidal solutions with two different particle sizes were mixed together, so that the volume fraction of the larger particles remained the same as in monodisperse studies (c.f. Table 2-1).

In bimodal mode, evaporation induced colloidal self-assembly consolidates larger particles into either fcc or hcp stacking with two commonly formed interstitial spaces between larger particles, depending on the number and arrangement of neighboring particles[16, 60]. There are thus two primary types of interstitial space that can be occupied by the smaller particles in a bimodal structure, so long as the larger particles hcp or fcc lattice is maintained. A tetrahedral space is made if a fourth particle is placed on the upper region of the interstitial space made between three other particles forming a triangle pattern.

However, placement of another three particles above the first three, rotated by 60^o creates an octahedral interstitial space. These interstitial spaces will be occupied by locally available smaller particles in a bimodal structure, making the porous structure less permeable, due to smaller effective pore sizes, than for the monomodal structures.

Table 2-1- Bidisperse colloidal mixtures as used in this study.

Small/Large particle sizes	Size ratio			Small/large Number ratio	Volume fraction of	
	Nominal	SEM	DLS		Larger particles	Smaller particles
150nm/900nm	0.167	0.165	-	4	1.25%	0.024%
100nm/540nm	0.185	0.209	0.256			0.032%
50nm/310nm	0.161	0.177	0.252			0.021%

To avoid disturbing the fcc and hcp structure of the larger particles by the presence of smaller particles, giving rise to major defects, geometrical considerations necessitate size ratios be kept within specific values[8, 11, 16, 61-63]. Consequently, the lower and upper size ratio limits for smaller particles placed in tetrahedral and octahedral spaces without disturbing the larger particle's skeleton are calculated as 0.224 and 0.4142, respectively[60]. According to Table 2-1, selected small to large size ratios, based on size values from the manufacturer and SEM analysis, are well below the upper limits; hence no major defects, caused by space limitations, were expected. However, DLS analysis predicts larger ratios as the particles size are measured a bit larger than their actual sizes due to the presence of the solvation layer around them in the dispersion.

Figure 2-11a shows the growth of mCC for different silica particle sizes. Surprisingly, the growth behavior is quite different than what was observed for the polystyrene system. All silica mCCs studied show distinct increases in *local* growth rates, slope of the local tangent line to the growth diagram, as opposed to their polystyrene counterparts.

A log-log plot of the time required to grow a crystal the whole length of the microchannel, 14 mm, versus particle sizes, is plotted in Figure 2-11b. For the silica system these values could be measured via optical microscopy. However, for the polystyrene system, the growth values had to be calculated based on the mathematical model because the growth times for this system were very long and hard to measure. According to Figure 2-11b, the total time, needed to grow a crystal as long as 14 mm, follows a downward trend with respect to particle size. This trend is seen for the polystyrene system as the porosity of the nanoporous lattice tends to decrease. However, mCCs of the silica system feature faster overall growth than polystyrene of similar particle size. For example an mCC of 310 nm silica takes ~4.3 h to grow, whereas 356 nm polystyrene take ~23.2 h to grow to the same length, even with a larger porosity. The same trend has also been observed for 690 nm silica with ~0.88 h, as opposed to 750 nm polystyrene with a duration of ~6.7 h.

Binary colloidal crystal growth of silica particles showed qualitatively the same trend over time as their monomodal counterpart discussed above, as per Figure 2-12. The growth duration results are plotted in Figure 2-11b, demonstrating modestly longer durations for bimodal dispersions compared to monomodal dispersions, where no smaller particles exist. The trend is consistent with the formation of smaller pore size, which should lead to longer duration growth.

The model of Dufresne et al.[36] cannot describe the growth behavior seen for silica at the volume fraction of the monomodal dispersions used in this study. The discrepant time dependent growth rate behavior could be captured by a modification of the Dufresne et al.[36] model, by introducing an exponential factor to the dimensionless time parameter, τ; namely

$$\frac{y_c}{y_0} = \sqrt{1 + 2\tau^{\upsilon}} - 1 \qquad (2\text{-}23)$$

The experimental data can be empirically modeled with coefficient of determination values fairly close to 1 (i.e R^2 = 0.99) for the particle diameters studied in Figure 2-11a. The values of υ are listed in Table 2-2.

Table 2-2 - Values of υ in the modified Dufresne et al. model, equation (2-23).

system	silica				polystyrene			
d_p [nm]	900	690	540	310	750	356	140	62
υ	2.5			1.4	1			

It is apparent from Table 2-2 that the effect of time constant, τ, is more pronounced with silica, as compared to polystyrene, even for particle diameters that are within the same order of magnitude for the two different materials.

Each particle experiences many interactions originated from van der Waals, electrostatic, stochastic Brownian, depletion, steric, contact, gravitational, buoyancy and hydrodynamic forces in its migration from the microfluidic chip reservoir to the microchannel and further to the compaction front where it is assembled into the structure. Taking into account the conditions of our experiments, of these forces, we conclude only the last two are significant.

- *Gravitational and buoyancy forces*

One of the major physical property differences between the two materials that have not been accounted for in the Dufresne et al. model[36] lies in the specific mass densities, i.e. $\rho_{Silica} \approx 2.00$ and $\rho_{PS} \approx 1.05$ according to the manufacturer's catalogue. This fact incurs higher downward terminal velocities for silica than polystyrene particles in the supply reservoir before they are dragged by flow into the microchannel. A combination of gravitational and buoyant forces acting on individual particles in the reservoir can be expressed as[64]

$$\boldsymbol{F}_G = \frac{4\pi}{3}\left(\rho_p - \rho_f\right) r_p^3 \boldsymbol{g} \tag{2-24}$$

where, ρ_p and ρ_f are mass densities of a particle and surrounding medium, respectively, and $\boldsymbol{g}$ is the gravitational acceleration force vector. Figure 2-13 shows the estimates of calculated force values acting on individual particles used in this study according to equation (2-24), based on the sizes and densities. Silica particles of sizes 690 nm and 310 nm experience almost an order of magnitude larger force compared to 750 nm and 356 nm polystyrene particles, respectively.

Since $\rho_p > \rho_f$, the sign of these forces are the same as the gravity acceleration force vector, resulting in higher particle downward acceleration than polystyrene particles, commonly known as sedimentation.

To better investigate the effect of particle density on crystal growth, a set of experiments on fabrication of bimodal lattices made from two different particle sizes was performed. These particle dispersions are made with silica having the same mass densities, but with three different nominal size ratios, 0.18, 0.32 and 0.76.

For each bimodal size ratio, top-down SEM images of crystals were taken at two different locations from the end of the microchannel, 0.1 mm and 3.5 mm, shown in Figure 2-14a. The crystal morphologies seen at distance 3.5 mm is self-assembled t minutes later than the crystal at 0.1 mm. The top-down SEM images, Figure 2-14b-d, were then analyzed with ImageJ[40] software to enumerate small and large particles to calculate their relative populations versus size ratios, plotted in Figure 2-15.

Apparently there is a gradient in the smaller particle populations, observed at both locations for every particle size ratio. Both particle number gradients approach their initial number densities in the reservoir, which is 4 (80% v/v). The morphology at 0.1 mm shows a volume fraction value closer to the reservoir value than is seen at 3.5 mm, which is formed a few minutes later. Furthermore, as particle size ratios shrink, leading to larger particle weight differences, the particle number gradient is sharper. These results show that gravitational separation is the dominant force in affecting the particle relative number densities. In fact, gravitational force increases the local number density of large particles in the microfluidic chip reservoir before they are fed into the microchannel.

- *Hydrodynamic drag force*

The hydrodynamic drag force exerted by the surrounding flowing fluid on the surface of individual particles migrates them[42, 65] through streamlines from its initial location, upon injection of the dispersion into the reservoir, all the way to the microchannel inlet. In the microchannel particles follow parallel streamlines, which is the inherent property of laminar regimes in creeping flow, until they are delivered at the compaction front, forming close-packed structures.

Streamline trajectories for a case of pure water, or extra dilute dispersion, were simulated in COMSOL Multiphysics 4.3 software (Burlington, MA).[66] The results are plotted in Figure 2-16. This simulation is based on a no-slip boundary condition at the reservoir walls (PDMS and glass substrate), constant pressure at the surface of the dispersion and a constant average maximum velocity at the microchannel inlet, estimated from the initial stages of crystal growth.

Particle trajectories can be qualitatively predicted as they follow streamlines. Here we assume particles undergoing sedimentation do not cause any disturbance to the local flow hydrodynamics[67]. As a consequence of different total fluid velocities at different reservoir locations, plotted in Figure 2-16b, particles experience different magnitudes of drag forces. As is evident from the figure, at regions near the microchannel inlet the larger local velocity values drag particles more intensely than the rest of the reservoir. Based on particle size, densities, and also fluid dynamic viscosity, Stokes terminal velocities[68] of particles are estimated and plotted in Figure 2-17a for both silica and polystyrene systems. It is clear that velocities of particles in the silica system are substantially affected by gravity compared to the polystyrene system, as the polystyrene terminal Stokes velocity values are almost immeasurable when plotted on the same scale as their silica counterparts.

Particles at the upper portions of the reservoir, which is more quiescent, have local velocities comparable to, or even larger than local fluid flow velocity values. Consequently, particles at the upper right gradually migrate and switch their streamlines as they sediment. Since, according to the fluid simulation, local fluid velocity increases on approaching the reservoir bottom near the microchannel inlet, particles reaching these zones may suddenly be grabbed by local flow into the microchannel. Thus, sedimentation can bias the local large particle number density toward higher values compared to smaller particles in the vicinity of the entrance to the microfluidic channel. This bias can indeed be amplified by flow hydrodynamics due to particles faster motions. Hydrodynamic separation amplification has been recently used and studied as a technique by Huh et al.[67]

The observed particle number gradient in the microchannel can also be attributed to the differences in the hydrodynamic drag forces posed on particle surfaces by the flowing medium, based on different particle diameters. However, it is worth noting that hydrodynamic drag force has a linear proportionality to particle size as opposed to the combined gravity-buoyancy forces that show a cubic proportionality as per equation (2-24). Hence, we conclude that the relative particle number density is decreased for smaller particles over time at zones near the bottom of the reservoir, where they are dragged into microchannel for silica system owing to larger than medium mass density values that gets intensified with cubic power of particle size.

Permanent inversion of the microfluidic chip shows bCC crystal growth trends for silica that are quite similar to what is observed for the polystyrene system. Figure 2-17b shows crystal growth trends observed for silica bCCs of different size ratios. Evidently, all of them demonstrate a downward trend for growth rate like the polystyrene system, but finally they stop growing after a specific amount of time. It can be seen that after 200 minutes, the bCCs of silica system have grown less than a millimeter for 150/900 nm and 100/540 nm and less than three millimeter for 50/310 nm. Whereas, in the case of a normally placed microfluidic chip, in which gravity and hydrodynamic drag forces act in the same directions on particles in reservoir, bCCs of the two former samples have grown 14 mm and the latter ~12 mm, according to Figure 2-12.

A close observation of reservoirs of two microfluidic chips placed normally and inversely is depicted in Figure 2-17c. Obviously, the inverted reservoir has developed two separated regions, a clear aqueous and a colloidal dispersion phase. The surface tension of the colloidal dispersion and PDMS surface prohibits motion of the dispersion phase away from the microchannel inlet, thus preventing air bubble leakage into the microchannel.

For an inversely placed chip, the drag and gravity forces act on individual particles in opposite directions; i.e. hydrodynamic viscose drag force, posed by the local mobile aqueous phase, towards the microchannel and gravity away from it. Therefore, it is reasonable to conclude that settling velocities of silica particles outweigh drag force, because otherwise the two clear and dispersion phases would never be separated. Hence, crystal growth ceases after a short time, due to migration of particles away from the microchannel inlet. Figure 2-17d shows a bCC of 150 nm mixed with 900 nm particle. The brown color indicates a binary crystal at the left side and a gradual fading brown color towards right side indicates mCC of 150 nm crystals. Beyond this particle front there is a clear aqueous phase without particle supply. A movie of an inverted chip is available that shows flowing aqueous phase without particle supply, proving that crystal cease growth is not a result of a hydrodynamic equilibrium due to microfluidic chip inversion. Slower Stokes settling velocities for 310 versus 900 nm particles in fact incurs longer growth bCCs of 50/310 nm (< 3 mm) compared to 150/900 nm (< 1 mm).

A direct result of hydrodynamically amplified particle sedimentation phenomenon is seen in bCC fabrication, where an exact ratio of the number density of small to large particles is needed to get the desired nano structure. To counterbalance this effect and restore the small to large particle number ratio to its initial value, upon dispersion injection in a supply reservoir, the reservoir was pipetted on average every 10 min, with the objective of mixing the dispersion content.

This mixing experiment was performed for three bimodal dispersions and colloidal crystal growth was plotted against time as in Figure 2-18a-c. As was expected, crystal growth follows a similar trend as for the polystyrene system, presenting a completely different behavior than that observed in Figure 2-12. Using the modified form of the Dufresne et al.[36] model, the growth rate of bCCs of the silica system can be reproduced within an acceptable error. The error may stem from insufficient stirring via pipetting, based on the size of larger particles. An exponential factor close to one was observed, similar to the polystyrene system, Figure 2-18c, for the mixture of 50 and 310 nm silica particles. In this case the larger particle's tendency to sediment is much less than for the mixture of 150 and 900 nm, Figure 2-18a. Apparently better mixing is needed for larger particles.

2.4.2 On-Chip Deposition of Binary Colloidal Crystal

2.4.2.1 System of polystyrene particles

Deposition of bCCs of polystyrene particles in a microchannel is performed by mixing a specific number density of small and large particles, with a specific size ratio. According to geometrical analysis, for smaller particles settle into tetrahedral and octahedral vacancies in the larger particle assembly without disturbing their structures, a size ratio of not larger than 0.2247 and 0.4142[60] is required, respectively. Otherwise, due to insufficient space available for the smaller particles, a disordered nano porous material will result. Examples are depicted in Figure 2-14c and d, where bimodal lattices of silica particles with size ratios of 0.32 and 0.76 are self-assembled. According to dynamic light scattering results in Figure 2-19, polystyrene particle of 140 and 750 nm nominal diameters with a measured size ratio of 0.180 meet the aforementioned size ratio criteria. Scanning electron analysis also gave a size ratio of 0.183 that still confirms a final ordered structure from the geometrical point of view.

Figure 2-20a shows structural details of the top layer of an LS_2 structure formed with a number ratio of small to larger particles of 2.5. The crystal demonstrates a long range order with only one small particle filling the three-fold interstitial spaces of larger particles assembly. However, there are some small numbers of voids that are not occupied. Apparently presence of small particles has not distorted hexagonal closed packing of larger particles. Similar studies by others show the same bCC structural stoichiometry at number ratios of 2[12], 2.5[11] or 1.8[60]. There is also an evidence of a point defect caused by an imperfectly small 750 nm particle. Furthermore, the SEM analysis reveals particle aggregations distributed at the surface of the LS_2 crystal that are placed in locations other than the spaces between the larger particles. This is probably due to the free space between the surface of the crystal and the PDMS wall that may be a few hundred nanometers long letting nano particles reaching the top of the crystal later than the instant when it is packed.

An increase of number ratio from 2.5 to 9.8 resulted in a bCC with a long range, ordered LS_6 structure, for which on average each individual larger particle is surrounded by six smaller ones, as shown in Figure 2-20b. Other studies have revealed that with smaller number density ratios (i.e. 4[12], 3.9, 4.1[11] or 3.43[69], LS_6 structures can still be achieved at the top layer of the crystal. Analysis of the interstitial space available to smaller particles without disturbing the larger particle assembly, reveals that with the size ratio of 0.2, there is enough space in octahedral and tetrahedral sites for respectively 8 and 1 smaller particles to be arranged[60]. The LS_6 structure is more stable at the surface as opposed to bulk[11], hence the surface configuration might not be replicated in the bulk and there are probably 3D interstitial spaces that have not been fully occupied. However, by increasing the number ratio, more small particles are available to be accommodated in the bulk crystals so that every octahedral and tetrahedral space accommodates appropriate numbers of smaller particles.

According to the top-down SEM image in Figure 2-20b, with a number ratio of 9.8, most interstitial spaces at the surface are occupied by three 140 nm particles, though some of them have been filled by less than three, and in some cases no smaller particles are present.

By increasing the smaller particle number density ratio to 11.0, space restrictions become a determining factor in achieving an ordered structure. In fact, at the compaction front all locally available smaller particles cannot find enough octahedral and tetrahedral sites to arrange themselves in an ordered fashion, creating space limitations for the larger particles. The result is the disordered structure shown Figure 2-21. Clearly the hexagonal close packed orientation of the large particle has been shifted so much that the structure does not feature local short range order. Hence, in addition to keeping the size ratio within a specified range, the number ratio must also be kept within a certain range, in this case $2.5 < n < 11$, to obtain a bimodal crystal with a long rage order.

2.4.2.2 System of silica particles

As shown in section 2.4.1.2, hydrodynamically intensified sedimentation of large particles incurs a lower small particle number ratio. As a result the required number ratio of 2.5 needed for an LS_2 bCCs is not achieved. Therefore, a periodic chip rotator, shown in Figure 2-22a, was designed to invert the microfluidic chip regularly. The colloid suspension is thus repeatedly mixed, based on a pattern determined by a function generator. The apparatus is able to perform timed 180 degree rotations based on a specified-by-user time period. A plot of the chip angular position is depicted in Figure 2-22b for 15 s time intervals.

This equipment can handle six microfluidic chips at the same time. Using this approach, bCCs of silica particles of 100 nm mixed with 540 nm with a number ratio of 4 were fabricated on a microfluidic chip. Particle sizes, as determined by DLS are plotted in Figure 2-23. According to this analysis the small and large particles are larger and smaller than their nominal sizes, respectively. This gives a size ratio of 0.251 that is a bit larger than what is expected to have an ordered binary structure; i.e. 0.225 based on geometrical analysis. However, SEM analysis determined a ratio of 0.209 that guarantees an ordered structure. Here 15 s was chosen as the time interval, being far faster than the 5 min interval used for the pipetted sample, so the rotation should counter the hydrodynamically amplified sedimentation phenomenon. SEM images of a normally packed and a periodically rotated microfluisic chip are shown in Figure 2-24a and b, respectively.

Figure 2-24a shows the binary colloidal crystal fabricated in a nonrotated microfluidic chip produced an almost monomodal crystal, rather than the binary lattice made by use of the chip rotator. This result is consistent with the mathematical and experimental analysis revealing an amplified influence caused by sedimentation of larger silica particle relative to smaller ones.

An interesting point is that with a number ratio of 4, an LS_2 structure was made on the surface of the silica structures, in contrast to the polystyrene system that showed an LS_6 stoichiometry. This result may be due to the chosen time intervals for influencing of sedimentation. In an inverted chip, hydrodynamic viscous drag and gravity vectors point to opposite directions, with viscous drag proved to be the outweighing factor. However, in a normally placed chip these two vectors point to the same direction. This fact, in addition to the complex nature of charged colloidal hydrodynamics makes the reasoning and judgment quit difficult to decide upon appropriate time intervals, whether they need to be equal or not over the course of colloidal self-assembly and so forth.

Hence a more careful analysis and numerical simulation of colloidal hydrodynamics in reservoir during colloidal self-assembly is necessary.

2.5 Conclusions

Dynamic growth of monomodal and bimodal colloidal crystals of polystyrene and silica particles were studied both experimentally via optical microscopy and mathematically by Dufresne et al.[36] model. The model was then modified through an exponential term imposed on the dimensionless time parameter to describe growth of silica lattices, employing a power law to capture the effect of sedimentation phenomena.

Finally, a periodic chip rotator was designed and used to deposit heterogeneous bimodal crystals of silica in a microfluidic channel. The effect of chip rotation in producing bCCs of silica featuring long range, ordered LS_2 structures was discussed. Accordingly, LS_2 structures of silica were fabricated at number ratios higher than those used by others.[11] Numerical simulation of on-chip binary colloidal crystals is needed to better understand the complexities behind colloidal self-assembly phenomena in a microfluidic chip for the production of diverse bCCs with different structural stoichiometries.

Binary colloidal crystals of polystyrene and silica particles were also deposited by a microfluidic approach. Ordered LS_2 and LS_6 and dense disordered structures were obtained for polystyrene system by increasing the small particle number ratio from 2.5 to 11.0.

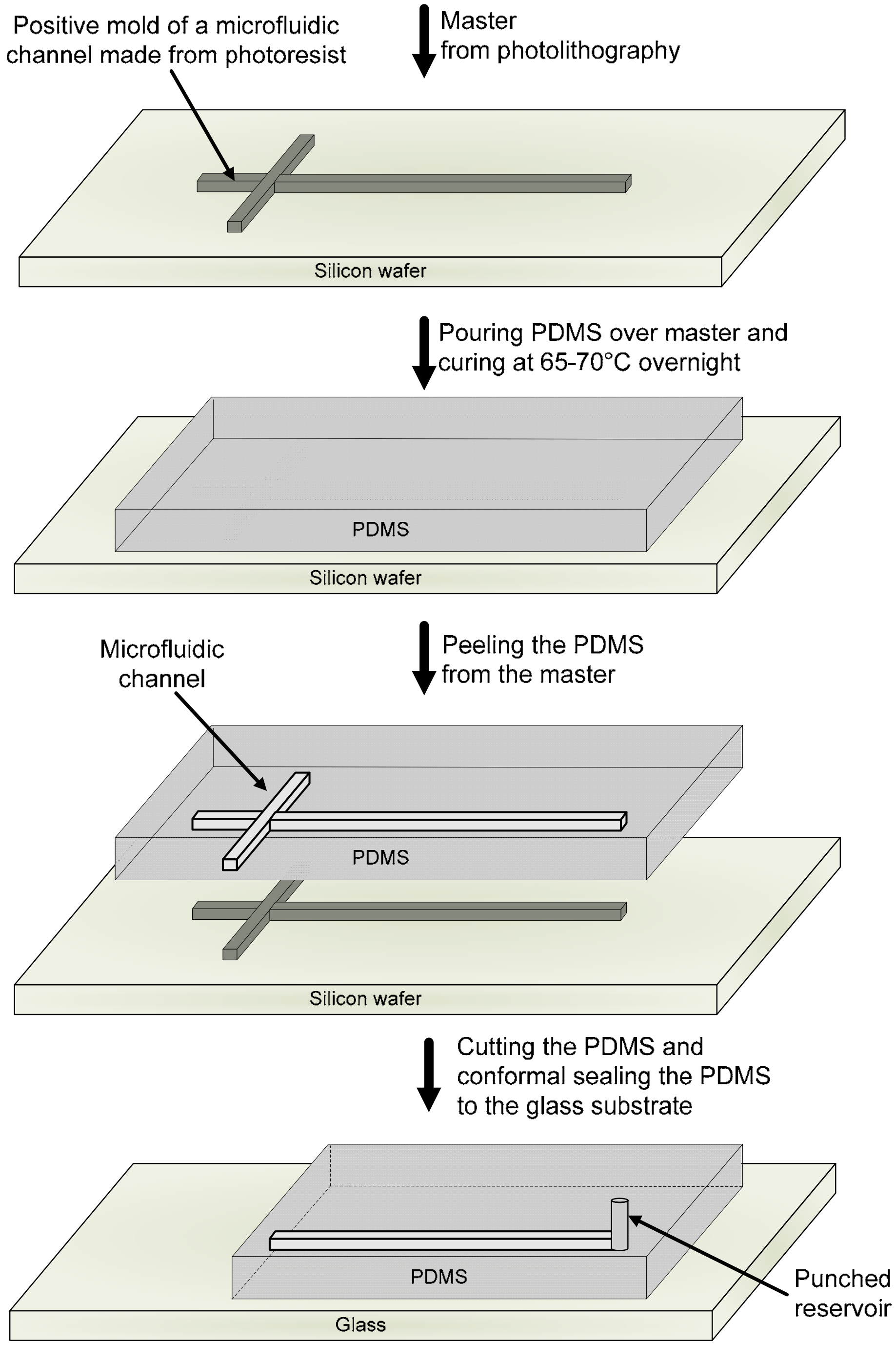

Figure 2-1 Scheme for rapid prototyping of the cross-chip used in this study.

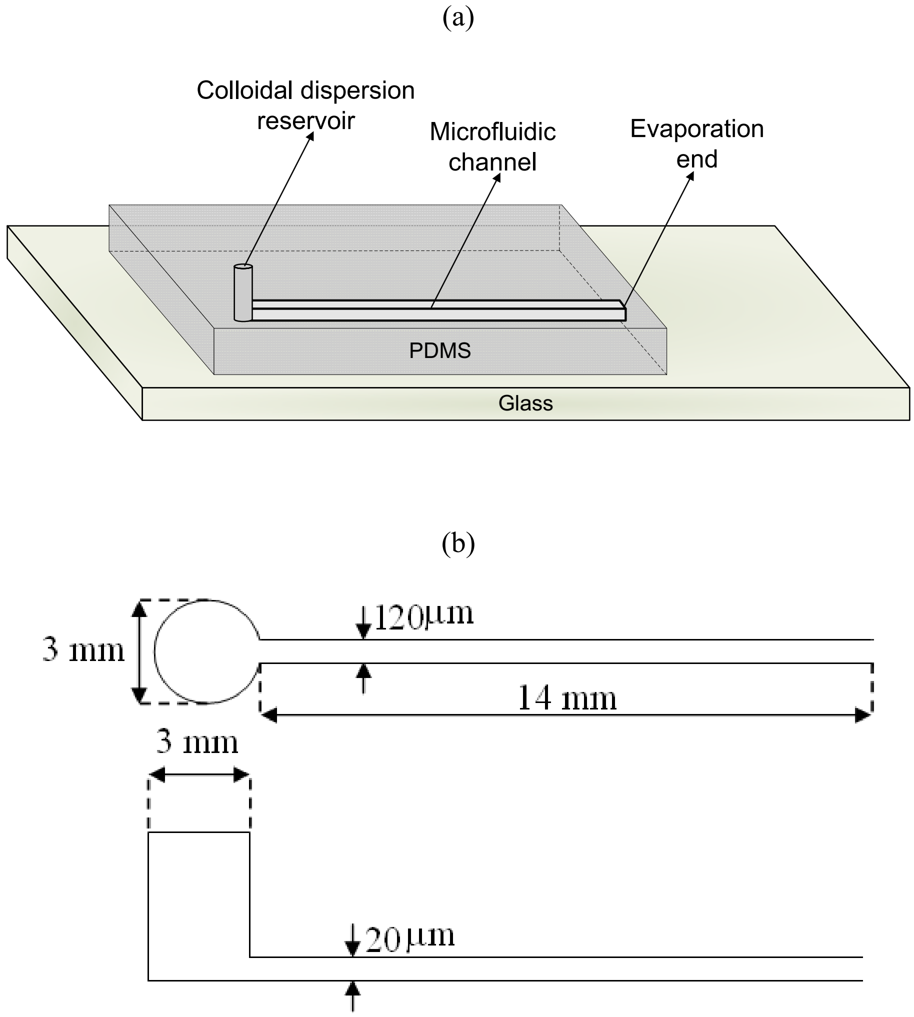

Figure 2-2 The Microfluidic chip used in this study. a) Reservoirs and microchannel arrangements. b) Top and front views with sizes.

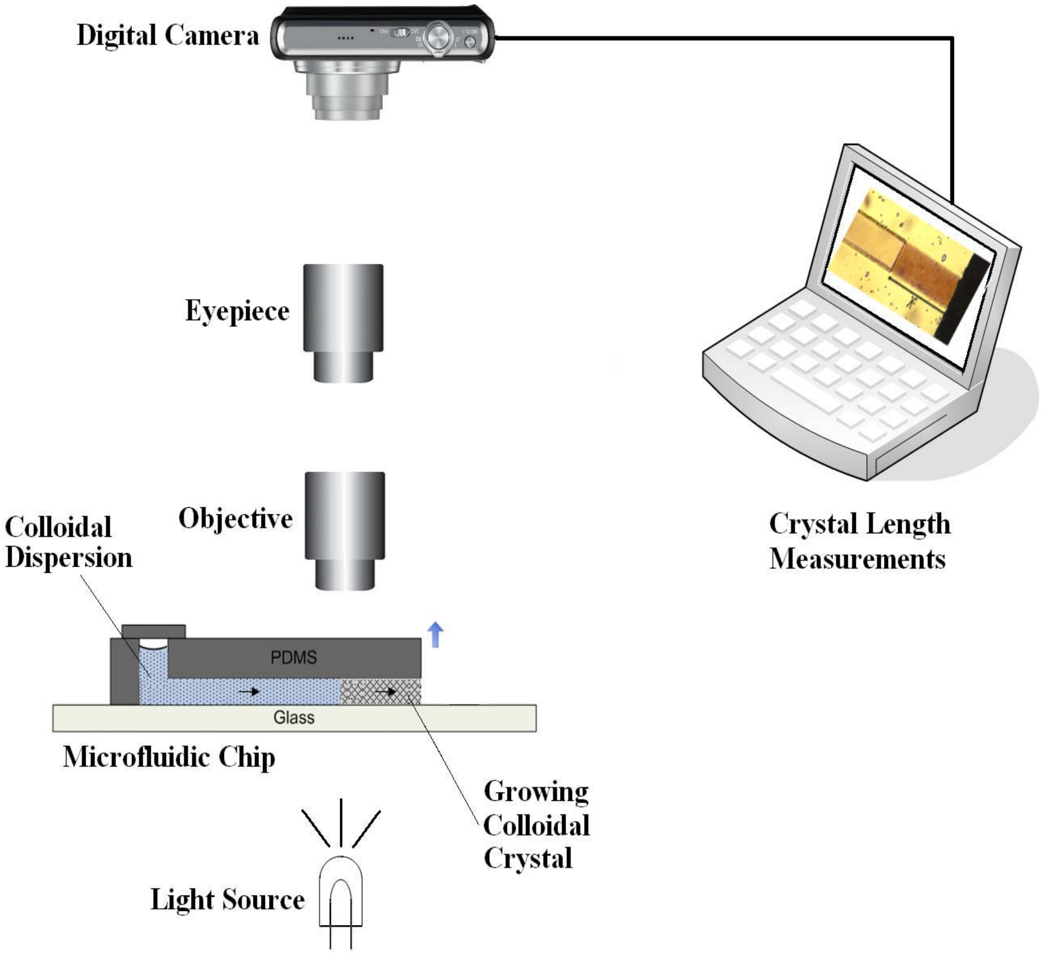

Figure 2-3 Schematic diagram of the setup for dynamic optical microscopy studies of colloidal crystal growth.

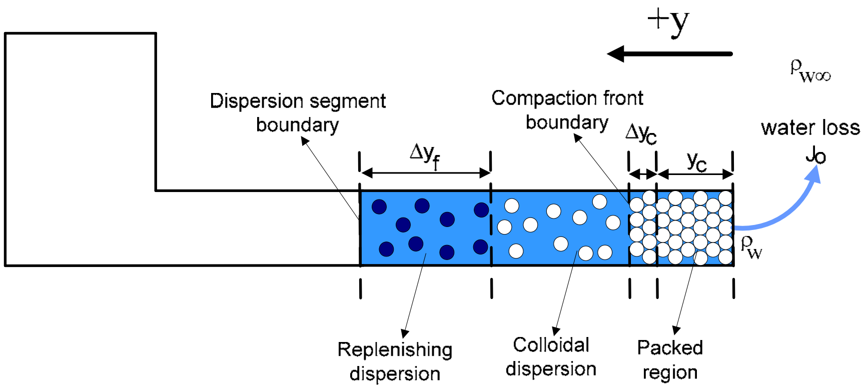

Figure 2-4 Definitions of the compaction front, colloidal dispersion and fluid segment locations relative to each other during colloidal self-assembly. The direction of the y-axis is shown at the top of the figure.

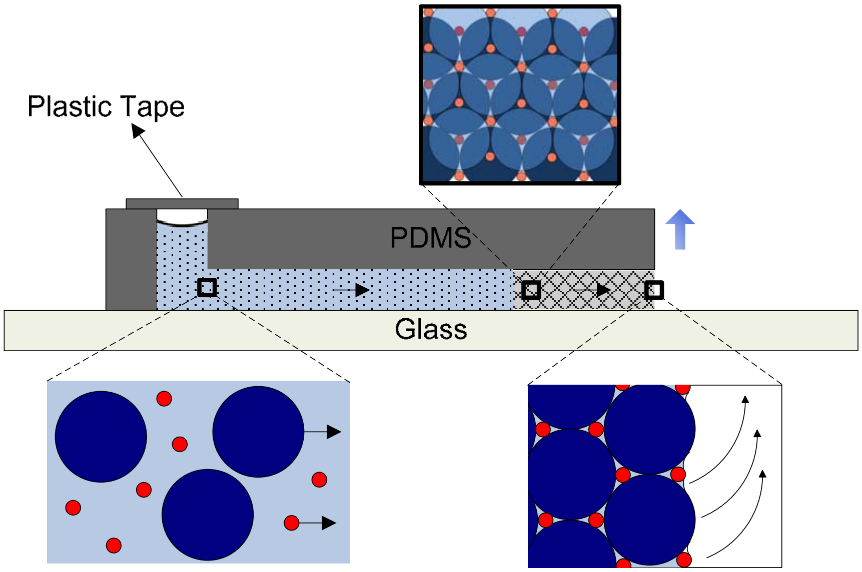

Figure 2-5 On-chip bimodal colloidal crystal self-assembly.

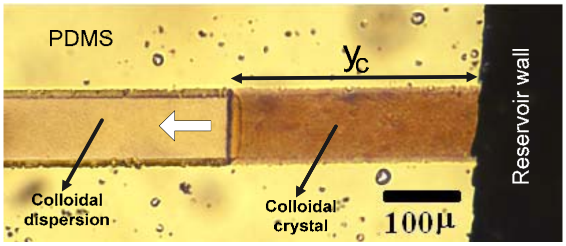

Figure 2-6 Optical micrograph of crystal growth of 690 nm silica particles in microchannel as is evident by the difference in colors of crystal and the dispersion. The arrow shows the direction of the compaction front advancement.

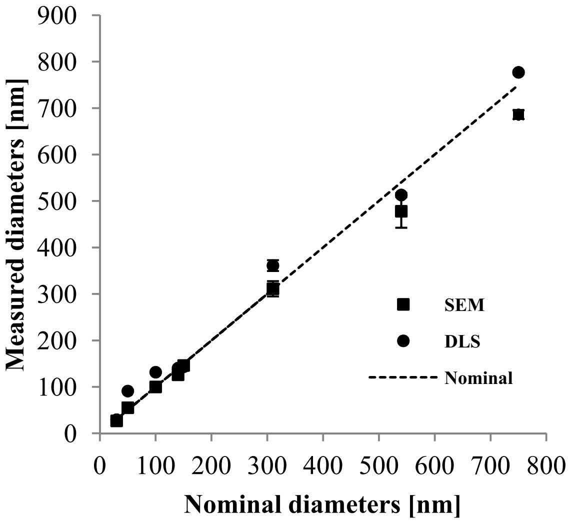

Figure 2-7 Measured values of the diameters of the particles used in this study by DLS and SEM.

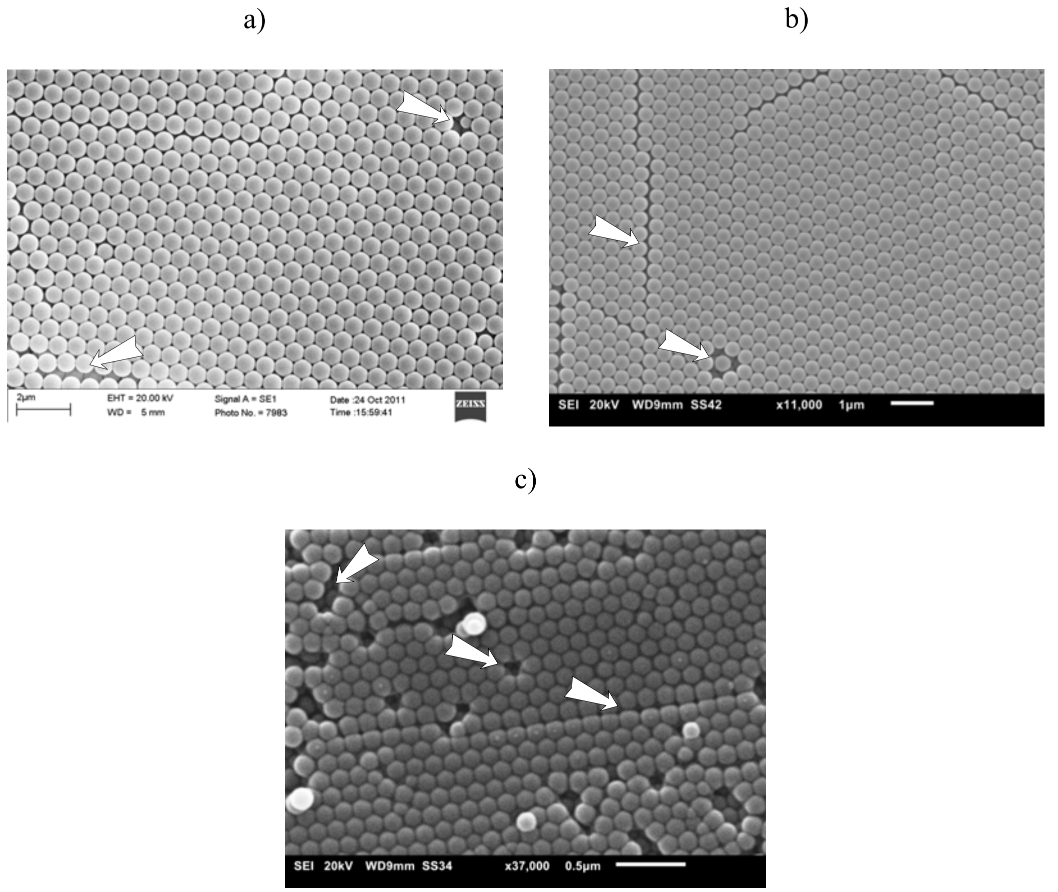

Figure 2-8 Top-down SEM images of self-assembled structures of polystyrene particles a) 750 nm. b) 356 nm. c) 140 nm. Arrows indicate defects.

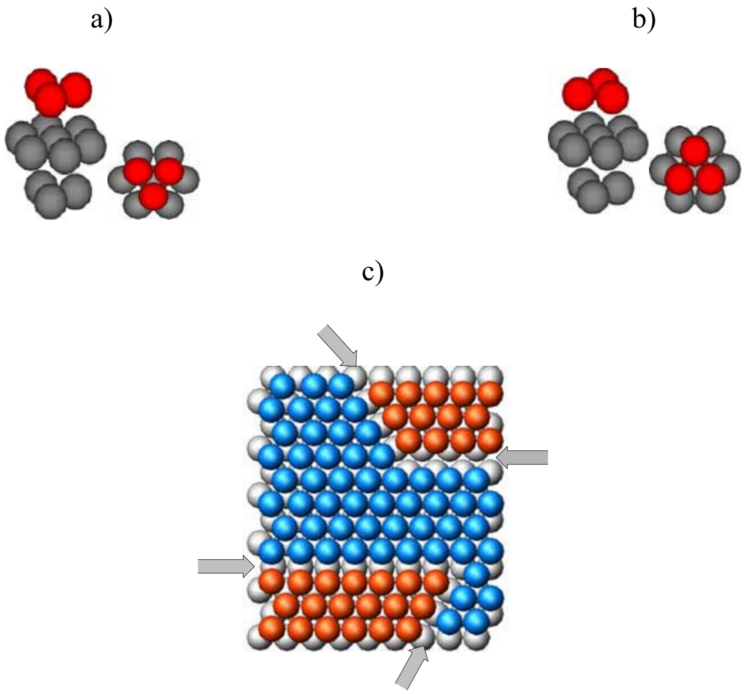

Figure 2-9. Similarities and differences between hcp and fcc stackings. a) hcp stacking and its top view. b) fcc stacking and its top view. c) Presence of both hcp and fcc configuration at the same plane causing line-defects. Arrows indicate defects.

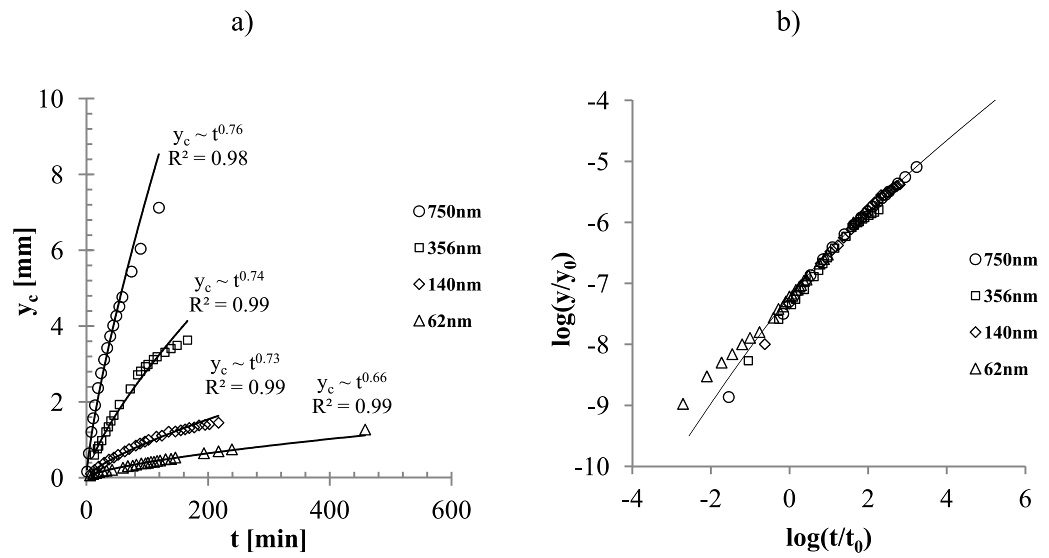

Figure 2-10 Microfluidic mCC growth behavior of polystyrene particles. a) Solid lines are $y \sim t^a$ functions. b) Scaled trajectories of the colloidal mCCs made from monodisperse polystyrene particle with different radii. The line is the correlation made by equation (2-20). In the labels, y_c, y_0 and t are crystal length, characteristic length and time, respectively.

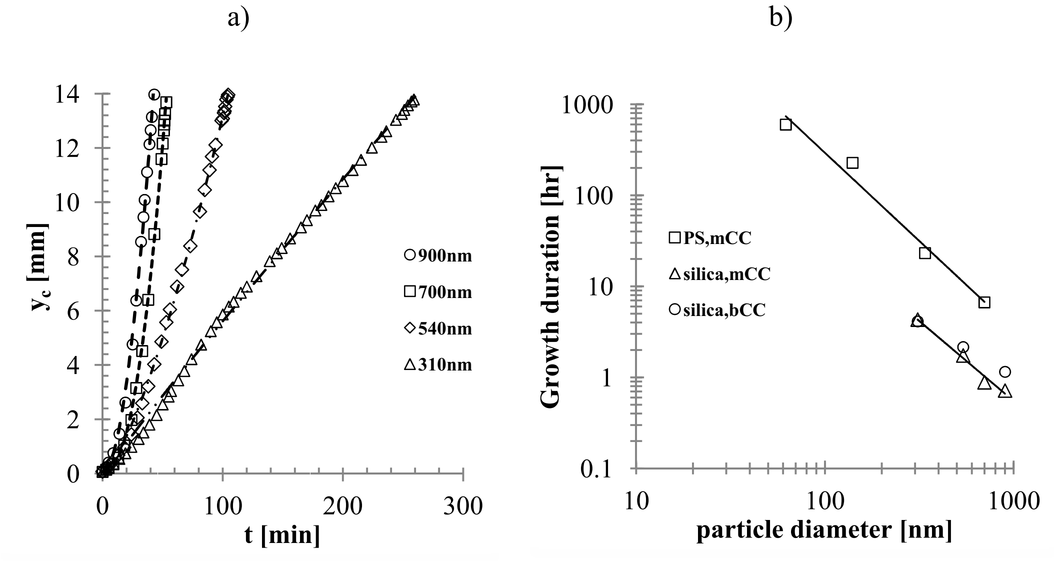

Figure 2-11 Microfluidic mCC growth of silica particles. a) Growth of different crystals of different particle sizes. b) Log-log plot of time to grow a 14 mm crystal for different silica and polystyrene particles at same condition as Figure 2-10a and Figure 2-11a.

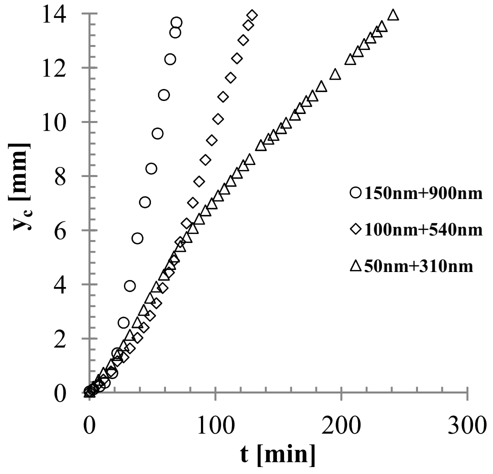

Figure 2-12 Binary colloidal crystal growth of silica particles of different sizes.

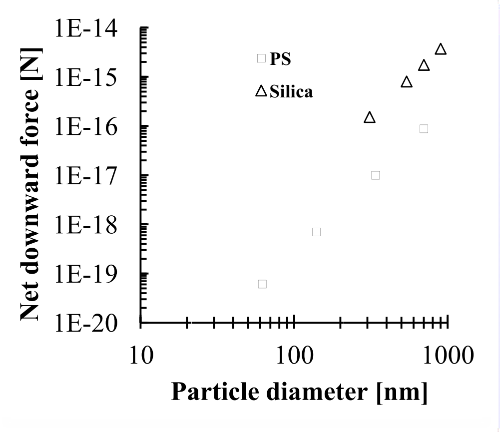

Figure 2-13 Net force imposed on each particle in reservoir through combination of gravity and buoyancy forces.

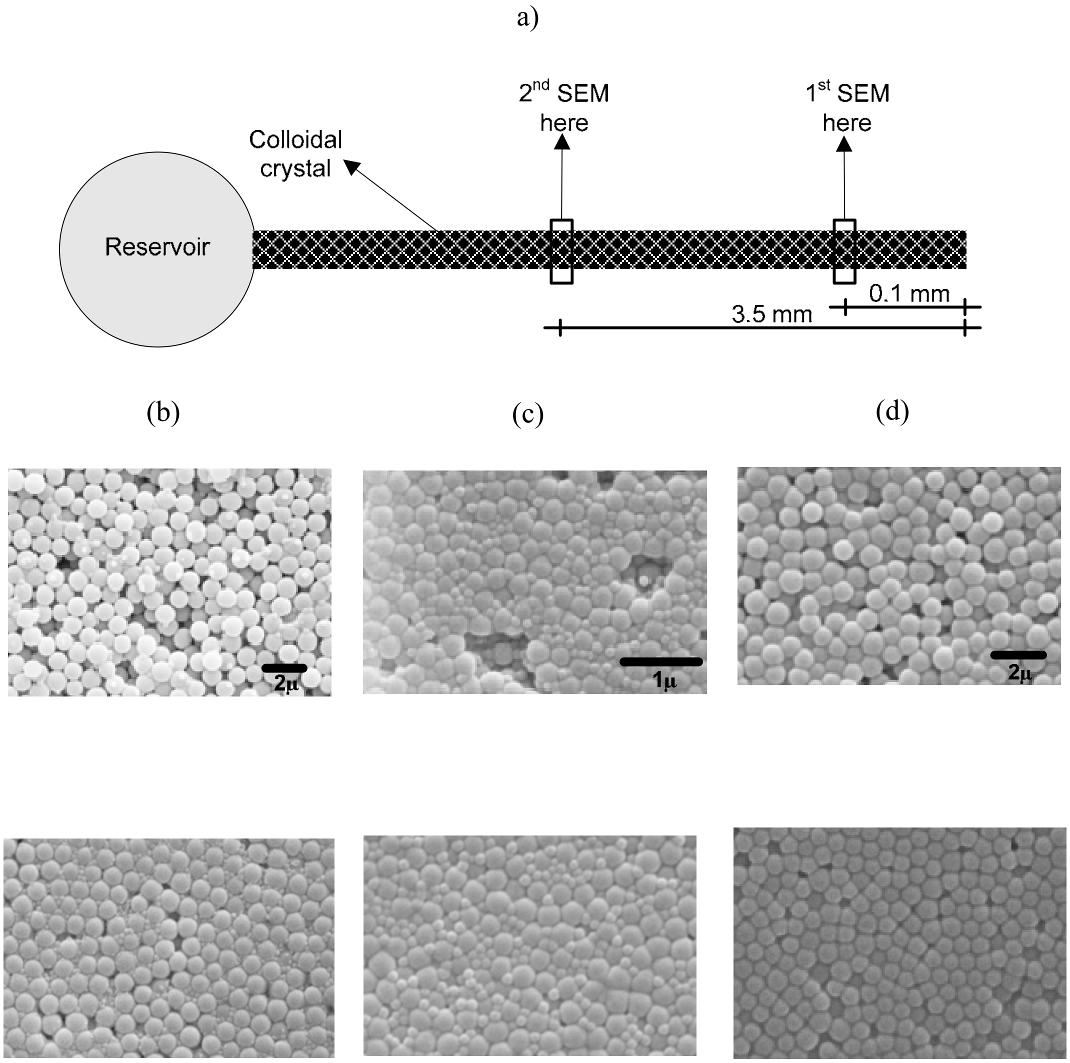

Figure 2-14 Colloidal gradient along the microchannel. a) Schematic of the microfluidic chip and crystal along with two points of SEM analysis. b) bCC of 150/900 nm. c) bCC of 100/310 nm. d) bCC of 690/900 nm. The upper and lower rows demonstrate crystal surface morphologies at 3.5 mm and 0.1 mm respectively.

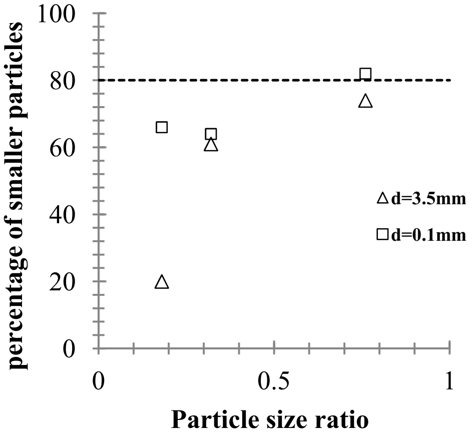

Figure 2-15 Particle number gradient at 0.1 mm and 3.5 mm away from the end of the microchannel.

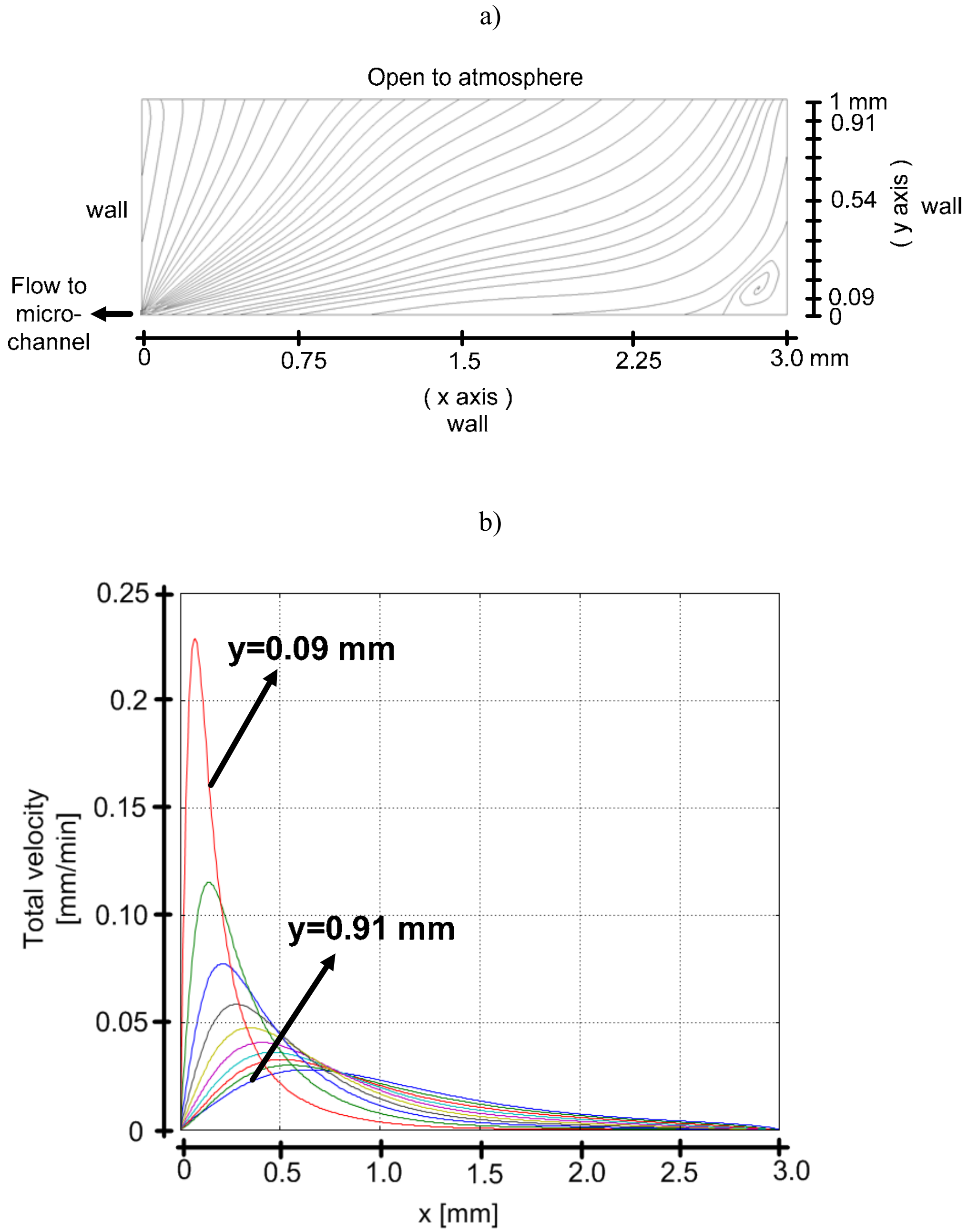

Figure 2-16 Analysis of flow and streamlines in the reservoir with COMSOL Multiphysics. a) Schematic of the microfluidic chip reservoir as implemented in COMSOL representing streamline trajectories of flow. b) Plot of the total flow velocities, i.e. $|\vec{\boldsymbol{u}}| = \sqrt{u_x^2 + u_y^2}$, along the x axis at different y axis values.

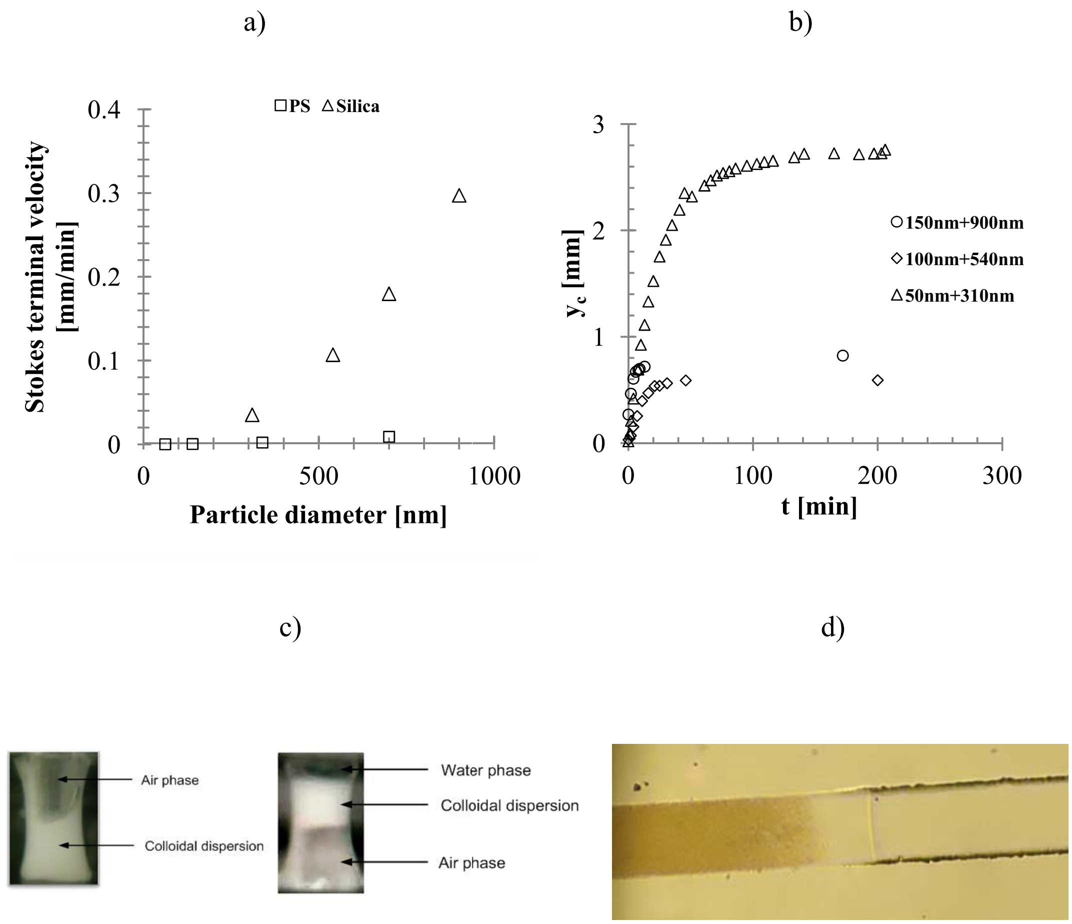

Figure 2-17 Effect of gravity. a) Stokes terminal velocities for particles of different sizes and materials. b) bCC growth trends of silica particles in an inverted microfluidic chip. c) demonstration of gravity effect in the reservoirs of a normally (left) versus inverted (right) chip. d) bCC growth of 150/900 nm in an inverted microfluidic chip, stopped shortly after inversion.

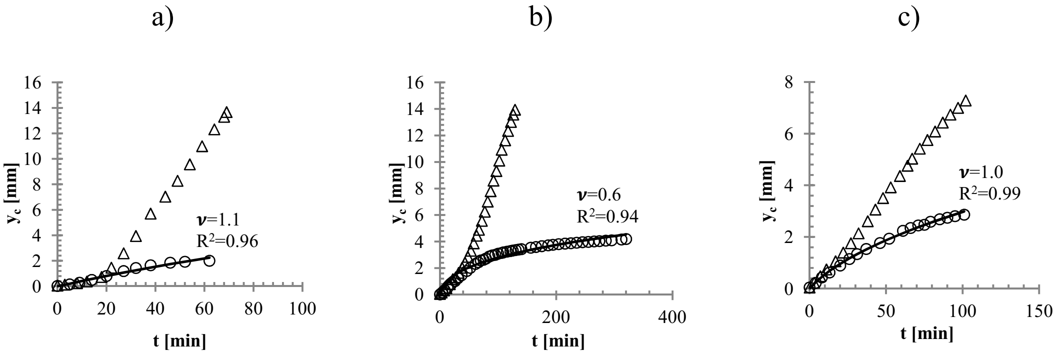

Figure 2-18 bCC growth behavior of silica particles, number ratio=4. Effect of in-reservoir micromixing by a pipette done every 10 min. a) 150/900 nm. b) 100/540 nm. c) 50/310 nm. Triangles and circles indicating bCC's made while the reservoir was not mixed and mixed, respectively.

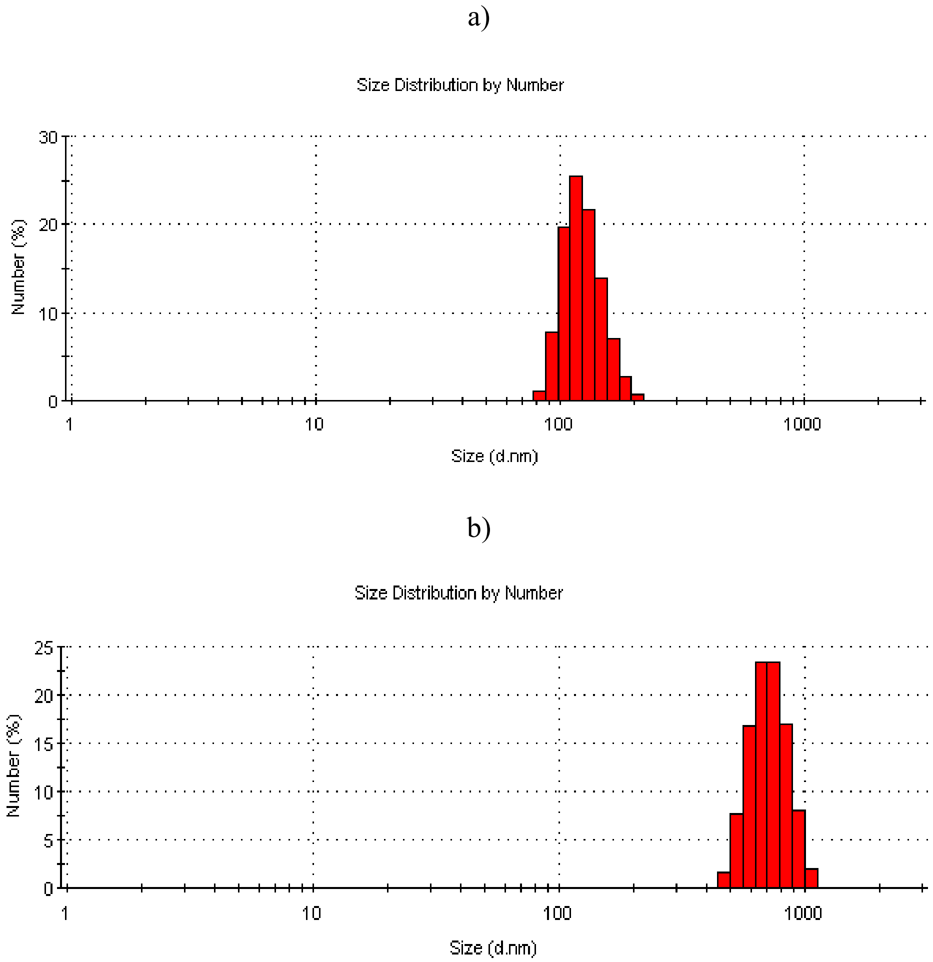

Figure 2-19 Histograms of the polystyrene particle diameters from the DLS. a) 140 nm ($d_p^{av.}$=140.8 ± 12.24% nm). b) 750 nm ($d_p^{av.}$=774.1 nm).

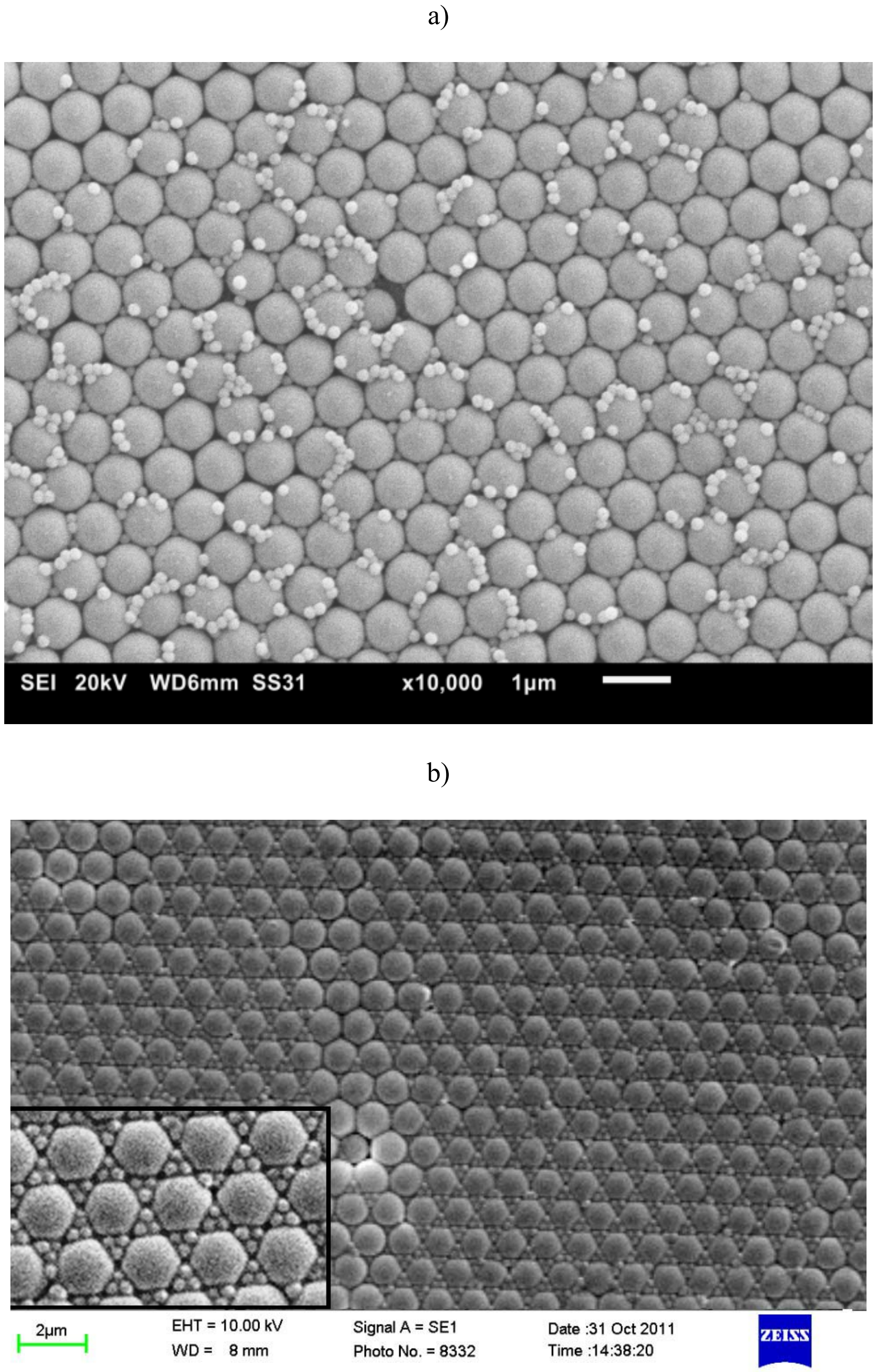

Figure 2-20 Top-down SEM images of ordered bCC of polystyrene particles of 750 nm and 140 nm. a) LS_2 (n=2.5). b) LS_6 (n=9.8).

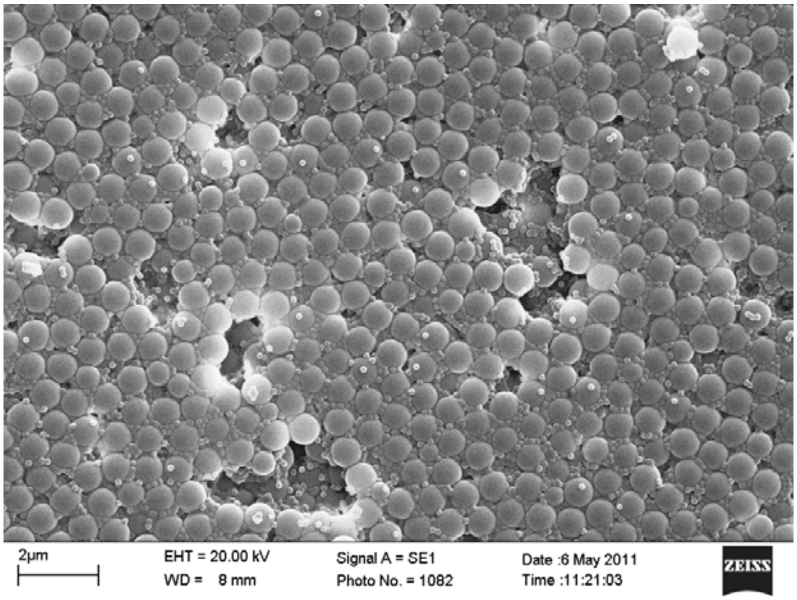

Figure 2-21 Top-down SEM images of ordered bCC of polystyrene particles of 750 nm and 140 nm (n=11.0).

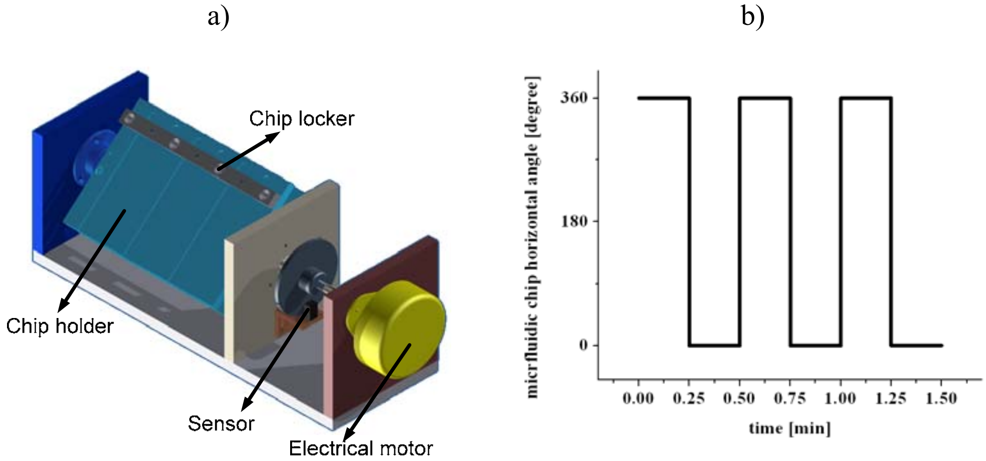

Figure 2-22 Periodic chip rotator. a) Schematic illustrating major composing parts. b) chip angular position as a function of time as performed by the periodic chip rotator; time interval between each inversion is 15 s.

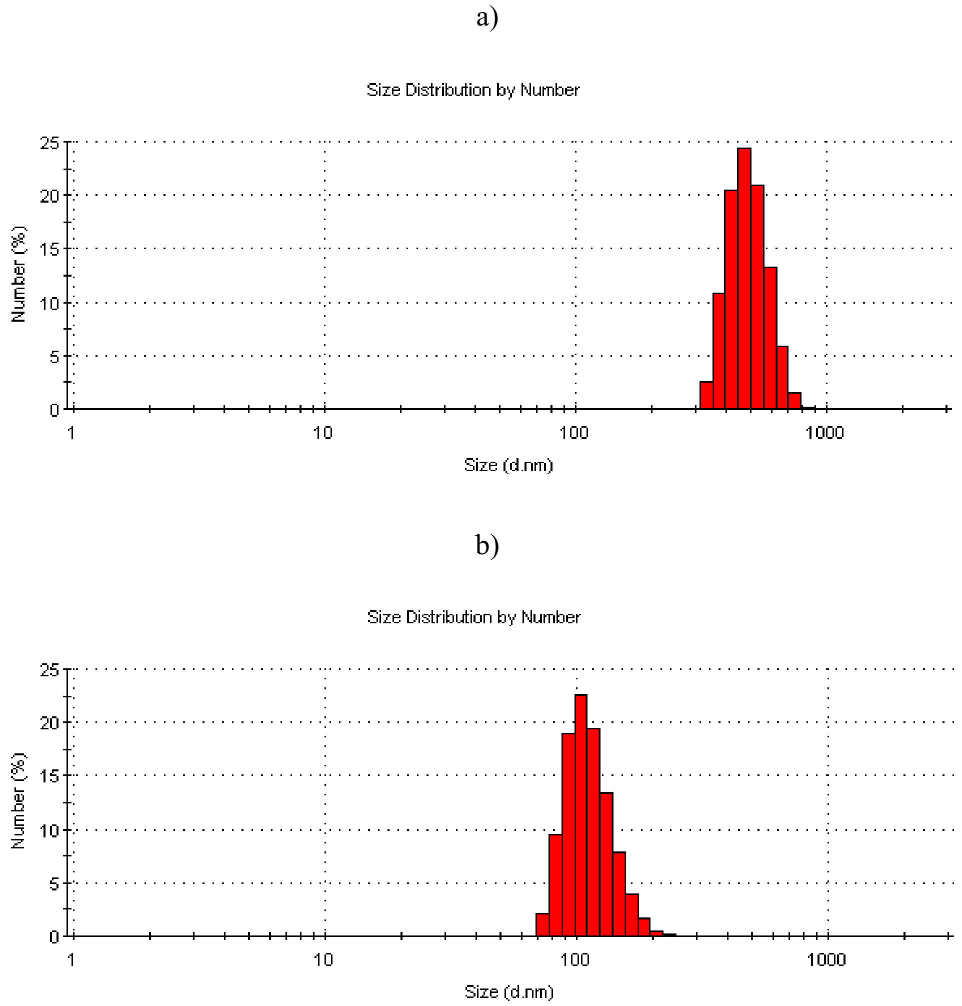

Figure 2-23 Histograms of the silica particle diameters from the DLS. a) 540 nm ($d_p^{av.}$=523.2 ± 15.5% nm). b) 100 nm ($d_p^{av.}$=131.6 ± 10.78% nm).

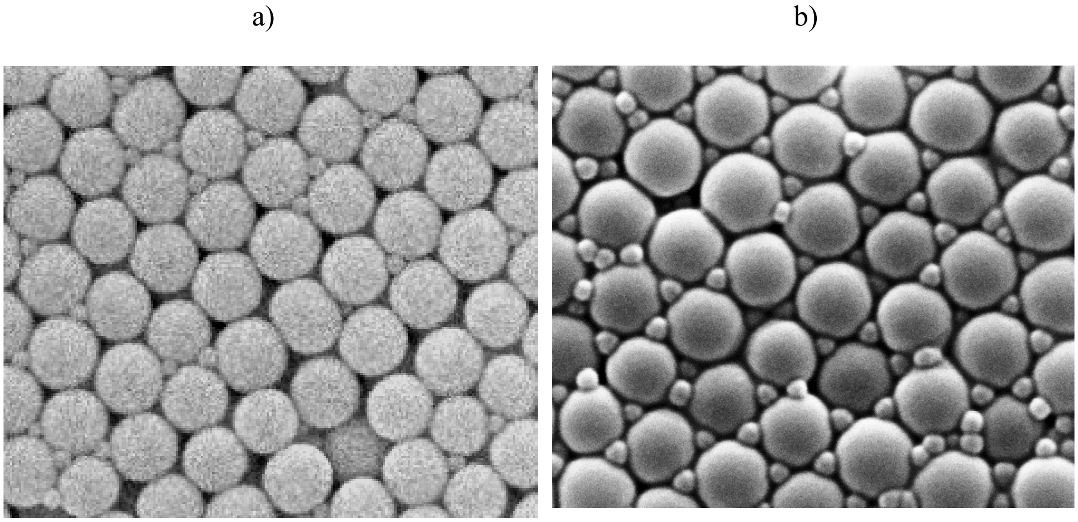

Figure 2-24 Top-down SEM images of ordered bCC of silica particles of 540 nm and 100 nm (n=4). a) Nonrotated chip. b) Rotated chip.

2.6 References

[1] Kiely, C.J., Fink, J., Brust, M., Bethell, D., Schiffrin, D.J. *Nature* **1998**, *396*, 444–446.

[2] Hachisu, S., Yoshimura, S. *Nature* **1980**, *283*, 188–189.

[3] Bartlett, P., Ottewill, R.H., Pusey, P.N. *Physical Review Letters* **1992**, *68*, 3801–3804.

[4] Eldridge, M.D., Madden, P.A., Frenkel, D. *Nature* **1993**, *365*, 35–XI.

[5] Huang, X., Zhou, J., Fu, M., Li, B., Wang, Y., Zhao, Q., Yang, Z., Xie, Q., Li, L. *Langmuir* **2007**, *23*, 8695–8698.

[6] Hunt, N., Jardine, R., Bartlett, P. *Physical Review E - Statistical Physics, Plasmas, Fluids, and Related Interdisciplinary Topics* **2000**, *62*, 900–913.

[7] Schofield, A.B. *Physical Review E - Statistical, Nonlinear, and Soft Matter Physics* **2001**, *64*, 051403/1–051403/4.

[8] Bartlett, P., Ottewill, R.H., Pusey, P.N. *The Journal of Chemical Physics* **1990**, *93*, 1299–1312.

[9] Sharma, V., Yan, Q., Wong, C.C., Carter, W.C., Chiang, Y.-M. *Journal of Colloid and Interface Science* **2009**, *333*, 230–236.

[10] Velikov, K.P., Christova, C.G., Dullens, R.P.A., Van Blaaderen, A. *Science* **2002**, *296*, 106–109.

[11] Wang, L., Wan, Y., Li, Y., Cai, Z., Li, H.-L., Zhao, X.S., Li, Q. *Langmuir* **2009**, *25*, 6753–6759.

[12] Yu, J., Yan, Q., Shen, D. *ACS Applied Materials and Interfaces* **2010**, *2*, 1922–1926.

[13] Schofield, A.B., Pusey, P.N., Radcliffe, P. *Physical Review E - Statistical, Nonlinear, and Soft Matter Physics* **2005**, *72*.

[14] Wang, D., Mohwald, H. *Advanced Materials* **2004**, *16*, 244–247.

[15] Kim, M.H., Im, S.H., Park, O.O. *Advanced Materials* **2005**, *17*, 2501–2505.

[16] Burkert, K., Neumann, T., Wang, J., Jonas, U., Knoll, W., Ottleben, H. *Langmuir* **2007**, *23*, 3478–3484.

[17] Kitaev, V., Ozin, G.A. *Advanced Materials* **2003**, *15*, 75–78.

[18] Cong, H., Cao, W. *Journal of Physical Chemistry B* **2005**, *109*, 1695–1698.

[19] Gu, Z.-Z., Uetsuka, H., Takahashi, K., Nakajima, R., Onishi, H., Fujishima, A., Sato, O. *Angewandte Chemie - International Edition* **2003**, *42*, 894–897.

[20] Lee, S.-K., Yi, G.-R., Yang, S.-M. *Lab on a Chip - Miniaturisation for Chemistry and Biology* **2006**, *6*, 1171–1177.

[21] Shiu, J.-Y., Kuo, C.-W., Chen, P. *Journal of the American Chemical Society* **2004**, *126*, 8096–8097.

[22] Zhang, K.-Q., Liu, X.Y. *Journal of Chemical Physics* **2009**, *130*.

[23] Velev, O.D., Bhatt, K.H. *Soft Matter* **2006**, *2*, 738–750.

[24] Gates, B., Lu, Y., Li, Z.Y., Xia, Y. *Applied Physics A: Materials Science and Processing* **2003**, *76*, 509–513.

[25] Park, J.I., Nie, Z., Kumachev, A., Abdelrahman, A.I., Binks, B.P., Stone, H.A., Kumacheva, E. *Angewandte Chemie - International Edition* **2009**, *48*, 5300–5304.

[26] Kumacheva, E., Garstecki, P., Wu, H., Whitesides, G.M. *Physical Review Letters* **2003**, *91*, 1283011–1283014.

[27] Hoogenboom, J.P., Van Langen-Suurling, A.K., Romijn, J., Van Blaaderen, A. *Physical Review E - Statistical, Nonlinear, and Soft Matter Physics* **2004**, *69*, 051602–1–051602–18.

[28] Zeng, Y., He, M., Harrison, D.J. *Angewandte Chemie - International Edition* **2008**, *47*, 6388–6391.

[29] Zeng, Y., Harrison, D.J. *Electrophoresis* **2006**, *27*, 3747–3752.

[30] Nazemifard, N., Wang, L., Ye, W., Bhattacharjee, S., Masliyah, J.H., Harrison, D.J. *Lab on a Chip - Miniaturisation for Chemistry and Biology* **2012**, *12*, 146–152.

[31] Nazemifard, N., Bhattacharjee, S., Masliyah, J.H., Jed Harrison, D. *Angewandte Chemie - International Edition* **2010**, *49*, 3326–3329.

[32] Shiu, J.-Y., Whang, W.-T., Chen, P. *Journal of Chromatography A* **2008**, *1206*, 72–76.

[33] Zhang, Z., Ratnayaka, S.N., Wirth, M.J. *Journal of Chromatography A* **2011**, *1218*, 7196–7202.

[34] Wei, B., Malkin, D.S., Wirth, M.J. *Analytical Chemistry* **2010**, *82*, 10216–10221.

[35] Zheng, S., Ross, E., Legg, M.A., Wirth, M.J. *Journal of the American Chemical Society* **2006**, *128*, 9016–9017.

[36] Dufresne, E.R., Corwin, E.I., Greenblatt, N.A., Ashmore, J., Wang, D.Y., Dinsmore, A.D., Cheng, J.X., Xie, X.S., Hutchinson, J.W., Weitz, D.A. *Physical Review Letters* **2003**, *91*, 224501/1–224501/4.

[37] Xia, Y., Whitesides, G.M. *Angewandte Chemie - International Edition* **1998**, *37*, 550–575.

[38] Zeng, Y., Harrison, D.J. *Analytical Chemistry* **2007**, *79*, 2289–2295.

[39] McDonald, J.C., Duffy, D.C., Anderson, J.R., Chiu, D.T., Wu, H., Schueller, O.J.A., Whitesides, G.M. *Electrophoresis* **2000**, *21*, 27–40.

[40] ImageJ: Image Processing and Analysis in Java. 2012; http://-rsbweb.nih.gov/ij/.

[41] Xia, Y., Gates, B., Yin, Y., Lu, Y. *Advanced Materials* **2000**, *12*, 693–713.

[42] Dimitrov, A.S., Nagayama, K. *Langmuir* **1996**, *12*, 1303–1311.

[43] Routh, A.F., Russel, W.B. *AIChE Journal* **1998**, *44*, 2088–2098.

[44] Allain, C., Limat, L. *Physical Review Letters* **1995**, *74*, 2981–2984.

[45] Dufresne, E.R., Stark, D.J., Greenblatt, N.A., Cheng, J.X., Hutchinson, J.W., Mahadevan, L., Weitz, D.A. *Langmuir* **2006**, *22*, 7144–7147.

[46] Dullien, F. A. L. *Porous media : fluid transport and pore structure*; 2nd ed.; Academic Press: San Diego, 1992.

[47] Zheng, S., Zhang, H., Ross, E., Thai, V.L., Wirth, M.J. *Analytical Chemistry* **2007**, *79*, 3867–3872.

[48] Woodcock, L.V. *Nature* **1997**, *385*, 141–143.

[49] Gasser, U. *Journal of Physics Condensed Matter* **2009**, *21*.

[50] Prasad, V., Semwogerere, D., Weeks, E.R. *Journal of Physics Condensed Matter* **2007**, *19*.

[51] Cai, Z., Teng, J., Yan, Q., Zhao, X.S. *Colloids and Surfaces A: Physicochemical and Engineering Aspects* **2012**, *402*, 37–44.

[52] Treybal, R. E. *Mass-transfer operations*; 3rd ed.; McGraw-Hill: New York, 1987.

[53] Marinova, K.G., Christova, D., Tcholakova, S., Efremov, E., Denkov, N.D. *Langmuir* **2005**, *21*, 11729–11737.

[54] Meijer, J.-M., De Villeneuve, V.W.A., Petukhov, A.V. *Langmuir* **2007**, *23*, 3554–3560.

[55] Arora, A.K., Tata, B.V.R. *Advances in Colloid and Interface Science* **1998**, *78*, 49–97.

[56] Koh, Y.K., Teh, L.K., Wong, C.C. *Thin Solid Films* **2008**, *516*, 5637–5639.

[57] Pusey, P.N., Van Megen, W. *Nature* **1986**, *320*, 340–342.

[58] Pusey, P.N., Van Megen, W., Bartlett, P., Ackerson, B.J., Rarity, J.G., Underwood, S.M. *Physical Review Letters* **1989**, *63*, 2753–2756.

[59] Komatsu, T.S., Sasa, S.-I. *Japanese Journal of Applied Physics, Part 1: Regular Papers and Short Notes and Review Papers* **1997**, *36*, 391–395.

[60] Wang, J., Ahl, S., Li, Q., Kreiter, M., Neumann, T., Burkert, K., Knoll, W., Jonas, U. *Journal of Materials Chemistry* **2008**, *18*, 981–988.

[61] Wang, J., Li, Q., Knoll, W., Jonas, U. *Journal of the American Chemical Society* **2006**, *128*, 15606–15607.

[62] Vermolen, E.C.M., Kuijk, A., Filion, L.C., Hermes, M., Thijssen, J.H.J., Dijkstra, M., Van Blaaderen, A. *Proceedings of the National Academy of Sciences of the United States of America* **2009**, *106*, 16063–16067.

[63] Bartlett, P., Ottewill, R.H. *The Journal of Chemical Physics* **1992**, *96*, 3306–3318.

[64] Adrian, R. J. *Particle image velocimetry*; Cambridge University Press: New York, 2011.

[65] Kralchevsky, P.A., Denkov, N.D. *Current Opinion in Colloid and Interface Science* **2001**, *6*, 383–401.

[66] COMSOL 4.3. http://www.comsol.com/.

[67] Huh, D., Bahng, J.H., Ling, Y., Wei, H.-H., Kripfgans, O.D., Fowlkes, J.B., Grotberg, J.B., Takayama, S. *Analytical Chemistry* **2007**, *79*, 1369–1376.

[68] Xuan, X., Li, D. *Journal of Micromechanics and Microengineering* **2006**, *16*, 62–69.

[69] Liang, Z., Chiem, N., Ocvirk, G., Tang, T., Fluri, K., Harrison, D.J. *Analytical Chemistry* **1996**, *68*, 1040–1046.

.

CHAPTER 3

EFFECT OF PORE SIZE ON PROTEIN SEPARATION

3.1 Introduction

Three-dimensional colloidal crystals fabricated via a colloidal self assembly (CSA)[1] method provide nanoporous structures that offer a novel approach for the systematic study of the migration of biomolecules, i.e. DNA and proteins, under an external electrical field as a driving force[2-12]. Charged biomolecules can be separated based on their different molecular sizes. The smallest pore size made by CSA on a microfluidic chip has been about 25 nm, fabricated from a monodisperse silica particles of 160 nm, in diameter, in work done by Zeng and Harrison. [12] Based on their studies of proteins, ranging in molecular weight from 20.1 kDa to 116 kDa, Ogston sieving was diagnosed to be the governing separation mechanism in a 1-D, DC external field strength of 30.9 V/cm.

In this study, colloidal crystals with an average pore size ranging from 7 to 48 nm are fabricated on a microfluidic chip having a double-T configuration for the injection and separation stages. [12] Challenges in the fabrication of these crystals include air-invasion and development of micro-cracks. The former problem leads to dry parts of the crystal which are difficult to wet again, leading to spots without any external field. The latter incurs channeling phenomena that hinder the separation quality achieved by the nanocrystal. These problems were addressed and solved by a new approach.

Krypton porosimetry at 87 K was applied to characterize the mesoporous structure of the colloidal crystals fabricated in this study. A convenient sample preparation approach is developed to prepare enough colloidal crystal on a glass substrate for sorption analysis.

Finally, three proteins, trypsin inhibitor (20.1 kDa), ovalbumin (45 kDa) and bovine serum albumin (BSA) (66 kDa), were selected for electrophoretic separation in an external field of 30 V/cm. Electrophoretic mobilities were measured at a variety of pore sizes ranging from 7 to 48 nm.

3.2 Materials and Methods

3.2.1 Reagents and Samples

Aqueous suspensions of monodisperse silica particles (310 nm in diameter, 5% v/v, 150 nm in diameter, 5% v/v) were obtained from Bangs Laboratories (Fishers, IN) and uniform silica beads (100 nm in diameter, 2.8% v/v, 50 nm in diameter, 2.8% v/v) were received from Polysciences (Warrington, PA). Colloidal dispersions of 30 nm silica (1.25% v/v) were purchased from Discovery Scientific (Kelowna, BC). All colloidal dispersions were used as-received. Binary colloidal dispersions were made by mixing aliquots of individual monodisperse colloidal solutions with specific volume fractions of particles to get the desired small to large particle number ratios. Each colloidal dispersion was sonicated in an ultrasound bath (Branson 1200, Triad Scientific, NJ, USA) at room temperature for 30 minutes before use. For bimodal dispersions, each individual colloidal suspension was sonicated separately before and after mixing.

For denatured protein separation experiments, trypsin inhibitor (soybean, 20.1 kDa), ovalbumin (chicken, egg, 45 kDa), bovine serum albumin (BSA) (66 kDa), fluorescein isothiocyanate (FITC), sodium dodecyl sulfate (SDS), 10× TBE buffer solution and mercaptoethanol were purchased from Sigma-Aldrich (St. Louis, MO). These proteins were labeled with FITC, according to the vendor's manual, and their concentrations were about 0.01 mM after labeling. Aliquots of each individual FITC-protein solution were mixed with a 4× TBE solution containing 4% w/v SDS and 8% v/v mercaptoethanol as the reducing and anti-photobleaching agent. The mixtures were heated to 85°C for about 5 minutes in a hot water bath in dark. The protein samples were then diluted with 4× TBE solution containing 0.1% w/v SDS as the running buffer and then mixed together for electrophoresis. Final concentrations of the proteins were 10^{-4} mM.

Pre-cleaned glass microscope slides, 25 mm × 75 mm × 1 mm, were purchased from Fisherbrand, Canada, and treated with piranha solution, containing concentrated sulfuric acid (98%, Caledon Laboratories Ltd., Canada) and hydrogen peroxide (30%, Fisher Scientific, U.S.A.) (H_2SO_4:H_2O_2 = 3:1 v/v), overnight to oxidize their surface making them more hydrophilic. (WARNING! *The above piranha solution reacts violently with organic materials and generates gas so should not be stored sealed. Handle with caution*).

3.2.2 Microchip Fabrication

The fabrication of the PDMS microfluidic chip is discussed in chapter 2. The size of a typical microfluidic chip was about 12 mm × 24 mm × 2.5 mm, embodying two microchannels crossing a third one with a depth of ~20 µm and a width of ~120 µm proved by SEM observations. The two former microchannels, perpendicular to the third one, are offset by about 120 µm. The PDMS microfluidic chip is shown in Figure 3-1.

3.2.3 On-chip Colloidal Crystal Self-Assembly

3.2.3.1 Monomodal colloidal crystals of microparticles

Monomodal colloidal crystals (mCC) of 310 and 150 nm of silica particles were formed via injection of 5-7 µL of the sonicated colloidal dispersion into reservoir 1, shown in Figure 3-1. The dispersion fills all microchannels by capillary action. Soon after that, the same amount of dispersion was injected in reservoirs 2 and 3 and reservoir 4 was left empty. The hydrodynamic head of the colloidal dispersion phase in the supplying reservoirs, 1-3, were kept the same. After a few seconds, evaporation of water from reservoir 4 triggers commencement of colloidal self-assembly, indicated by iridescent color advancing from the end of the microchannel away from reservoir 4. The inlets to reservoirs 1-3 were capped by thin pieces of plastic tape that prevent significant water evaporation that might leave the supplying reservoir dry.

Depending on particle sizes, volume fractions and ambient conditions, on-chip colloidal self-assembly takes a few hours to complete. After completion of CSA and removal of all plastic tapes, colloidal dispersion contents of the supplying reservoirs were replaced with 5-7 µL solutions of 0.1% v/v SDS dissolved in 4× TBE, as the running buffer. The same amount of the solution was also loaded in reservoir 4. The microchip, with the running buffer in all reservoirs capped with thin pieces of plastic tape, was then placed in a petri dish with a small amount of water, keeping the PDMS microchip humidified enough to cease further water evaporation. The microfluidic chip was then used for protein separation by electrophoresis.

3.2.3.2 Monomodal colloidal crystals of nanoparticles

Fabrication of mCCs of 100, 50 and 30 nm diameter silica particles was performed via the same approach as discussed for larger particles. The colloidal dispersion injection sequence was the same, however, after the injection stage, the microfluidic chips were placed in a petri dish with a semi-controlled humidity, as is depicted in Figure 3-2. The humidity was kept higher than ambient (i.e. 28%) by sprinkling water droplets inside the petri dish and restricting mass transfer of water molecules from the container to the surrounding atmosphere through four holes with a diameter of about 3 mm formed on the cap of the petri dish. After CSA completion, the petri dish cap was removed and the colloidal dispersions in the reservoirs were replaced with running buffer. All reservoirs were then again sealed with plastic pieces of tape and a cap without any holes was finally placed on the petri dish, allowing the chip to sit in equilibrium with the buffer solution overnight. The chip was then used for protein separation via electrophoresis.

3.2.3.3 Binary Colloidal Crystal

On-chip fabrication of binary colloidal crystal (bCC) was studied in chapter 2. In this study the same method of fabrication was used. Here, aliquots of colloidal dispersions of silica particles of 150 (5% v/v) and 30 nm (diluted to 0.16% v/v), in diameter, were sonicated separately for 30 min, mixed and sonicated again for another 30 min. The dispersion was injected in the microfluidic chip following the same sequence discussed for mCCs of microparticles. Soon after injection, the chip was placed tightly on the periodic rotator which inverted the chip every 15 s, as shown in Figure 3-3, for a period of 1.5 h. After the bCC packed the whole microchannel, the chip was removed from the chip rotator and was subjected to buffer solution injection, in the manner discussed for mCC of larger particle beds.

3.2.4 Instrumentation and Imaging

FITC-labeled and SDS-denatured proteins were detected using a epifluorescence microscopy apparatus [12]. The labeled proteins were excited with an expanded 488 nm argon ion laser beam. Fluorescent emissions were then collected by a 40× objective and directed, via a mirror, to a 515 nm long-pass filter to select excitation and detection wavelengths. A high-sensitivity CCD camera, interfaced to the objective before the filter, was employed for the collection of images with a rate of 10 fps. Digitized images were then imported in and quantified by the image processing software, ImageJ. [13] An x-y-z translation stage was used to manually move the mounted microfluidic chip to the detection location.

3.2.5 Crystal and Particle Characterization

3.2.5.1 Scanning electron microscopy

The microscopic quality of the colloidal crystals was investigated using scanning electron microscopy (SEM, JEOL JSM-6010LA and LEO 1430) in secondary electron mode. Sample preparation for SEM is described in chapter 2. The same approach was used in this study.

3.2.5.2 Dynamic light scattering

The particle sizes and polydispersities of the particles were examined by dynamic light scattering (DLS) measurements, using a Brookhaven BI-200SM Multi-angle instrument.

3.2.5.3 Pore size analysis

Pore size measurement of the bCC, fabricated in this study, was performed using a Quantachrome Autosorb 1MP instrument where krypton (Praxair, 99.999% pure) gas was chosen as adsorbate. To prepare bCC samples, another microfluidic chip, with different architecture, also designed in our group[7] (c.f. Figure 3-4a), was used. The size of the square chamber, located in the middle of the chip, was 4 mm × 4 mm, with a depth of 20 µm. This chamber was selectively sputtered with a thin layer of gold (Denton vacuum coater) prior to bCC fabrication. Other parts of the chip were masked-off using thin plastic tape, as depicted in Figure 3-4b and c.

Since the internal diameter of the inlet to the sample holder of the Autosorb instrument was about 9 mm, the glass substrate had to be pre-diced prior to bCC fabrication. The substrate was cut with the pattern shown in Figure 3-4d, using a diamond touch dicing saw instrument. The cuts were chosen 0.5 mm deep to facilitate the post cutting stage that should incur any damage to the nanocrystal. The pre-diced substrate was washed following the approach described before. The PDMS chip was then placed on the pre-diced substrate with the middle chamber placed between two parallel lines of cuts as shown in Figure 3-4e.

Binary colloidal dispersions of 150 and 30 nm were prepared following the procedure described in section 3.2.1. The bCC fabrication was initiated by injection of about 30 µL of the dispersion in reservoir 1. After the colloidal dispersion filled the whole microfluidic chip by capillary action, reservoirs 2-5 were also loaded with the same amount of dispersion, keeping the hydrodynamic level the same for all. Reservoirs 1-5 were then capped by thin pieces of plastic tape, prohibiting further water evaporation. Colloidal self-assembly started from reservoir 6, which was left empty, and proceed through 20 microchannels connected to this reservoir to the middle chamber and subsequently to all other parts of the microfluidic chip.

After completion of CSA, the binary colloidal dispersions were removed from the reservoirs and the chip was left undisturbed for a final evaporation process, overnight, where the bCC was completely dried. The PDMS chip was then removed very carefully, to avoid any disturbance to the nanocrystal on the substrate, and the substrate was cut, gently, according to the pre-diced pattern. This process was repeated for 11 other samples to make enough bCC amounts for the krypton adsorption experiment. Figure 3-5 shows part of the predicted glass substrates with the sample bCCs on them.

The samples were then loaded in a 9 mm ID bulb of the equipment for an outgassing process at ambient temperature, overnight, to release any volatile contaminants that might interfere with pore size analysis. The outgassing process was terminated after a less than 0.02 mmHg/min outgas pressure rise criterion was met. Soon after outgassing termination, samples in the sample holder were transferred and sealed to the port, where they were subjected to krypton sorption analysis in an 87 K cooled bath of liquid argon (Praxair).

3.3 Results and Discussion

3.3.1 Colloidal Crystals of Silica Particles

3.3.1.1 Monomodal colloidal crystals of microparticles

SEM images of the crystals of microparticles fabricated in the microfluidic chip via evaporation induced self-assembly are shown in Figure 3-6. Crystals of 310 nm silica particles, in Figure 3-6a, feature common defects including line defects, point defects and point vacancies. One of the origins of point defects is the presence of particles with sizes smaller than the dispersion mean size[14]. However, we expect many of the observed point vacancies arise from particle removal as the PDMS is peeled away for SEM sample preparation.

The particle size polydispersity (PSP) of 310 nm particles are calculated based on the DLS measurements and the following equation[15-17]

$$\mathrm{PSP\%} = \frac{\sigma}{\bar{\mathrm{d}}_{\mathrm{p}}} \times 100 \tag{3-1}$$

where $\bar{\mathrm{d}}_{\mathrm{p}}$ is particle mean diameter and σ is standard deviation.

Mean size and polydispersity values of the particles used in this study as measured by SEM and DLS analyses are listed in Table 3-1 (standard deviation values are calculated at n=3). The particle sizes suggested by SEM are smaller than measured by DLS. This difference can be attributed to the hydrodynamic shell formed around the hydrophilic surface of the particle, in solution[18].

From the SEM analysis, for 310 nm silica particles the polydispersity was calculated to be 6.95 ± 0.51%, which is smaller than the threshold value of 12% beyond which the nucleation barrier increases rapidly[16, 19] and crystallization is believed to be suppressed[16, 20]. A range of 5 to 10%[21, 22] and a value of 10%[23] (specifically for 500 nm colloids) has also been reported that resulted in amorphous structures. A larger polydispersity of 15.75 ± 1.33% is calculated for the 150 nm silica particles used in this study. The SEM of the packing of these particles, in Figure 3-6b, reveals nearest-neighbor hexagonally closed-pack structures sporadically distributed throughout the top-down view, but little long range order is observed, in contrast to the crystal of 310 nm particles. These two particle systems were packed with the same crystallization conditions of ambient temperature, humidity, and particle volume fraction, with a dispersion medium of the same nature. In fact polydispersities, specifically larger than 8%[24-26], are reported to have a detrimental effect on the ordering quality of the colloidal crystals[27-35]. Therefore, the more amorphous structure of the 150 nm particles is most likely due to their more polydisperse nature. The mechanism by which the crystalline structure of the lattice is influenced by polydispersity is complex in nature and depends on detailed size distribution of the particles.[16, 36-38]

In addition to the co-existence of hcp and fcc as a potential contributor to the emergence of stacking faults in this study, discussed in section chapter 2, line defects in the mCC of 310 nm can also be attributed to the polydisperse nature of this colloidal dispersion. This is consistent with the systematic study of the effect of polydispersity on the density of structural defects, in Gates and Xia[14] and also Paquet et al.[38], where the increase of guest particles concentration, with different diameters, leads to greater line defect density in their structures.

Table 3-1 - Diameters of silica particles as measured by SEM and DLS.

Manufacturer	SEM		DLS	
d_p [nm]	$\bar{d}_p$ [nm]	SPD%	$\bar{d}_p$ [nm]	SPD%
310	311.24±16.46	6.95±0.51	361.07±11.78	46.08±2.21
150	145.99±5.37	15.75±1.33	143.20±0.40	13.37±4.07
100	100.00±0.93	7.32±0.41	131.6±0.92	10.78±7.09
50	55.21±4.48	10.48±1.27	91.00±0.42	28.56±2.51
30	26.79±2.58	9.64±0.01	29.43±0.19	17.51±4.97

3.3.1.2 Monomodal colloidal crystals of nanoparticles

Fabrication of crystals of nanoparticles has been attempted before by several authors by different approaches. [35, 39, 40] Here crystals of 100, 50 and 30 nm are fabricated in the microfluidic channels, shown in Figure 3-1, via the approach described in the materials and methods section. Figure 3-7 depicts top-down SEM images of 100, 50 and 30 nm particle beds.

As is expected from the polydispersity value of 100 nm silica particles, i.e. 7.32 ± 0.41%, which is well below the threshold of 12%, the mCC of these particles features long range hexagonal order, apparent in Figure 3-7a. Point vacancies are minor and line defects cannot be distinguished in this image of the surface of the crystal. The middle part of the image, where sample preparation caused removal of a monolayer of particles, shows a second layer of the crystal, proving a highly ordered orientation of the nanoparticles beneath. Nanoparticles in this layer follow the same pattern of particles in the first layer starting at the north side of the removed region, providing evidence of order in other layers in the bulk of the crystal below the surface.

According to Table 3-1, the mean diameter of 50 nm silica particles has been measured as 55.21 ± 4.48 nm with a polydispersity value of 10.48 ± 1.27%.

Accordingly, it is expected that mCC of these nanoparticles do not have a long range structural order. The SEM of the mCC of these particles in Figure 3-7b presents a polydisperse distribution that hinders hexagonal closed-pack orientation. The same packing behavior is also seen for silica nanoparticles of 30 nm diameter, in Figure 3-7c. The polydispersity values of these nanoparticles were measured as 9.64 ± 0.01 according to the SEM analysis.

Figure 3-8 shows the radial distribution function (RDF) calculated based on the image analysis of the top-down SEM images of the nanoporous media. RDF embodies information regarding long range interparticle organization[9, 41-43] and is used as a geometrical characterization of the mCCs of 310, 150, 100, 50 and 30 nm based on their top-down SEM images. The center coordinates of the particles were measured in ImageJ[13] software and used to calculate the RDFs. Furthermore, local structural order of the structures were captured by global orientational order parameter[9], ψ, and are shown for each structure in Figure 3-8.

For an ideal hcp or fcc crystal the RDF features numerous peaks with high magnitudes, as is depicted in Figure 3-8a, hence it can be used as a reference to judge upon the structural order of the nanoporous media made in this study.

Crystals of 310 and 100 nm, especially 310 nm particles, show structural order, based on the magnitude and number of sharp peaks in their RDF plots. However, RDFs of the nanoporous structures of 150, 50 and 30 nm do not have as many peaks as the model reference crystal and also the magnitude of their peaks is quite shallow.

Huang and Pemberton[40] studies of sub-100 nm silica particles showed better structural order for 53 ± 9.5% nm than that fabricated in this study for 50 nm. The polydispersity in their studies was lower, 9.5%, compared to the value of 10.48 ± 1.27% in this study. However, their particles of 38 ± 12.8% nm, showed qualitatively the same structural defect density as in this study for particles of 30 nm, even with a lower volume fraction of the particle. A lower volume fraction favors increased structural order. [40] Hence it can be concluded that polydispersity values higher than 8% reduce the lattice order, as pointed out by Jiang et al. [24]

Two major challenges with the fabrication of mCCs of nanoparticles were the formation of micro-cracks developed during the course of CSA and development of totally air-invaded areas. Cracks could be easily observed via optical microcopy as their sizes are on the order of a few micrometers, and there is a difference between their refractive indexes and the surrounding wet mCC. In addition, air-invaded regions are distinguishable by differences in the Bragg diffraction phenomena in the reflection mode during optical microscopic analysis. Cracks in the body of the nanoporous media serve as preferential pathways for biomolecules during separation. For separation to occur proteins must migrate through the porous network of the lattice, rather than the cracks. The presence of air-invaded spots in the nanoporous lattice hinders the electrical field strength and its consistency along the bed during protein separation. The absence of an external electrical field, incurs inconsistency in the measured mobilities of the analytes. It is very difficult to re-introduce liquid into the dried regions.

As the void area of the growing nanoporous lattice shrinks with smaller particle sizes, the viscous resistance against the transfer of water increases. Hence, at an extreme, water diffusion in the surrounding air at the evaporation edge happens faster than water transfer through the nanocrystal to compensate for the loss-by-evaporation. As a consequence, air starts invading the crystal, causing the surface of the packed silica particles to become completely dried.

Figure 3-9 shows a bright-field image of the colloidal self-assembly of 30 nm silica particles in the main microchannel. As is evident, there are three cracks starting from the channel outlet invading into the microchannel. During the initial stages of CSA, the tips of these cracks follow the compaction front at about 70 µm distant, however at later times, the distance increases to about 250 µm. Cracks follow the compaction front with a different velocity than the compaction front itself at various time instances. Usually, crack length follows a stepwise increasing pattern with respect to time; namely, a crack might not grow for a short period of time, whereas the compaction front travels in a continuous pattern. The same crack growth behavior has been seen in studies of fracture in colloidal dispersion subjected to drying.[44, 45]

The origins of cracks and their growth pattern is still an open subject for research[46]. However, according to recent findings[46-50], water drainage due to capillary action at the drying edge, which keeps the bed wet, tends to shrink the crystal. On the other hand, the lattice is cemented to the glass substrate at one side and to the PDMS chip at three other sides, through chemisorption and physisorption phenomena between the silanol groups[51], as shown schematically in Figure 3-10. As a consequence of this misfit, a dynamically growing internal stress is imposed that will be released, after a threshold value is met, by cracking the crystal apart. This crack propagates when the energy released by its formation exceeds the surface energy. [48, 49]

Figure 3-11 shows three propagating mico-cracks of a 30 nm silica colloidal crystal by optical microscopy in reflection mode. According to this observation, the three cracks and the two microchannel walls are, on average, spaced vertically and equally by about 29.61 ± 1.93 µm throughout the microchannel length whole.

There are also areas where water has evaporated creating air-invaded regions. These regions, that are brighter than other regions in Figure 3-11, can also be observed to grow tangent to the cracks, which confirms cracks to be preferential pathways for water to evaporate faster than other areas.

To prohibit crack formation and growth, the spacing between cracks has to be increased to values greater than the microchannel width; i.e. 120 µm in this study. Based on the mathematical model of Allain and Limat[48], two contributors to the spacing between cracks are the flux of water content and the crystal thickness that is determined by the channel height. Accordingly, at a lower value of water flux, a higher value of spacing is expected. Since the microchannel geometry was fixed, to attain higher value of crack spacing the flux of water was decreased simply by placing the microfluidic chip, with the ongoing CSA, in a humidified environment, as described in section 3.2.3.2. By increasing the surrounding humidity the driving force for mass transport from the evaporation front to the surrounding environment is decreased; hence the flux of water is decreased. Therefore, the crack spacing is increased and no further cracking was seen in optical micrographs of crystals of 30 and 50 nm particles.

Another major advantage of growing crystals of nanoparticles in an environment with higher than ambient humidity is that air-invasion does not occur. In fact by lowering evaporation rate, the CSA rate will be mainly governed by evaporation rate rather than water flow through the nanoporous media, as opposed to the original approach where the later was dominant.

According to the optical microscopic analysis in this study, no evidence of air and crack invasion was found in the mCCs of 100 and 50 nm crystals fabricated in a humidified environment.

3.3.1.3 Binary colloidal crystals of nanoparticles

A binary colloidal dispersion of 150 and 30 nm was dried on the microfluidic chip via the approach discussed in chapter 2. A top-down SEM image of this crystal is shown in Figure 3-13a. No evidence of LS_2 structure is apparent on the surface of the crystal. In the previous chapter it was shown that with a number and size ratio, small to large particles, of, respectively, 4 and 0.2, these structural stoichiometries can in fact be achieved on a microfluidic chip. However, for a mixture of 150 and 30 nm with the same number and size ratios within the same microchannel, the surface morphology of the lattice does not show an ordered binary crystal.

It is not surprising that the structure does not present a long range order taking into account the polydispersity value of 15.75 ± 1.33 for the 150 nm particles, which produce an amorphous structure.

To better analyze the bulk structure, the crystal was grown on a pre-diced glass substrate to facilitate cutting the 1 mm thick glass substrate. The PDMS chip was gently removed and the substrate was cut very gently to minimize any disturbance to the nanostructure. SEM of the cross-sectional area of the same kind of sample as Figure 3-13a, in Figure 3-13b, shows a higher number of 30 nm particles that are, on average, distributed uniformly throughout the structure. The cross sectional area is very disturbed however, as shown the inset of Figure 3-13b, there are still traces of LS_2 structure that can be seen within the skeleton of the larger particles. This observation suggests that LS_2 nanostructures are more thermodynamically stable for the inner layers of the structure than the top most one, when formed by CSA in a PDMS chip.

According to the geometrical calculation, presented in Appendix A, with the assumption of a spherical pore, the smallest pore size achievable by doping 150 nm silica particles with the 30 nm, is 10.88 nm. Krypton porosimetry at 87 K is a sensitive and reliable method to characterize the mesoporous nature of these structures[52], for surface areas as low as 0.05 m^2. Recently it has been applied to measure the surface area and the pore size distribution of mesoporous silica films made by the glancing angle deposition (GLAD) technique in Kruase et al.[53] Based on the sample preparation approach introduced in section 3.2.5.3, a mesoporous structure of the 150 and 30 nm particles was subjected to krypton adsorption. An isotherm of krypton adsorption at 87 K was obtained from a pressure of 10^{-4} to

0.9950 (adsorption cycle) p_o where p_o is the pressure when krypton starts solidifying at 87 K.

Pore size distribution was determined by the Quantachrome software (v1.52, 2006) by analyzing the adsorption isotherm and is plotted in Figure 3-12. Porosimetry studies were performed first on glass substrates without the bCC samples on them, to characterize the substrate porosity. The results are shown in Figure 3-12a.

As can be seen, the pore size distribution diagram features five sub-10 nm peaks corresponding to the porous nature of the glass substrates. However, when the same analysis was repeated for the same type of glass substrates with the sample bCCs, of 150 and 30 nm, another peak at 16.23 nm emerged, Figure 3-12b, which is attributed to the mesoporosity nature of the colloidal structure. This value however is about 49% larger than 10.88 nm, determined by theoretical calculations. The broadness of this peak is probably due to the presence of defects that invade the structures during the final evaporation stage.

Figure 3-14 shows the pore size distribution of the mCCs of 100 nm silica particles. These crystals were etched from the substrate and gently put into the equipment sample holder. According to these results, a majority of the pore sizes in the distribution is distinguished as sub-10 nm, we believe this result is attributable to the particle porosity, rather than the mCC itself. Geometrical considerations place the mean pore size of this mCC in the range of 15 nm. Figure

3-12b shows the 150 and 30 nm particle mixture composed of silica that has internal pores in the sub-10 nm range. Since no lattice sized pores are seen in Figure 3-14, it may be that the density of pores in the 100 nm particles far exceeds the density of lattice based pores, as their signal is not observed.

In the next sections, the protein separation studies performed on the different colloidal crystals with different mean pore sizes, fabricated here, will be discussed.

3.3.2 Separation of SDS-Denatured Proteins

3.3.2.1 Injection and separation schemes

Injection and separation of proteins was performed on microfabricated PDMS chips shown schematically in Figure 3-1. Plug shaping[54, 55] was used to minimize band broadening during sample loading[5] by applying +29 V at sample reservoir (2) against the waste reservoir (3) kept grounded. Buffer (1) and buffer waste (4) reservoirs were also kept grounded to make a “shaped” injection plug, shown in Figure 3-15a.

Sample loading was given enough time to ensure a high intensity sample plug for later analyte detection.

A home-made electrical relay system was used to switch from injection to separation mode. Voltages at buffer waste and buffer reservoirs were switched to +45 V and ground, respectively, while +29 V was applied at the two other reservoirs, sample and sample waste, to create a “push-back” process, avoiding further sample leakage. No evidence of a turbulent regime was distinguished upon switching, due to charging current flow, which would contribute to band broadening[5]. As shown in Figure 3-15b, the sample amount in the microchannels, leading to sample and sample waste, were effectively pushed back by the +29 V. The three fluorescing bands captured by the digital CCD camera about 3.5 minutes after switching time, correspond to the separation of free dye, FITC-ovalbumin (45kD) and FITC-BSA (66kDa) are shown in Figure 3-15c.

These applied voltages for the push-back and separation stages were chosen according to an electrical chip simulation using PSpice Schematics software (v9.1)[56]. In this simulation, each microchannel was taken as an electrical resistance with a magnitude dependent on the channel cross-section, length and the material trapped within it, i.e. packed particles and a running buffer. The subtle changes in the geometry of the walls of the microchannels that might affect the current and voltage values are ignored. Assuming that the buffer and the colloidal crystal are in equilibrium after a fairly long period of storage overnight, all microchannels should have the same type of material, hence any heterogeneity in contribution to the electrical resistance was ignored. Taking into account that all the microchannels have the same cross-section area, 120 µm × by 20 µm, it is concluded that the only contributor to their differences of electrical resistance is their lengths. Therefore, the values of the resistances were chosen as factors of the microchannels length values.

Based on simulation results, the selected voltage scheme for the separation mode results in the voltage of +24 V for the double-T area. Accordingly, with a voltage of +45 V in the buffer waste reservoir, 7 mm away, the external electrical field strength should be about 30 V/cm. Furthermore, the simulation revealed that the electrical current flowing from the sample and sample waste channels are directed toward the double-T area. Therefore negatively charged SDS-denatured protein would migrate away from the double-T area, which confirms the desired push-back. To keep the field strength within a targeted value, the channel lengths, i.e. reservoirs locations, and the voltage scheme for the injection and separation were kept the same for all the protein separation experiments in this study.

One important issue regarding the PDMS chip has been its nanoporous structure[57], which imposes further evaporation of water molecules from its bulk, including the microchannels. In fact, further evaporation of water from the PDMS may concentrate the running buffer leading to crystallization of salt in the interstices of colloidal crystal inside the microchannels. Higher background imposed by light scattering, smaller than expected pore sizes and disturbance of the crystalline pattern of the nanolattice are some foreseeable major consequences affecting separation quality and quantification caused by salt crystallization.

Weight of the PDMS chip that has been transferred from the humid petri dish to the weighing station at ambient conditions was measured every 6 minutes. Values of the current minus the initial weight were plotted against time in Figure 3-16a.

A demonstration of the apparent water loss of a PDMS chip on a glass substrate during electrophoresis is also shown in Figure 3-16b after 10 minutes. To considerably minimize evaporation of the water content, a blanket of humidified paper tissue were wrapped around the peripheral and upper region of the PDMS chip in such a way not to disturb electrode arrangements and make any short electrical connection between them in the four reservoirs. This blanket was periodically kept humid by injection of a few micro litters of water during electrophoretic separation.

3.3.2.2 Measurements of the electrophoretic mobilities

The mobilities of SDS-denatured FITC-labeled proteins for all experimental sets in this study were measured 4 mm away from the double-T location injector. This measured mobility is not the free solution electrophoretic mobility calculated by equation 1-5, because this measured mobility includes the frictional effects of the crystal structure. After observing injection, the detector was then located at the separation detection point. Analytes where detected in a sequence corresponding to their molecular weights. The PDMS microfluidic chips surface used in this study were native, without further treatment prior to analysis.

To reduce the siphoning effect and equalize electro osmotic flow rates throughout the device, the particle bed was grown throughout the device.

According to Figure 3-17a, nanoporous crystal of 310 nm silica particles, presenting an average pore size of 48 nm, do not resolve the three expected peaks effectively. Nonetheless, a minor peak of free dye is observable at about 3.4 minute, though it is not baseline resolved. However, with a smaller lattice pore size of 23 nm in the mCC of 150 nm, the separation does discriminate between labeled SDS-protein complexes based on their molecular weights, as can be clearly seen in Figure 3-17b. With an average smaller pore size of 11 nm, in the case of 150 nm mixed with 30 nm silica particles, more differentiation in the elution times of the proteins was observed, these proteins are better baseline resolved, as by comparing Figure 3-17b and c.

Separation of trypsin inhibitor (20.1 kDa) and BSA (66 kDa) in an mCC of 310 nm particles, Figure 3-18a, however, revealed that these larger particles afford resolution of peaks for proteins that are 46 kDa different in molecular weight, even when proteins ovalbumin (45 kDa) and BSA (66 kDa) with only 21 kDa difference could not be separated, Figure 3-17a. Furthermore, similar to Figure 3-17c, baseline resolution with a longer peak-to-peak distance results from the separation in 11 nm pore size of the bCC, as per Figure 3-18b.

These separation results at the same external field strength suggest that the separation of these three proteins is actually based exclusively on their hydrodynamic sizes[58] and the pore structure of the crystal.

Figure 3-19 shows the measured mobilities of trypsin (20.1 kDa), ovalbumin (45 kDa) and BSA (66 kDa). As is evident, all proteins show a downward trend in the electrophoretic mobilities, as the average pore size of the nanoporous media shrinks. An interesting feature of these results is the rate at which these mobilities collapse. As the protein molecular weight increases it shows a sharper decrease with pore size compared to its counterparts in the same pore size regime. This behavior in protein migration through the nanoporous crystal can be described by a protein and pore size argument.

Hydrodynamic radii of denatured proteins have been studied by several authors.[59-61] Based on a pulsed field gradient NMR approach, recently Wilkins et al. have proposed the following empirical model for the calculation of the hydrodynamic radii of denatured proteins[61]

$$R_{\mathrm{hyd.}} = (2.21 \pm 1.07)N^{0.57 \pm 0.02} \qquad (3\text{-}2)$$

where N is the number of residues in the polypeptide chain. According to the predictions of this equation the diameter of the proteins applied in this study is shown in Table 3-2. The hydrodynamic diameter is the diameter of a spherical particle that has the same diffusion coefficient as the protein molecule.[62]

The standard deviations in the Table 3-2 are calculated based on different arrangements of the plus and minus signs in equation (3-2). BSA (66 kDa), with the largest hydrodynamic size shows a steeper decrease in its mobilities from 48 to 11 nm of the pore size than trypsin inhibitor (20.1 kDa), that is not as affected through the same pore size spectra.

Table 3-2 - Hydrodynamic diameter of the SDS-denatured proteins studied here as estimated by equation (3-2)

Protein	Molecular weight [kDa]	Number of amino acid residues	Hydrodynamic diameter [nm] from equation (3-2)
trypsin inhibitor	20.1	181	8.60 ± 4.94
ovalbumin	45	385	13.24 ± 7.67
BSA	66	585	16.83 ± 9.80

The mean hydrodynamic size values listed in the above table suggest that protein separation will be governed by Ogston sieving[63] in mCCs with an average pore size of 48 nm to 15 nm, which is larger than the studied protein sizes. However, reptation, or at least transition to it, might be a factor in the 15 nm (nominal) pores of the mCC and 11 nm (nominal) pores of the bCC. This conclusion is consistent with small angle neutron scattering (SANS) studies that these SDS-denatured proteins are flexible[64, 65] globular particles with a random coil orientation of the polypeptide chain that has been unfolded during heat and SDS denaturation process. [66, 67] Without this random coil flexibility, these proteins could not be electrokinetically injected, separated and detected. However, as is evident from in Figure 3-17c and Figure 3-18b, the peaks of ovalbumin (45 kDa) and BSA (66 kDa), for an average pore size of 11 nm, indicate that they have been injected into the structure even if the structure pore size is smaller than their hydrodynamic sizes.

The band broadening, specifically for the FITC in Figure 3-17c, is a major consequence of the longer injection time that in fact has contributed to the diffusion of the sample analyets before separation resulting in a broader sample plug and hence fluorescent peaks. Also a contributor to the broader band of ovalbumin (45 kDa) and BSA (66 kDa), in Figure 3-17c, and also trypsin (20.1 kDa), in Figure 3-18b, might be a more sensitive molecular weight discrimination capability of the bCC in ready capturing heterogeneously FITC-labeled proteins within the same molecular regime, as it has smaller pore size.[68]

Figure 3-20 is an electropherogram of a separation performed on mCCs of 50 nm silica particles, that based on geometrical calculations provides an average pore size of 7.7 nm. According to this highly reproducible result, there are three peaks that can be distinguished. Based on the previous results, the first sharp and tall peak can be assigned to the free dye, FITC. This peak also shows up about 1.4 minutes earlier than the other mCCs which is probably due to lower EOF in this nanostructure. The other peaks may correspond to ovalbumin (45 kDa) and BSA (66 kDa). However, surprisingly their electrophoretic mobilities are higher in this experiment than in larger particle beds. The nominal pore size of 7.7 nm, in a structure of 50 nm particles, is smaller than the hydrodynamic sizes of these proteins, according to Table 3-2. It can be concluded that protein separation may be governed by reptation in this bed. In this regime proteins have higher mobilities as they travel through the structure, recruiting a rode-like shape that incurs less friction than when they have a globular shape. The poor separation resolution might be due to the less difference in electrophoretic mobilities in the rode-like motion regime through the structure.

3.4 Conclusions

Micro-crack and air-invaded free monomodal colloidal crystals of micro and nano particles were fabricated based on a microfluidic approach. Based on the analysis of the mathematical crack models presented to date, developments of the micro-cracks are assigned to the rate of dispersant (water) evaporation at the evaporation edge. It was found that with fixed channel geometry, micro-crack development can be ceased by decreasing dispersant evaporation during CSA. In fact, by decreasing the evaporation rate, the micro-crack spacing can be increased. Therefore, from a threshold value onward the spacing are higher than the microchannel dimension and hence no opportunity for a crack to be initiated and grow.

The problem of air-invasion was serious in the mCCs of 30 and 50 nm particles because as the mean pore sizes shrink the viscous resistance acting against the dispersant flow increases. Therefore with the evaporation rate of the dispersant to the ambient environment, that was higher than the transport of the replenishing dispersant through the bulk of the nanoporous media, the parts of the crystal closest to the ambient conditions start getting completely dried.

Nanoporous structures of 150 doped with 30 nm particles and crystals of 100 nm particles were subjected to sorption analysis, based on the adsorption of krypton in 87 K, to better understand their mesoporous structures. According to these analyses it was concluded that the applied micro- and nanoparticles are highly porous with a size ranging from 1 to 10 nm. However, the pore size distribution of the colloidal crystal itself, as a porous media, did not reveal useful information probably due to the low amount of crystal samples dictated by the difficult sample preparation procedure. Furthermore, since the final stage of evaporation incurs inevitable cracks and structural defects, sorption porosimetry reveals very broad peaks that are not reliable to judge about the effective pore size of these crystals. This was shown for a bCC of 150 and 30 nm particles. The peak was distributed from a value of about 5 to 185 nm while a peak of 11 nm is expected from this analysis.

Table 3-3 summarizes the results of protein separation along with the suggested separation regimes.

Table 3-3 - Summery of the protein separation results at different pore sizes

Particle size [nm]	Structure pore size [nm]		Separation results	Separation Regime
	nominal	measured		
310	48		• 45 and 66 kDa not resolved • 20 and 45 kDa resolved	Ogston
150	23		• 45 and 66 kDa resolved	
100	15.5		• 45 and 66 kDa resolved • 20 and 45 kDa resolved	
30/150	10.5	~16	• 45 and 66 kDa resolution increased • 20 and 45 kDa resolution increased	Transition to reptation
50	7.7		• A transition to reptation regime is suggested	Reptation

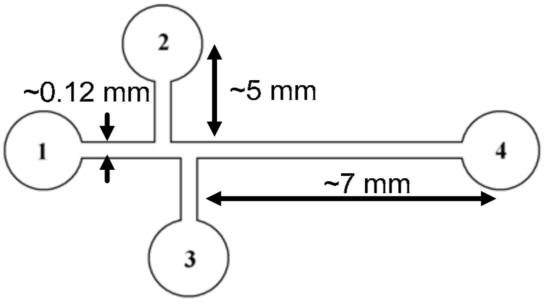

Figure 3-1 A schematic presentation of the microfluidic chip.

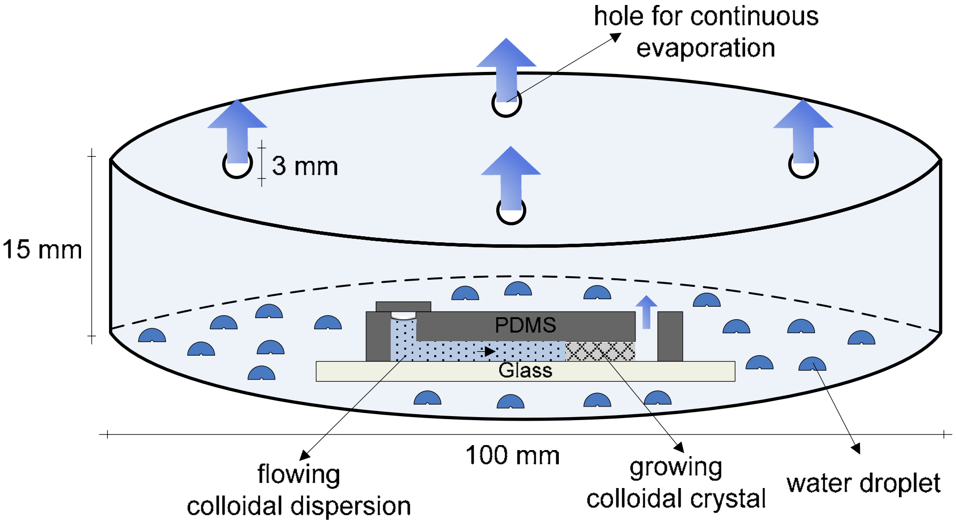

Figure 3-2 Schematic diagram of the microfluidic approach for the fabrication of the mCCs of sub-100 nm silica particles, micro-crack and air-invaded free.

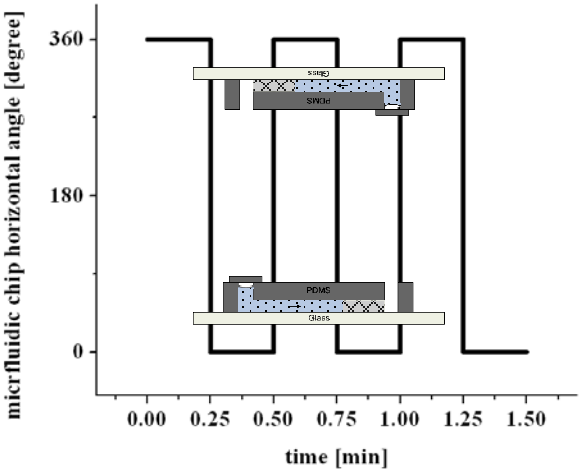

Figure 3-3 Diagram of a microfluidic chip angular position as imposed by the periodic chip rotator.

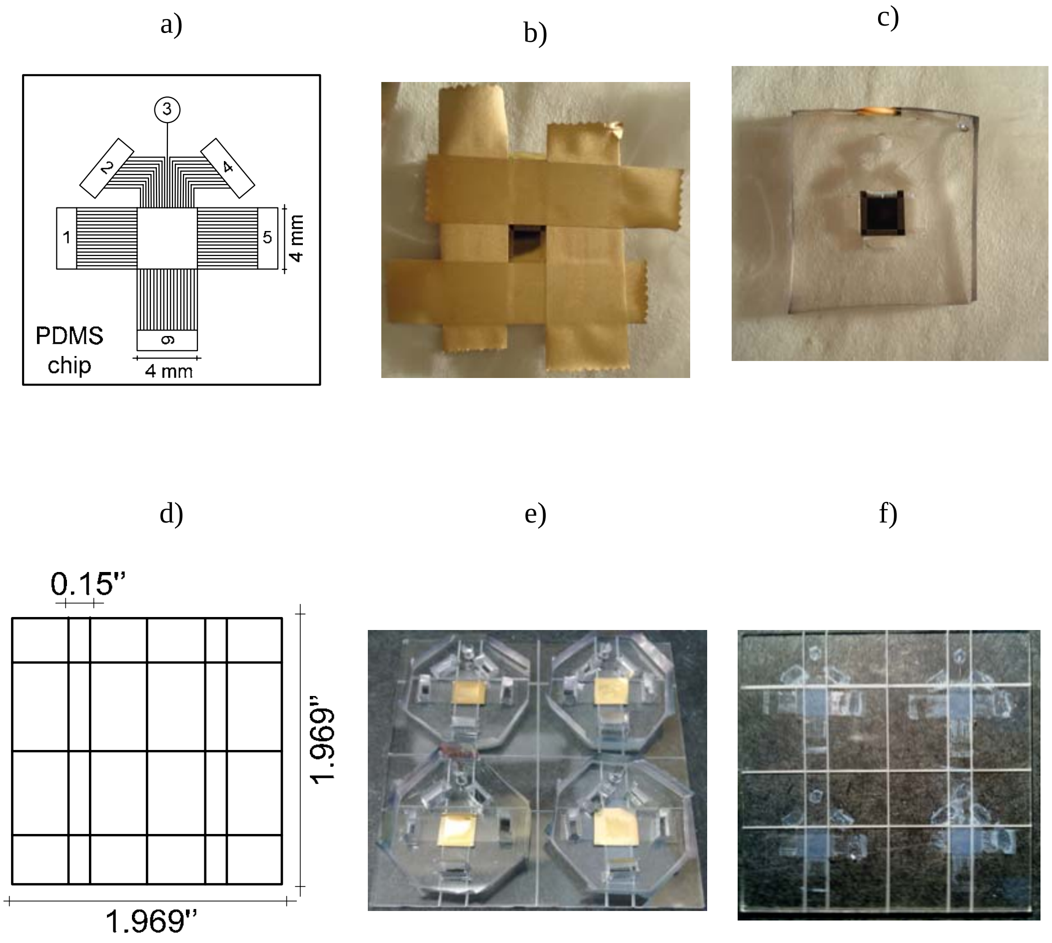

Figure 3-4 Images of sample preparation process. a) the PDMS chip. b) A PDMS chip sputtred with gold with plastic tapes to mask-off desired regions. c) PDMS chip with the plastic tapes peeled-off. d) The pre-diced glass substrate. e) PDMS chips with selectively sputtered gold regions on a pre-diced glass substrate. f) Colloidal crystals deposited on a glass substrate after the PDMS chips were successfully peeled-off.

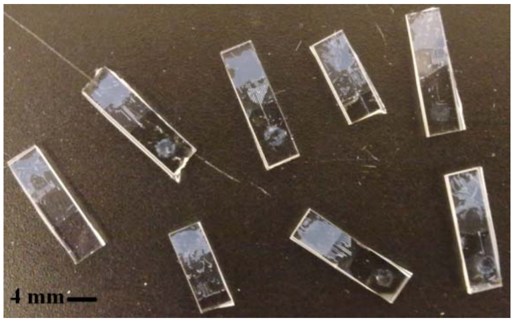

Figure 3-5 Photo of the colloidal crystals on the cut glass substrates prepared for porosimetry.

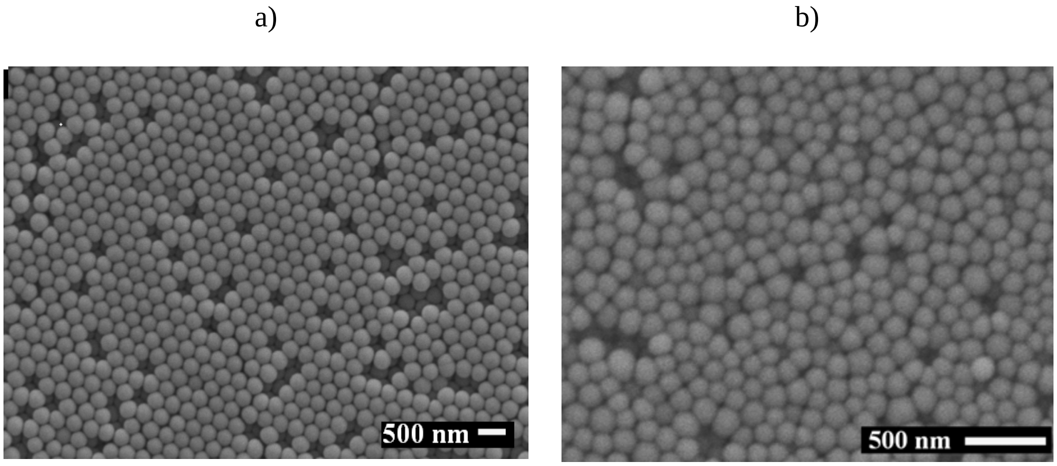

Figure 3-6 Top-down SEM images silica microparticles. a) 310 nm. b) 150 nm.

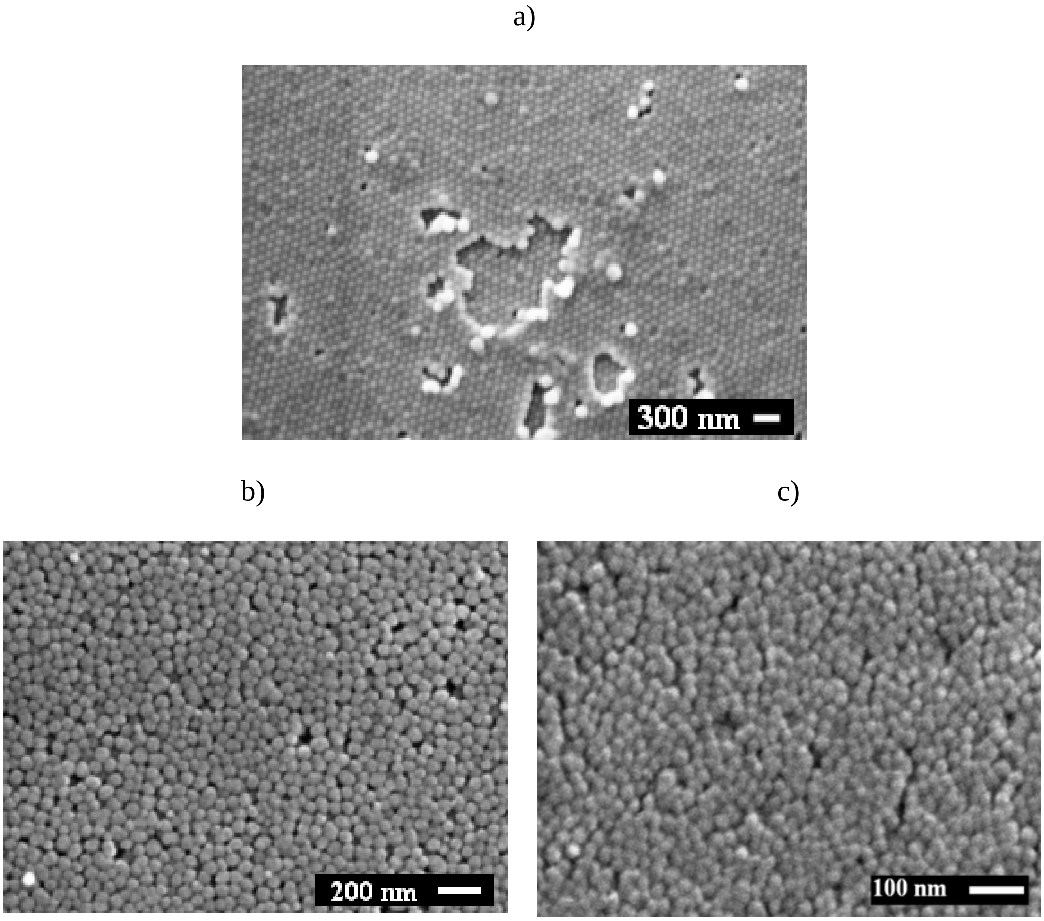

Figure 3-7 Top-down SEM images of silica nanoparticles. a) 100 nm b) 50 nm c) 30 nm

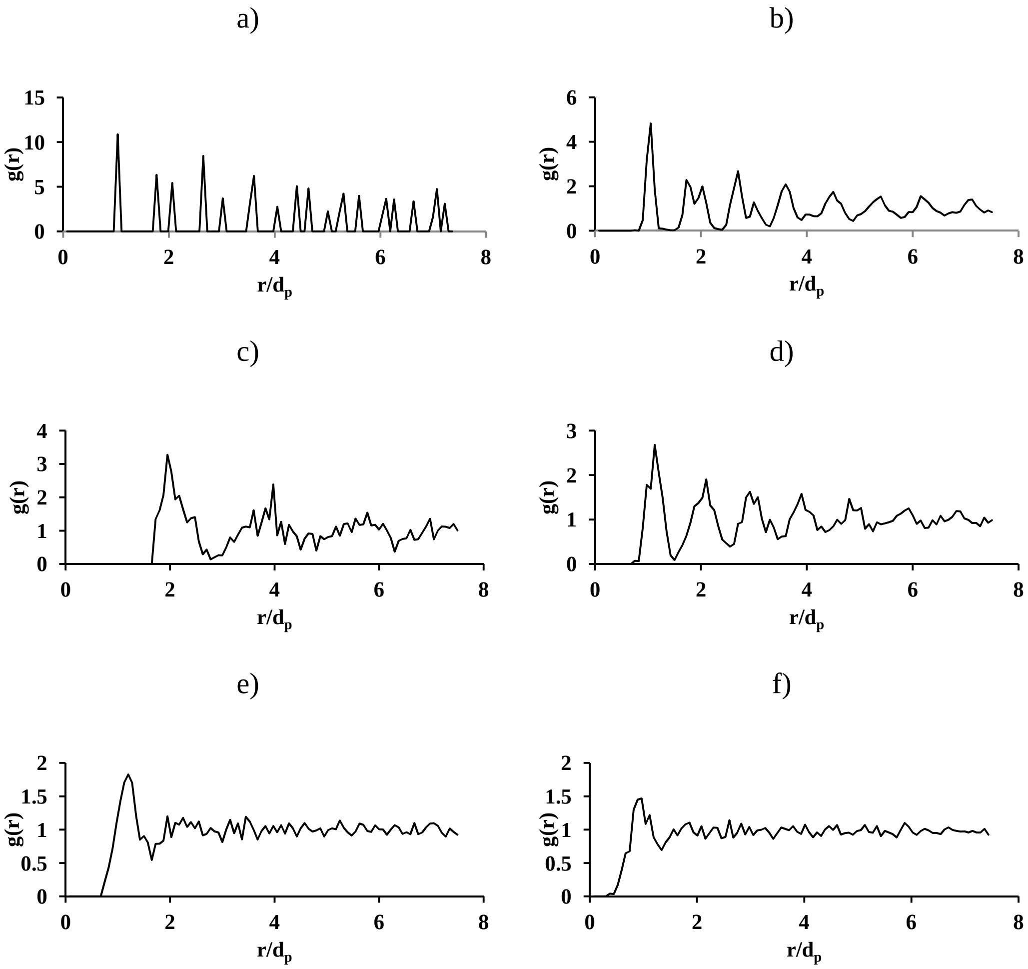

Figure 3-8 Profile of the radial distribution function of the colloidal crystals, g(r). a) Ideal hexagonally closed-packed (ψ=1). b) 310 nm (ψ=0.93±0.015). c) 150 nm (ψ=0.72±0.04). d) 100 nm (ψ=0.86±0.01). e) 50 nm (ψ=0.42±0.06). f) 30 nm (ψ=0.65±0.06).

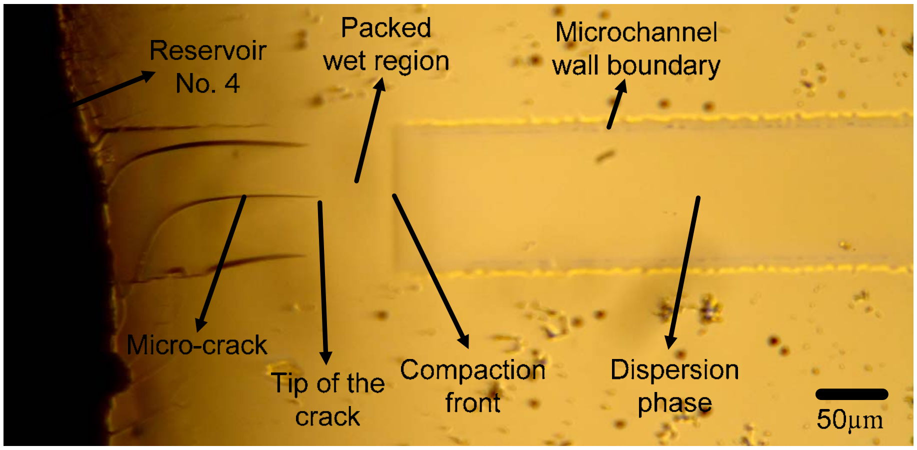

Figure 3-9 Micrograph of a PDMS microchannel and the mCC of a 30 nm silica particles growing with the three just emerged micro-cracks.

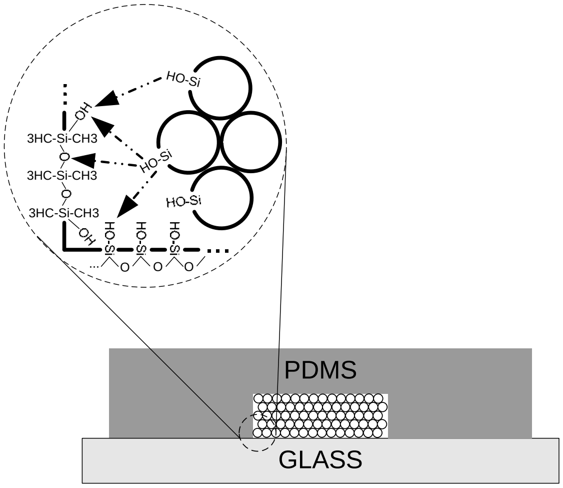

Figure 3-10 Demonstration of the mechanisms of silica adhesion to the surface of PDMS chip and the glass substrate.

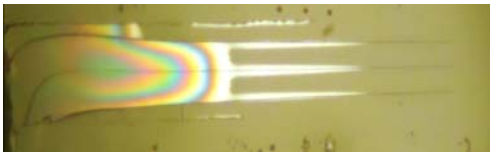

Figure 3-11 Bright-field micrograph of mCC of 30 nm silica particles in a microfluidic PDMS channel. Three parallel growing micro-cracks and air-invaded regions near the channel outlet are shown.

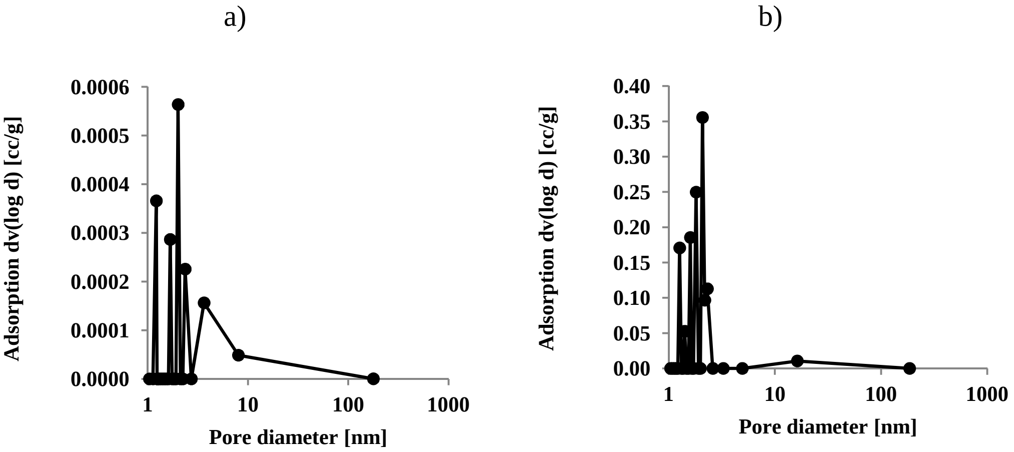

Figure 3-12 Pore size distribution as measured and calculated by sorption analyzer. a) clean unused glass substrate. b) bCC of 150 and 30 nm.

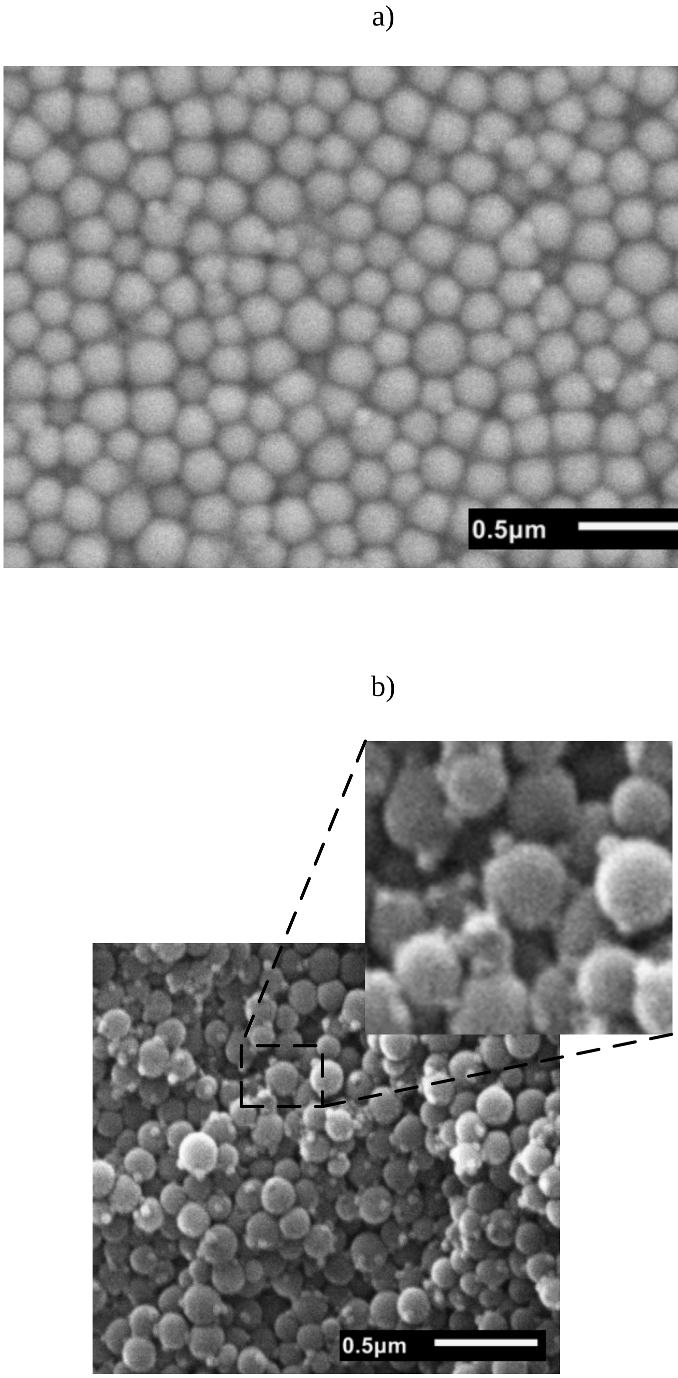

Figure 3-13 SEM images of bCC of 150 and 30 nm silica particles. a) top view. b) cross-sectional view.

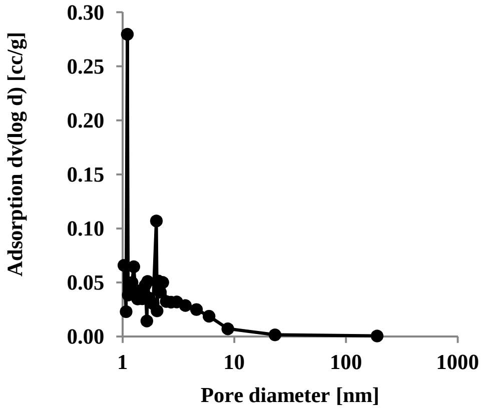

Figure 3-14 Pore size distribution as measured and calculated by sorption analyzer for mCCs of 100 nm silica.

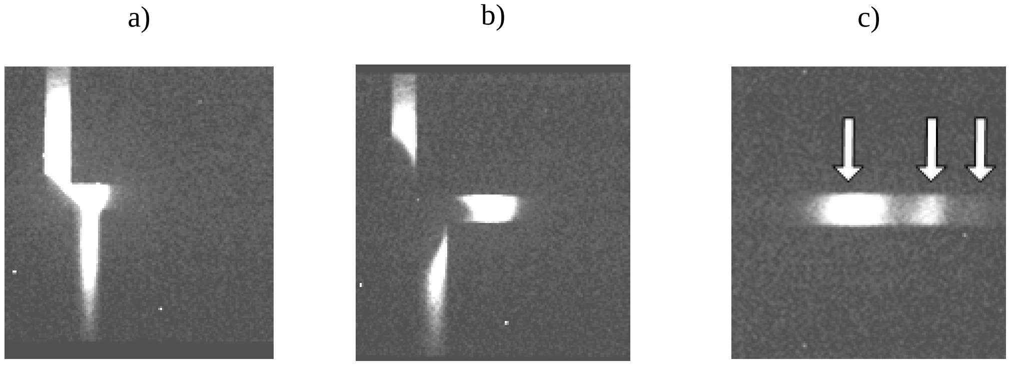

Figure 3-15 Schematic of protein separation as observed in CCD camera; injection, push-back and separation. a) Injection b) Push-back c) Separation (the three peaks are, from left to right, free dye, ovalbumin (45 kDa) and BSA (66 kDa)).

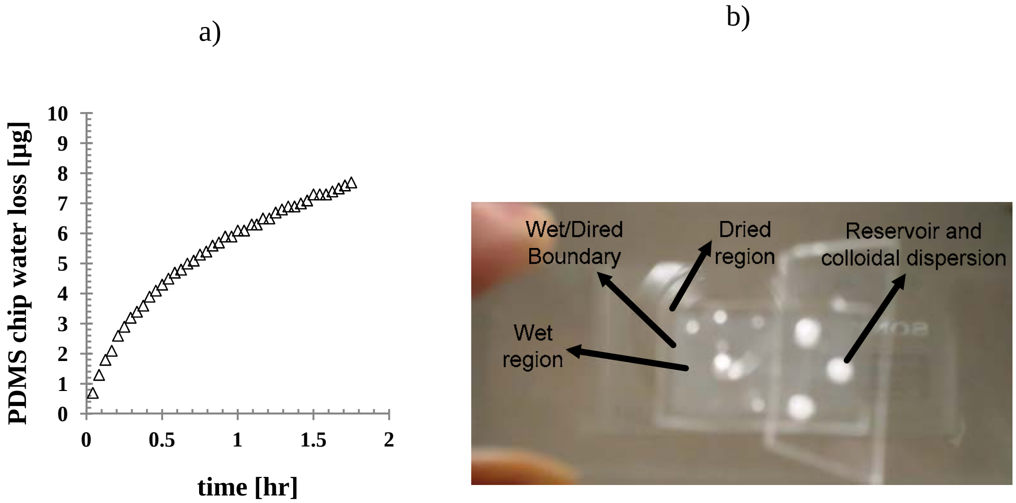

Figure 3-16 PDMS chip water loss versus time. a) Weigh of PDMS chip compared to its initial value. b) Photo of a drying PDMS chip with dried and still wet regions.

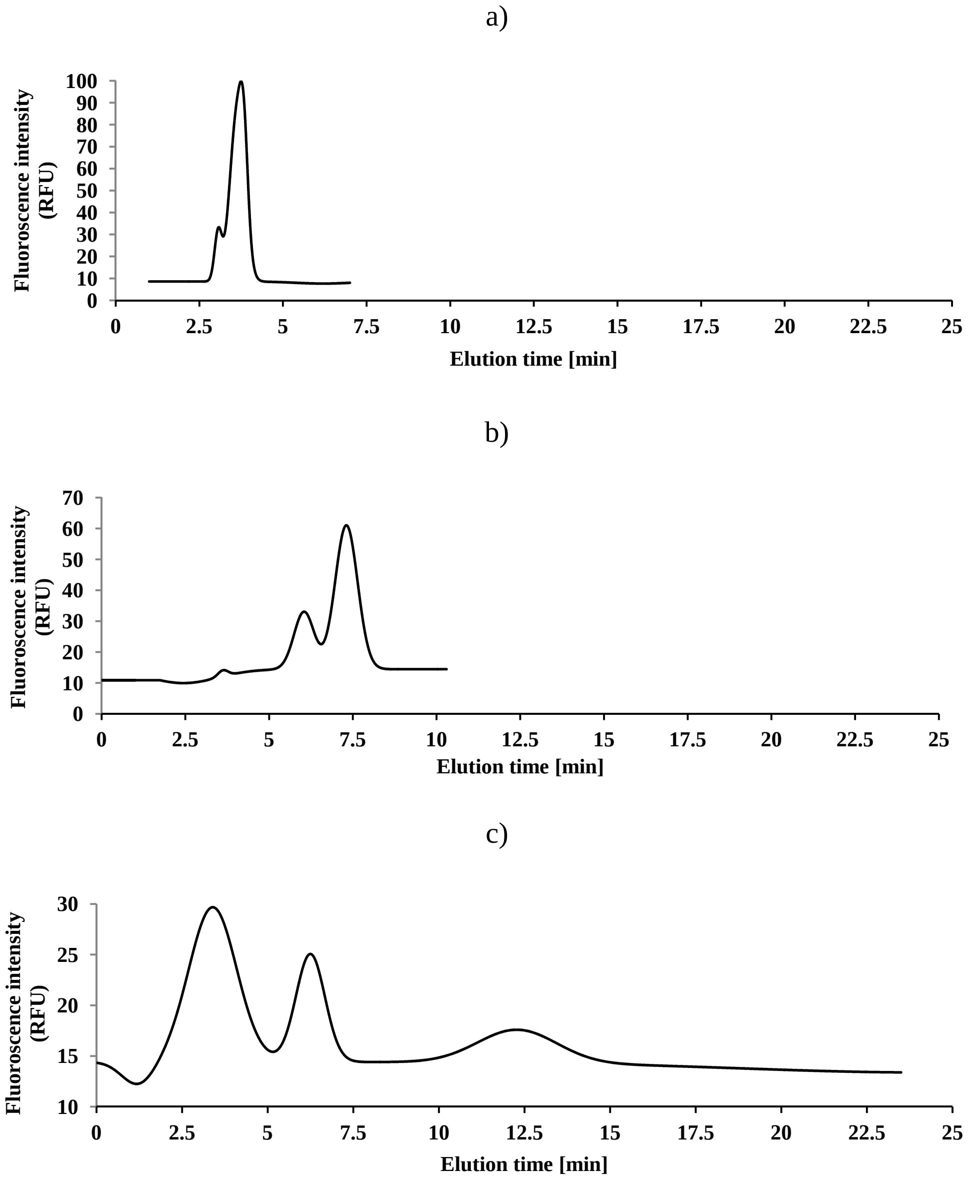

Figure 3-17 Electropherograms of FITC, ovalbumin (45 kDa) and BSA (66 kDa) separation at 30 V/cm as observed at 4 mm. a) mCC of 310 nm. b) mCC of 150 nm. c) bCC of 150 and 30 nm.

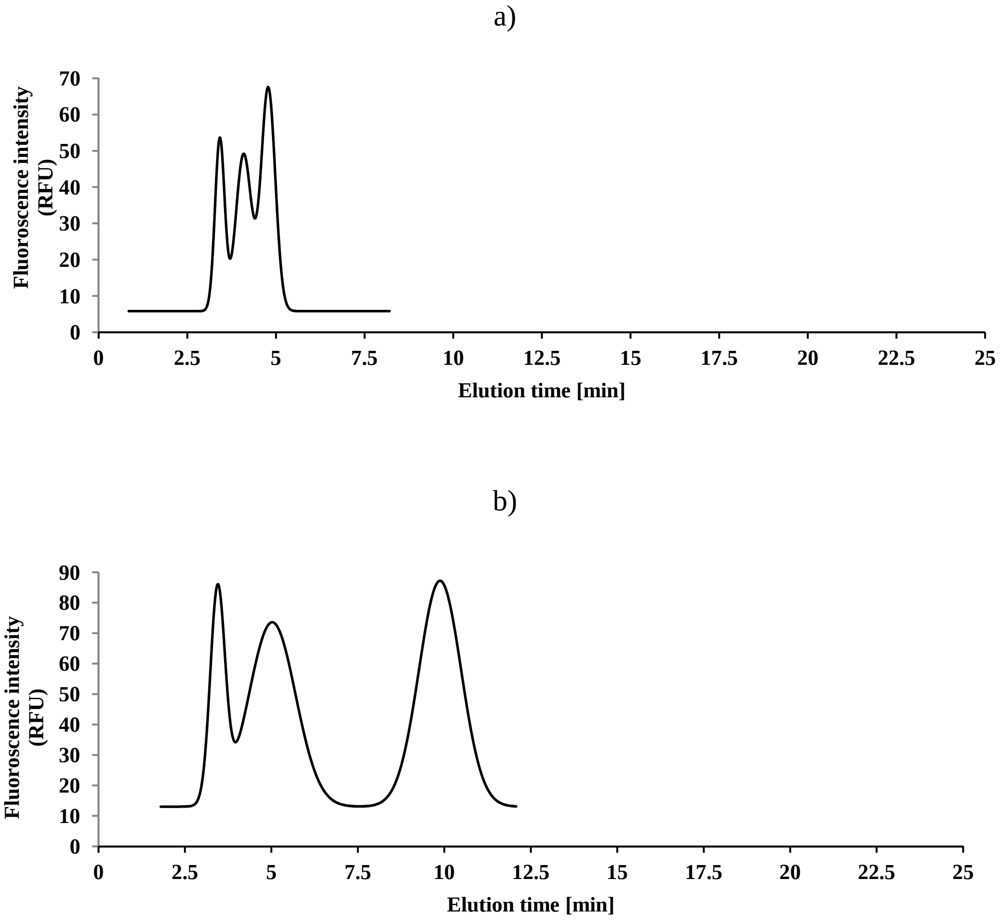

Figure 3-18 Electropherograms of FITC, trypsin (20.1 kDa) and BSA (66 kDa) separation at 30 V/cm as observed at 4 mm. a) mCC of 310 nm. b) bCC of 150 and 30 nm.

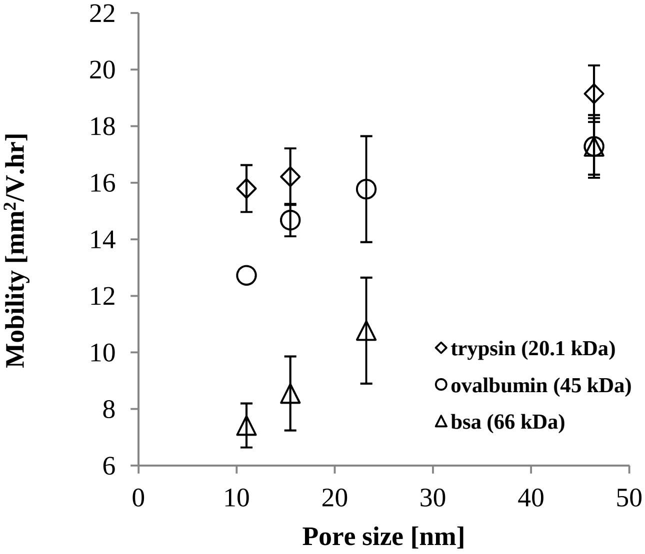

Figure 3-19 Plot of mobilities of different proteins at different pore sizes at 30 V/cm.

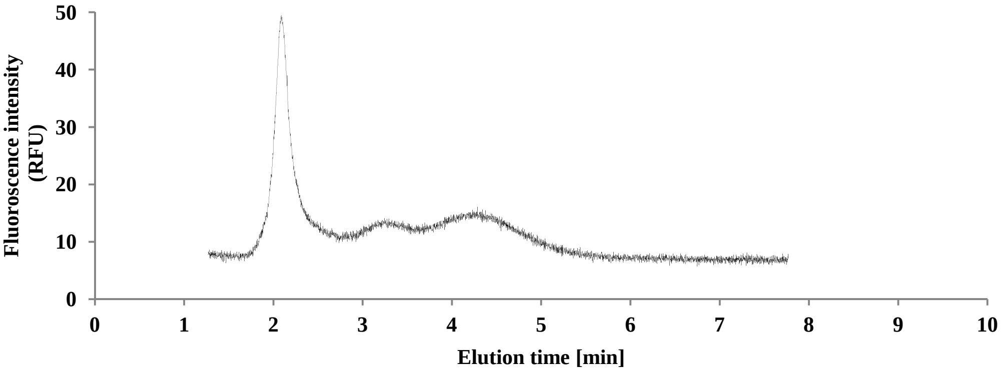

Figure 3-20 Electropherograms of FITC, ovalbumin (45 kDa) and BSA (66 kDa) separation at 30 V/cm as observed at 4 mm in an mCC of 50 nm silica particles.

3.5 References

[1] Lee, Y. S. *Self-Assembly and Nanotechnology: A Force Balance Approach*; John Wiley & Sons, Inc., Hoboken, New Jersey, 2008.

[2] Jemere, A.B., Martinez, D., Finot, M., Harrison, D.J. *Electrophoresis* **2009**, *30*, 4237–4244.

[3] Jemere, A.B., Oleschuk, R.D., Harrison, D.J. *Electrophoresis* **2003**, *24*, 3018–3025.

[4] Jemere, A.B., Oleschuk, R.D., Ouchen, F., Fajuyigbe, F., Harrison, D.J. *Electrophoresis* **2002**, *23*, 3537–3544.

[5] Park, J., Lee, D., Kim, W., Horiike, S., Nishimoto, T., Se, H.L., Ahn, C.H. *Analytical Chemistry* **2007**, *79*, 3214–3219.

[6] Hua, Y., Koshel, B.M., Wirth, M.J. *Analytical Chemistry* **2010**, *82*, 8910–8915.

[7] Zeng, Y., He, M., Harrison, D.J. *Angewandte Chemie - International Edition* **2008**, *47*, 6388–6391.

[8] Zeng, Y., Harrison, D.J. *Electrophoresis* **2006**, *27*, 3747–3752.

[9] Nazemifard, N., Wang, L., Ye, W., Bhattacharjee, S., Masliyah, J.H., Harrison, D.J. *Lab on a Chip - Miniaturisation for Chemistry and Biology* **2012**, *12*, 146–152.

[10] Nazemifard, N., Bhattacharjee, S., Masliyah, J.H., Jed Harrison, D. *Angewandte Chemie - International Edition* **2010**, *49*, 3326–3329.

[11] Wei, B., Malkin, D.S., Wirth, M.J. *Analytical Chemistry* **2010**, *82*, 10216–10221.

[12] Zeng, Y., Harrison, D.J. *Analytical Chemistry* **2007**, *79*, 2289–2295.

[13] ImageJ: Image Processing and Analysis in Java. 2012; http://-rsbweb.nih.gov/ij/.

[14] Gates, B., Xia, Y. *Applied Physics Letters* **2001**, *78*, 3178–3180.

[15] Verhaegh, N.A.M., Van Duijneveldt, J.S., Van Blaaderen, A., Lekkerkerker, H.N.W. *The Journal of Chemical Physics* **1995**, *102*, 1416–1421.

[16] Gasser, U. *Journal of Physics Condensed Matter* **2009**, *21*.

[17] Hoogenboom, J.P., Van Langen-Suurling, A.K., Romijn, J., Van Blaaderen, A. *Physical Review E - Statistical, Nonlinear, and Soft Matter Physics* **2004**, *69*, 051602–1–051602–18.

[18] Wang, J., Li, Q., Knoll, W., Jonas, U. *Journal of the American Chemical Society* **2006**, *128*, 15606–15607.

[19] Auer, S., Frenkel, D. *Nature* **2001**, *409*, 1020–1023.

[20] Kofke, D.A., Bolhuis, P.G. *Physical Review E - Statistical Physics, Plasmas, Fluids, and Related Interdisciplinary Topics* **1999**, *59*, 618–622.

[21] Brouwers, H.J.H. *Physical Review E - Statistical, Nonlinear, and Soft Matter Physics* **2007**, *76*.

[22] Arora, A.K., Tata, B.V.R. *Advances in Colloid and Interface Science* **1998**, *78*, 49–97.

[23] Auer, S., Frenkel, D. *Nature* **2001**, *413*, 711–713.

[24] Jiang, P., Bertone, J.F., Hwang, K.S., Colvin, V.L. *Chemistry of Materials* **1999**, *11*, 2132–2140.

[25] Dimitrov, A.S., Nagayama, K. *Langmuir* **1996**, *12*, 1303–1311.

[26] Rengarajan, R., Mittleman, D., Rich, C., Colvin, V. *Physical Review E - Statistical, Nonlinear, and Soft Matter Physics* **2005**, *71*.

[27] Saunders, A.E., Korgel, B.A. *ChemPhysChem* **2005**, *6*, 61–65.

[28] Palacios-Lidon, E., Juarez, B.H., Castillo-Marti-nez, E., Lopez, C. *Journal of Applied Physics* **2005**, *97*.

[29] Rabideau, B.D., Pell, L.E., Bonnecaze, R.T., Korgel, B.A. *Langmuir* **2007**, *23*, 1270–1274.

[30] Li, F., Josephson, D.P., Stein, A. *Angewandte Chemie - International Edition* **2011**, *50*, 360–388.

[31] Goldenberg, L.M., Jung, B.-D., Wagner, J., Stumpe, J., Paulke, B.-R., Gornitz, E. *Langmuir* **2003**, *19*, 205–207.

[32] Grzelczak, M., Vermant, J., Furst, E.M., Liz-Marzan, L.M. *ACS Nano* **2010**, *4*, 3591–3605.

[33] Kumacheva, E., Garstecki, P., Wu, H., Whitesides, G.M. *Physical Review Letters* **2003**, *91*, 1283011–1283014.

[34] Meijer, J.-M., De Villeneuve, V.W.A., Petukhov, A.V. *Langmuir* **2007**, *23*, 3554–3560.

[35] Wang, C., Zhang, Y., Dong, L., Fu, L., Bai, Y., Li, T., Xu, J., Wei, Y. *Chemistry of Materials* **2000**, *12*, 3662–3666.

[36] Vermant, J., Solomon, M.J. *Journal of Physics Condensed Matter* **2005**, *17*, R187–R216.

[37] Martin, S., Bryant, G., Van Megen, W. *Physical Review E - Statistical, Nonlinear, and Soft Matter Physics* **2005**, *71*.

[38] Paquet, C., Allard, M., Gledel, G., Kumacheva, E. *Journal of Physical Chemistry B* **2006**, *110*, 1605–1613.

[39] Zhang, X., Tang, G., Yang, S., Benattar, J.-J. *Langmuir* **2010**, *26*, 16828–16832.

[40] Huang, Y., Pemberton, J.E. *Colloids and Surfaces A: Physicochemical and Engineering Aspects* **2011**, *377*, 76–86.

[41] Mason, G. *Nature* **1968**, *217*, 733–735.

[42] Scott, G.D. *Nature* **1962**, *194*, 956–957.

[43] Aste, T. *Journal of Physics Condensed Matter* **2005**, *17*, S2361–S2390.

[44] Dufresne, E.R., Stark, D.J., Greenblatt, N.A., Cheng, J.X., Hutchinson, J.W., Mahadevan, L., Weitz, D.A. *Langmuir* **2006**, *22*, 7144–7147.

[45] Dufresne, E.R., Corwin, E.I., Greenblatt, N.A., Ashmore, J., Wang, D.Y., Dinsmore, A.D., Cheng, J.X., Xie, X.S., Hutchinson, J.W., Weitz, D.A. *Physical Review Letters* **2003**, *91*, 224501/1–224501/4.

[46] Jing, G., Ma, J. *The journal of physical chemistry. B* **2012**, *116*, 6225–6231.

[47] Gauthier, G., Lazarus, V., Pauchard, L. *Langmuir* **2007**, *23*, 4715–4718.

[48] Allain, C., Limat, L. *Physical Review Letters* **1995**, *74*, 2981–2984.

[49] Komatsu, T.S., Sasa, S.-I. *Japanese Journal of Applied Physics, Part 1: Regular Papers and Short Notes and Review Papers* **1997**, *36*, 391–395.

[50] Routh, A.F., Russel, W.B. *AIChE Journal* **1998**, *44*, 2088–2098.

[51] Marinova, K.G., Christova, D., Tcholakova, S., Efremov, E., Denkov, N.D. *Langmuir* **2005**, *21*, 11729–11737.

[52] Lowell, S., Shields, J. E., Thomas, M. A., Thommes, M. *Characterization of Porous Solids and Powders: Surface Area, Pore Size and Density (Particle Technology Series)*; Springer: Netherlands, 2006.

[53] Krause, K.M., Thommes, M., Brett, M.J. *Microporous and Mesoporous Materials* **2011**, *143*, 166–173.

[54] Roddy, E.S., Xu, H., Ewing, A.G. *Electrophoresis* **2004**, *25*, 229–242.

[55] Chiem, N.H., Harrison, D.J. *Clinical Chemistry* **1998**, *44*, 591–598.

[56] PSpice Schematics: Cadence Design Systems. 2012; http://-www.electronics-lab.com/downloads/schematic/013/.

[57] Mizutani, F., Yabuki, S., Sawaguchi, T., Hirata, Y., Sato, Y., Iijima, S. *Sensors and Actuators, B: Chemical* **2001**, *76*, 489–493.

[58] Cohen, A.S., Karger, B.L. *Journal of Chromatography A* **1987**, *397*, 409–417.

[59] Garci-a De La Torre, J., Huertas, M.L., Carrasco, B. *Biophysical Journal* **2000**, *78*, 719–730.

[60] Damaschun, G., Damaschun, H., Gast, K., Zirwer, D. *Biochemistry (Moscow)* **1998**, *63*, 259–275.

[61] Wilkins, D.K., Grimshaw, S.B., Receveur, V., Dobson, C.M., Jones, J.A., Smith, L.J. *Biochemistry* **1999**, *38*, 16424–16431.

[62] Masliyah, J. H.; Bhattacharjee, S. *Electrokinetic and Colloid Transport Phenomena*; JohnWiley & Sons, Inc.: Hoboken, New Jersey, 2006.

[63] Sartori, A., Barbier, V., Viovy, J.-L. *Electrophoresis* **2003**, *24*, 421–440.

[64] Guo, X.H., Zhao, N.M., Chen, S.H., Teixeira, J. *Biopolymers* **1990**, *29*, 335–346.

[65] Chen, S.-H., Teixeira, J. *Physical Review Letters* **1986**, *57*, 2583–2586.

[66] Guo, X.-H., Chen, S.-H. *Chemical Physics* **1990**, *149*, 129–139.

[67] Guo, X.-H., Chen, S.-H. *Physical Review Letters* **1990**, *64*, 2579–2582.

[68] Herr, A.E., Singh, A.K. *Analytical Chemistry* **2004**, *76*, 4727–4733.

CHAPTER 4

CONCLUSION AND FUTURE WORK

4.1 Concluding Remarks

This thesis has focused on fabricating nanoporous colloidal crystals with an average pore size smaller than 20 nm in a microfluidic chip for the purpose of protein separation. The primary goal was to making these structures by mixing silica colloidal particles of two different sizes and then investigation of the effect of their pore sizes on the quality of a protein separation experiment. Below, is a summary of the concluding remarks gained through the study in this thesis.

1. Colloidal self-assembly of a mixture of two particle sizes with appropriate size and number ratio is proved to be a flexible approach to engineer pore size of a porous colloidal structure at nano scale.

2. Based on the studies of optical microscopy of crystal growth, particle density has a profound effect upon the growth behavior of the colloidal crystal in a microfluidic channel. Particles made from silica (specific density ≈ 2) behave quite different than particle made from polystyrene (specific density ≈ 1). Silica crystals grow faster than their polystyrene

counterparts at the same solution and ambient conditions. According to hydrodynamic analysis of the flow in the microfluidic chip reservoir and SEM analysis of the morphology of the crystals in the microchannel, the different growth behavior was attributed to sedimentation of silica particles in the reservoir that affects their volume fractions during the self-assembly process. Sedimentation phenomenon changes the stoichiometry of the bimodal crystal as it changes the large and small local particle number ratio that has to be a constant value during the fabrication process.

3. To fabricate a structurally ordered binary crystal in a microfluidic chip, the small to large particle size and number ratio must be within a specific range determined by geometrical consideration. To get a crystal with a structural stoichiometry of LS_2 a small to large particle number ratio of 2.5 for the polystyrene and a ratio of 4 for the silica system are needed. For the later, a periodic chip rotation is necessary to counterbalance the effect of gravity. The small to large particle size ratio must be within 15 to 22% of the larger particle diameters to avoid any disturbance to the skeleton of the larger particles. Increase of smaller particle volume fraction leads to LS_6 structures and further increase is destructs the ordered organized large particles assembly.

4. As the particle diameter approaches sub-100 nm ranges, emergence of micro-cracks and air-invaded areas is inevitable. Therefore it is recommended to keep the ambient condition humidified during the colloidal self-assembly process which slows the assembly process down and avoids internal stress build-up and keeps the crystal wet enough.

5. The quality of particles as the building blocks in terms of polydispersity and sphericalness is the ultimate determining factor on the quality of the resulting structure. Polydispersity values more than 8% give disordered structures. Dynamic light scattering and scanning electron microscopy are two reliable tools for determining polydispersity values.

6. In-situ determination of the structure pore size and distribution is recommended through the krypton adsorption porosimetry at 87 K. This type of analysis may give broad and larger than theory pore sizes that are probably due to structural defects inherent in the structure. These defects are caused by the developed mechanical stress during the final evaporation process. Since the particles showed porous nature, enough amount of sample crystal must be prepared for the analysis to get strong and reliable signals that correspond to the porosity of the crystal not the particles.

7. Separation of trypsin (20.1 kDa), ovalbumin (45 kDa) and bovine serum albumin (66 kDa) proteins showed that at a nominal pore size of 45 nm, only trypsin can be separated and the other two have the same electrophoretic mobilities. However, with a nominal pore size of 11 nm in the case of binary structures made from a mixture of 150 and 30 nm particles, all the three proteins could be successfully separated as their nominal hydrodynamic sizes were comparable to the nominal pore size of the sieving media.

8. Ovalbumin (45 kDa) and bovine serum albumin (66 kDa) proteins in structures made from 50 nm diameter particles migrated with higher mobilities and poorer separation resolution than the previous structures with larger pore sizes. Since the pore size of these structures is nominally smaller than the hydrodynamic radiuses of these proteins, we suggest that reputation might be the governing regime at this scale of pore and protein size.

4.2 Future Work

The research reported herein should be considered as an initial step toward the development of a technology for protein separation that can be commercialized and tailored to clinical and proteomic applications. The idea of doping larger particle structures with the smaller particles to achieve an enough flexibility to engineer the architecture of the self-assembled structure at nano scale was investigated and proved to be feasible and novel. Based on the experience of this study, a few recommendations are made below.

1. Reliable characterization of the colloidal crystal is an important factor in the investigation of the effect of pore size on the protein separation efficiency. In chapter 3, the krypton porosimetry was employed to measure the size and distribution of the pores in colloidal crystals. The result showed that this method needs a large amount of crystal sample and is prone to the structural defects inherent in the body of the crystals originated from the evaporation stage. Therefore, an approach for the drying of the samples that avoids these defects is also recommended.

2. Sample preparation has proved to be a critical stage in the characterization procedure. PDMS removal in achieving the structure for the characterization is the first stage that might disturb the delicate nanostructure underneath. Therefore use of a thin layer of Au sputtered on the surface of PDMS before the crystal assembly is recommended. Furthermore, non-destructive characterization methods that rely on probing the structural features without any further preparation would be preferred.

3. The sizes of SDS-protein complexes are subject to large uncertainties and is still an open research field. Therefore a reliable and accurate method for the measurement of their sizes and also probing their structural shapes is necessary. Dynamic light scattering can be a reliable method in achieving this goal. With the accurate values of the protein sizes and shapes, separation mechanism can indeed be reliably studied at a molecular scale.

4. Results of protein separation achieved in chapter 3, indicated peak broadening at small pore sizes that is undesirable for an efficient separation. According to these results, optimization of the conditions of electrophoretic separation is necessary. This includes buffer pH, ionic strength and the geometry of the microfluidic chip at the injector part and also the initial protein denaturing step.

5. Based on our separation experiments, the colloidal crystals of particles smaller than 100 nm showed structural instabilities at high field strengths that are necessary for a faster and efficient protein separation. An approach for the fabrication of more robust crystals is therefore recommended.

APPENDIX A Theoretical pore size in an LS_2 structure

The pore size of an LS_2 structure was calculated based on a geometrical model shown in Figure A-1. Here the objective is to calculate the value of r', the radius of the largest circle, the target circle, that can be embodied within the interstices of the larger (shown in gray) and smaller particle (shown in dark gray).

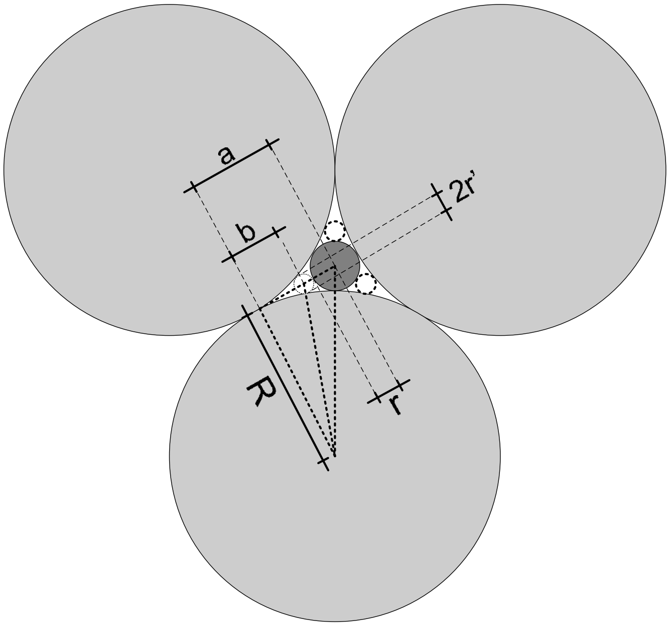

Figure A-1 Schematic of the geometrical model for the calculation of the theoretical pore size in a LS2 structure

The distance of the centroid of the small particle to the point where two larger particles touch each other can be calculated via the Pythagorean theorem

$$a=\sqrt{(R+r)^2-R^2}=\sqrt{r^2+2Rr} \tag{A-1}$$

where R and r are the radiuses of larger and smaller particles, respectively. Following the same theory for distance of the centeroid of the target circle to the touch point of the larger particles yields

$$b=\sqrt{(R+r')^2-R^2}=\sqrt{r'^2+2Rr'} \tag{A-2}$$

Now the radius of the target circle can be calculated by subtracting the a and b lengths

$$r'=a-b-r \tag{A-3}$$

Replacing equations (A-1) and (A-2) into (A-3) and squaring terms at both sides of the equal sign yields

$$\left(\surd(r{}^\wedge 2+2Rr)-\surd(r{}^\wedge 2+2Rr')\right)^2=(r'+r)^2 \tag{A-4}$$

Further algebric manipulation gives the following quadratic equation

$$(R-4r)r'^2-(4r^2+2Rr)r'+Rr^2=0 \tag{A- 5}$$

that has the following two roots

$$r'=\frac{(4r^2+2Rr)\pm\sqrt{(4r^2+2Rr)^2-4(R-4r)(Rr^2)}}{2(R-4r)} \tag{A- 6}$$

which can be further simplified as

$$r'=\frac{(4r^2+2Rr)\pm\sqrt{16r^4+32Rr^3}}{2(R-4r)} \tag{A- 7}$$

where the smallest root was acceptable, geometrically, as the pore size.